Spring 1-1-2017

The Nano Dust Analyzer for the Detection and Analysis of Nanometer-Sized Particles from the Inner Heliosphere

Leela Elise O'Brien
University of Colorado at Boulder, leelaobrien@gmail.com

The Nano Dust Analyzer for the Detection and Analysis of Nanometer-Sized Particles from the Inner Heliosphere

by

Leela Elise O'Brien

B.S. University of Nevada, 2011

A thesis submitted to the

Faculty of the Graduate School of the

University of Colorado in partial fulfillment

of the requirement for the degree of

Doctor of Philosophy

Department of Aerospace Engineering Sciences

2017

This Thesis entitled:
The Nano Dust Analyzer for Detection and Analysis of Nanometer-Sized Particles from the Inner Heliosphere
written by Leela O'Brien
has been approved for the department of Aerospace Engineering Sciences

_____
Prof. Zoltan Sternovsky

_____
Prof. Mihaly Horanyi

Date: _____

The final copy of this proposal has been examined by the signatories, and we find that both the content and the form meet acceptable presentation standards of scholarly work in the above mentioned discipline.

O'Brien, Leela E. (Ph.D., Aerospace Engineering Sciences)

The Nano Dust Analyzer for the Detection and Analysis of Nanometer-Sized Particles from the Inner Heliosphere

Thesis directed by Professor Zoltan Sternovsky

The Nano-Dust Analyzer (NDA) instrument is developed for the detection and compositional analysis of nanometer-sized dust particles originating near the Sun, and delivered near Earth's orbit by radiation pressure and electromagnetic forces. These particles report on processes occurring close to the Sun. This thesis investigates the basic dynamical processes and the results of the numerical calculations are then used to design and optimize the NDA, a linear time-of-flight mass analyzer. The challenge of needing high sensitivity of detection while pointed close to Sun's direction is solved by optimizing the instrument's field-of-view, pointing requirements, and designing an internal baffle system to suppress the effects of solar-ultraviolet radiation.

Little is known about the origin, distribution and fate of dust particles in the inner Solar System. The interplanetary dust complex is fed mostly by comets and asteroids. The interplanetary dust particles are transported towards the Sun (on timescales of ~ thousands of years) where they undergo multiple processes: most are destroyed by the heat of the Sun or sputtering by solar wind particles, while a small fraction is expelled out of the Solar System. Grinding from mutual collisions alters their size distribution, which intensifies closer to the Sun, where their density increases. These particles influence the solar wind plasma, being one of the sources of inner source pickup ions, or mass loading the expanding solar wind. The importance of these effects is yet to be fully understood.

The population of particles expelled from the Solar System include submicron-sized dust particles known as β-meteoroids, which are accelerated by solar radiation pressure. Nanometer-sized particles also belong to this population and are picked up and accelerated to high velocities by the solar wind. There is likely a wealth of information in their mass distribution, composition and dynamical properties, including their temporal and spatial flux variations, which is influenced by their interaction with the solar wind. Past missions have identified and partially-characterized particles originating from the inner Solar System. This thesis lays the foundations for providing measurements to resolve outstanding science questions by presenting a concept for their detection and a basic design for a capable instrument.

DEDICATION

I would like to dedicate this dissertation to my entire family, who are all amazing humans who I have the utmost love and respect for. Their unwavering love, support, and encouragement has made it possible for me to chase my dreams and not give up when times were tough.

ACKNOWLEDGMENTS

I would like to express my gratitude toward my advisor Zoltan Sternovsky, who has tirelessly guided and supported me throughout my Ph.D. study and research. I have learned a great deal while working with him and have developed a valuable skillset under his guidance. He provided me with the opportunity to discover my passion for space instrumentation and I've been inspired by his innovation in the field.

I would also like to express gratitude toward Dr. Antal Juhasz, who provided me with the dust dynamics numerical model and guided me through the modeling portion of my thesis project. I would not have been able to explore this type of research and develop a well-rounded thesis without the great amount of help and knowledge he provided me.

I would also like to thank Eberhard Grün, Mihaly Horanyi, and Sascha Kempf for sharing their wisdom and giving me the opportunity to work on very exciting projects as a graduate student. Similar thanks goes to David Malaspina for taking the vision for the Nano Dust Analyzer to a new and exciting level and allowing me to be a part of it. Special thanks also goes to Eberhard Mobius and David James for being wonderful people to work with, as well as inspiring me and believing in me.

Lastly, I would like to acknowledge the support for my dissertation research project from NASA's Solar and Heliospheric Physics program under Grant No. NNX11AB53G, as well as the NASA Earth and Space Sciences Graduate Fellowship (NESSF) program, grant number: NNX14AO15H.

TABLE OF CONTENTS

LIST OF TABLES

LIST OF FIGURES

Chapter 1: Introduction

The origin, distribution, interactions, and fate of dust in the inner Solar System have not been explored in great depth. Observations of zodiacal light scattered from interplanetary dust particles show that the dust density increases with distance toward the Sun and is eventually cleared out due to the intense heat from the Sun. The inner Solar System dust complex is primarily fed by mutual collisions of cometary and asteroid material. Cometary material contributes to the dust cloud at a range of heliospheric distances, but its production of dust is expected to be greatest at distances close to the Sun, whereas asteroid contributions originate mostly within the main asteroid belt at ~ 2-4 AU. The interplanetary dust particles (IDPs) generated are transported to the Sun on very long timescales (~ thousands of years) by an effect known as the Poynting-Robertson drag [*Russell,* 1929]. With increasing density, the frequency of mutual collisions increases toward the Sun and a fraction of the generated IDPs will be transported out of the Solar System. Submicron-sized particles (referred to as β-meteoroids) can be expelled by radiation pressure and have been detected at Earth's orbit as particles arriving approximately from the solar direction. Nanometer-sized dust particles are also generated in the inner Solar System. While there has been no direct detection of this particle population by dedicated dust instruments, numerical simulations show that they are quickly picked up by the solar wind, and become entrained in its flow out from the Sun [*Mann et al.,* 2012].

Nature is thus delivering samples of interplanetary dust in the form of nano-dust and β-meteoroids processed near the Sun to 1 AU, where they can be detected and analyzed. These

particles transported outward from the Sun present a chance to explore the origin, distribution, and variability of dust near the Sun from Earth's orbit, which presents a mission opportunity that is more likely than journeying to the inner Solar System. Nano-dust particles are expected to couple strongly to the solar wind through the Lorentz force, and the temporal and spatial variability of their fluxes at 1 AU is a function of this complex interaction. Measurement of their composition and variable fluxes provides information about dust-solar wind plasma interactions, in which nano-dust contributes to the mass, momentum, and energy balance of the solar wind through mass loading and pickup ion generation. The potentially important role of dust in solar wind processes thus deserves more attention.

This thesis presents the development of the Nano Dust Analyzer (NDA): a linear time-of-flight mass spectrometer to detect nano-dust particles that reach Earth's orbit and measure their elemental composition. NDA is the first dust instrument designed to specifically measure nanometer-sized particles originating near the Sun and confirm their existence and interaction with the solar wind. The instrument development effort is motivated by signals serendipitously recorded by the antennas of the STEREO radio instrument, which have been interpreted as nano-dust impacts on the spacecraft [*Meyer-Vernet et al.,* 2009].

NDA is designed to measure nano-dust over the entire expected range of velocities and masses and is required to operate while pointed close to the Sun's direction, from where the dust populations are expected to arrive. Thus NDA must be able to make sensitive measurements while exposed to solar ultraviolet (UV) radiation and solar wind particles that can scatter into the detector and interfere with the instrument's performance. This is achieved through an optimization of the instrument pointing and field-of-view, as well as the inclusion of an optical baffle system to reduce the effect from solar UV radiation. A solar wind suppression grid system

reduces the effect of solar wind particles.

Numerical modeling of nano-dust trajectories provides insight into the nature of their interaction with the solar wind. The numerical modeling shows that nano-dust are picked up and accelerated by the solar wind convection electric field and begin gyrating along the interplanetary magnetic field lines and are transported outward of the Sun, where the smallest nano-dust particles can arrive at 1 AU with speeds close to that of the solar wind [*Mann et al.,* 2012]. The nano-dust speed distribution and arrival directions at 1 AU are calculated using the numerical model to constrain the instrument design and operation requirements. Furthermore, recent modeling of nano-dust trajectories have shown that the interaction of nano-dust with the complex structure of the interplanetary magnetic field can result in a highly variable temporal and spatial distribution of nano-dust fluxes at 1 AU [*Juhasz and Horanyi*, 2013]. Thus, characteristics of the nano-dust-solar wind interaction could be linked to flux measurements. Furthermore, flux variability could also be described by nano-dust interaction with interplanetary coronal mass ejections (ICMEs). Preliminary analysis described in this work shows that ICMEs can potentially deliver nano-dust to near Earth's orbit in high concentrations.

The NDA is developed to address a number of outstanding science questions regarding the interplanetary dust complex including: what are the sources and sinks of IDPs existing in the inner Solar System? How do they evolve in size distribution/dynamics and what fraction is lost to the Sun through sublimation or sputtering vs. the fraction that is driven out of the Solar System through solar radiation pressure and solar wind pickup? Furthermore, if nano-dust couples to the solar wind, what is the nature of this interaction? NDA can address such questions by (1) measuring nano-dust fluxes and mass distribution to confirm the existence of nano-dust and report on the size distribution and collisional processes near the Sun. (2) Measuring

elemental composition to reveal information about their sources, and (3) the spatial and temporal variability of measured fluxes can reveal the nature of their interaction with the solar wind.

This thesis is structured as follows: Chapter 2 provides a background of the current understanding of the dust complex in the inner Solar System, which is maintained through various production and loss processes driven by the competing forces in the inner Solar System. This chapter also introduces the concept of nanometer-sized dust particles, their detection, and how they differ from the rest of the dust population. Chapter 3 describes the numerical modeling of dust dynamics in the inner Solar System and the influence of the solar wind on nano-dust trajectories and their distribution near Earth's orbit and how these results drive the instrument design and operation requirements. The dynamics model is extended to explore the delivery of nano-dust to near Earth's orbit by ICMEs where their fluxes could potentially be detected by NDA.

Chapter 4 provides a detailed description of the concept and design of NDA and its capability of addressing the science questions. As a proof of concept, a laboratory prototype version of NDA has been built and tested for performance verification. Details of its development and testing are discussed in this chapter. Chapter 5 describes the optical analysis used in the characterization and optimization of NDA's performance under solar UV exposure while pointed close to the Sun and reports the results of the analysis.

Chapter 2: Dust in the Inner Solar System

2.1 Flow of Meteoritic Matter in the Solar System

The current understanding of the dust complex in the inner Solar System and its evolution is based mostly on zodiacal light observations and in situ measurements at 1 AU, mainly covering the portion of the dust cloud concentrated near the ecliptic plane. Zodiacal light measurements by the Helios spacecraft have provided information about the dust density between 0.3 and 1 AU. However, information reporting on the dust complex within 1 AU is still very limited. This chapter describes the inner Solar System dust complex and its evolution as it is currently understood, including dust sources, size-dependent fluxes at and within 1 AU that are driven by collisional fragmentation and transport processes, and the orbital evolution and transport of interplanetary dust particles (IDPs) and the forces that dominate their motion.

2.1.1 Interplanetary Dust Sources and Composition

The inner Solar System dust complex is formed through the evolution of small bodies and is fed mostly by asteroid and cometary material. Other less contributing, albeit more exotic sources include dust from the collisions and fragmentation of Kuiper Belt objects [*Liou, Zook, and Dermott,* 1996; *Poppe,* 2016] and interstellar dust particles passing through the Solar System [*Grün,* 1994; *Sterken et al.,* 2012].

Asteroid material continually feeds the cloud of IDPs. Mutual collisions of asteroid material occur primarily in the main asteroid belt (2–4 AU) and generate fragments over a wide distribution in size. Collision models of asteroid material predict the mass distribution, which

agrees well with that determined by observations [*Dohnanyi*, 1969]. The estimated dust production rate from asteroids is 10^{9}-10^{11} kg year^{-1} [*Mann*, 1996].

Comets act as sources of dust particles over a wide range of heliospheric distances. However, the rate of cometary dust production increases greatly with decreasing distance towards the Sun. A fraction of the dust particles released by comets are in bound heliocentric orbits similar to their parent bodies, and a fraction of the submicron-sized particles are released into hyperbolic orbits as an effect of solar radiation pressure [*Sekanina et al.*, 2001]. Due to the much-increased activity close to the Sun, Sun-grazing comets act as transient sources, increasing the dust density locally and temporally. Recent modeling constrained by infrared astronomical satellite observations indicates that the dominant sources of IDPs within 5 AU are Jupiter-family comets, which contribute to a population with a broad range of inclinations [*Nesvorny et al.,* 2010]. The variability in cometary activity and uncertainty in the size distribution of released dust makes it difficult to predict the dust production rate from comets, but the estimated maximum mass losses from a single short and long-period comet are 1.44×10^{5} kg s^{-1} (Comet Halley) and 1.8×10^{6} kg s^{-1} (Comet Hale-Bopp), respectively [*Mann et al.,* 2006].

Micrometeorite samples collected at Earth in the stratosphere and in the ices of Antarctica and Greenland reveal compositional information about both asteroid and cometary IDPs [*Leinert and Grün*, 1990; *Jessberger et al.,* 2001]. The collected samples bear similarities to carbonaceous chondrites, which are a class of meteorites that have not undergone significant melting or differentiation since their formation. Lab measurements of collected micrometeorite samples reveal mineral composition of olivine, pyroxene, magnetite, and Mg-Fe silicates. IDPs collected in the stratosphere bear elemental composition: Mg, Al, Si, S, Ca, Cr, Mn, Fe, and Ni [*Jessberger et al.*, 2001]. These particles may be representative of dust originating from

asteroids. Atmospheric sampling of such particles is biased toward IDPs that survive Earth's atmosphere and have likely lost volatiles prior to collection, however. Analyses of samples returned from the Itokawa asteroid visited by the Hayabusa spacecraft confirmed that Itokawa, an S-type asteroid (the most common asteroid type in the inner belt), bears composition of ordinary chondrites, which are the most abundant class of meteorites found at Earth. The measurements reveal that many of the samples were mono-mineralic, including a large number of olivine and low-Ca pyroxene [*Nakamura et al.,* 2011].

In situ measurements of cometary dust (e.g. from Halley, Shoemaker-Levy, and Hale-Bopp) have shown a "CHON" component, rich in elements C, H, O, and N as well as a "rock" component, rich in Si, Fe, and Mg [*Sekanina et al.,* 2001]. Cometary dust returned by the Stardust mission showed a large range of minerals consistent with the CI class of carbonaceous chondrites, including an abundance of silicates, such as olivine [*Brownlee et al.,* 2006]. Recent compositional measurements by the COSIMA dust analyzer on the Rosetta cometary mission have shown the elemental composition to be heterogeneous. The particles could be composed of silicate minerals such as olivine and pyroxene and iron sulfides. The compositional analysis also shows that the Na to Fe ratio found in particles is larger than the abundance found in CI carbonaceous chondrites. Additionally, no organic material has been found in their compositional analyses [*Hilchenbach et al.,* 2016].

2.1.2 Dust Production, Transport, and Destruction

The mass and spatial distribution of dust in the inner Solar System is a result of continuous and transient sources feeding the dust complex, the dynamical and transport processes, and the eventual loss and destruction of the IDPs. This section provides a description

of the evolution and balance of the dust complex in the inner Solar System as it is currently understood.

Collisional fragmentation of mostly asteroid and cometary material forms the IDP population in the inner Solar System. The dust complex is maintained through multiple dust production and loss processes. Collisional breakup contributes to both production and loss of IDPs and will alter the dust size distribution, if not replenished. Collisions are the greatest loss process for the largest IDPs (> 10^{-6} g), which must then be replenished by influx of more material. Collisional fragmentation continuously produces smaller dust particles such as those in the 10^{-5}–10^{-10} g range, and a steady distribution in this mass range is maintained through a collective motion toward the Sun via the Poynting-Robertson (PR) drag [*Russell,* 1929; *Grün et al.,* 1985; *Leinert and Grün*, 1990], where the effect of solar radiation on the dust particle causes dust particles to spiral in toward the Sun (the PR effect is described in more detail in Sec. 2.2). Thus, the particles move closer to the Sun, where they occupy a smaller volume, which leads to an increase in the spatial density that scales roughly as $n \sim r^{-1.3}$, as determine by the Helios spacecraft zodiacal light measurements performed between 0.3 and 1 AU where r is the distance from the Sun [*Leinert,* 1981; *Grün et al.*, 1985]. Thus, the collision rate also increases with r and the smallest dust particles are expected to be generated with greater efficiency and in larger quantities at distances close to the Sun.

A specific class of dust particles belonging to the mass range ~10^{-12}–10^{-15} g are formed mostly through collisional fragmentation of meteoroids and direct release from comets [*Zook and Berg*, 1975]. These particles, known as β-meteoroids, are submicron in size (~0.1–1 μm radius) and their dynamics are strongly affected by solar radiation pressure. As a result, they can be blown out of the Solar System on hyperbolic orbits, contributing to another loss process of the

inner Solar System dust complex. IDPs smaller than β-meteoroids are also generated in the inner Solar System, primarily at distances close to the Sun where the dust density and collision rate is the highest. These nanometer-sized particles, known as nano-dust, belong to the mass range ~10^{-15}–10^{-20} g and approximate size range of 1–100 nm. All dust particles attain a surface charge in the space environment (see Sec. 2.5) and the nano-dust particles have high charge-to-mass ratios Q/m. As a result, their motion is most strongly influenced by the solar wind Lorentz force. The particles get picked up and accelerated by the solar wind and approximately follow the interplanetary magnetic field (IMF) lines as they spiral outward from the Sun. Figure 2.1 illustrates the flow of matter in and out of the inner Solar System, highlighting collisional fragmentation, the PR effect, and the ejection of submicron and nanometer-sized particles through radiation pressure and solar wind effects.

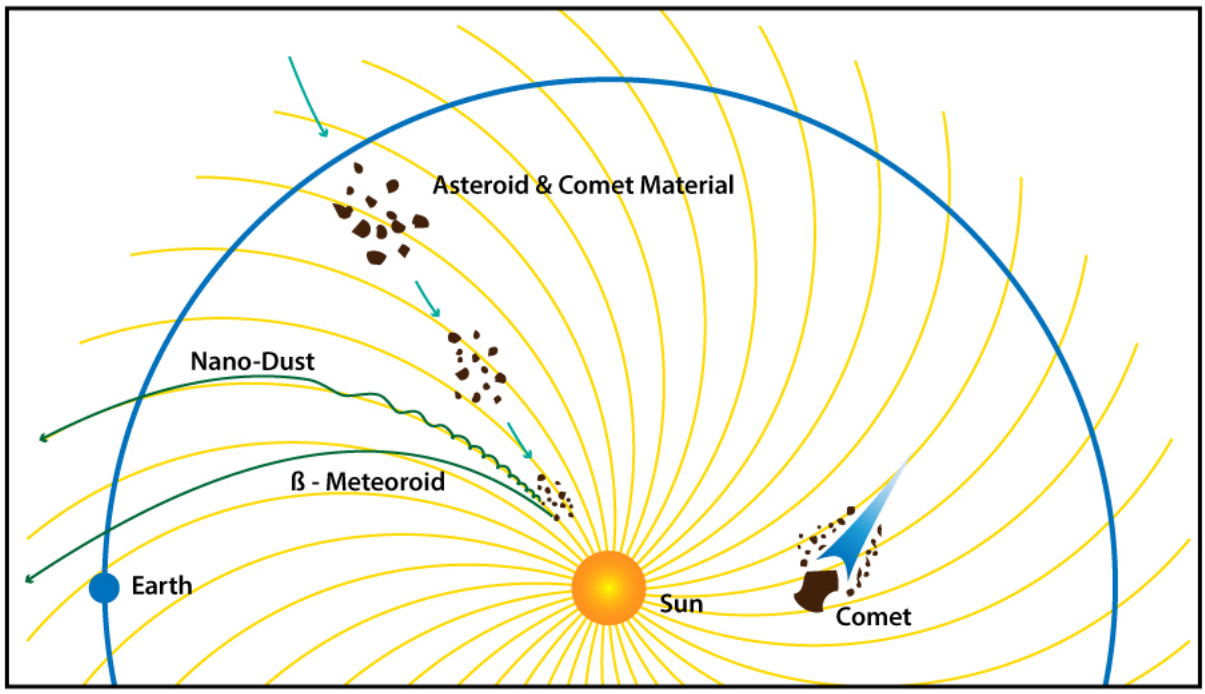

Figure 2.1 Illustration of dust production due to asteroids and comets and the inward transport of dust in the inner Solar System through collisional fragmentation and the Poynting-Roberston effect. In contrast, small dust particles in the form of *β*-meteoroids and nano-dust travel outward due to solar radiation and solar wind effects from the place of their generation.

Other mechanisms of dust loss from the inner Solar System complex include sputtering, sublimation, and rotational bursting of dust particles. Energetic solar wind particles impacting dust grains can sputter atoms and molecules from the surface, slowly eroding the dust particles, especially at distances near the Sun (< 0.1 AU) [*Mukai and Schwehm*, 1981]. Irregular transfer of solar wind particle or photon momentum due to dust surface irregularities can also lead to destruction of IDPs through rotational bursting, which occurs well-within 0.1 AU [*Misconi*, 1993]. The dust population near the Sun is also cleared out due to sublimation. The distance from the Sun at which a dust particle sublimates depends on the particle's temperature and chemical composition. Dust particles composed of pure water ice sublimate at a few AU [*Mukai and*

Mukai, 1973], whereas refractory dust composed of silicates, carbonaceous grains and metals sublimate closer to the Sun ~2–10 R_{Sun} where R_{Sun} is the solar radius (1 AU = ~215 R_{Sun}) [*Lamy,* 1974; *Mukai et al.,* 1974; *Kimura et al.,* 2002]. Thus, inward of ~10 R_{Sun}, dust destruction is dominated by sublimation and varies with dust size and composition, eventually leading to a 'dust-free zone' which could extend as far from the Sun as ~2–3 R_{Sun}. Figure 2.2 shows the evolving distribution of the dust in the inner Solar System (including all sources) through the production, transport, and loss processes discussed in this section.

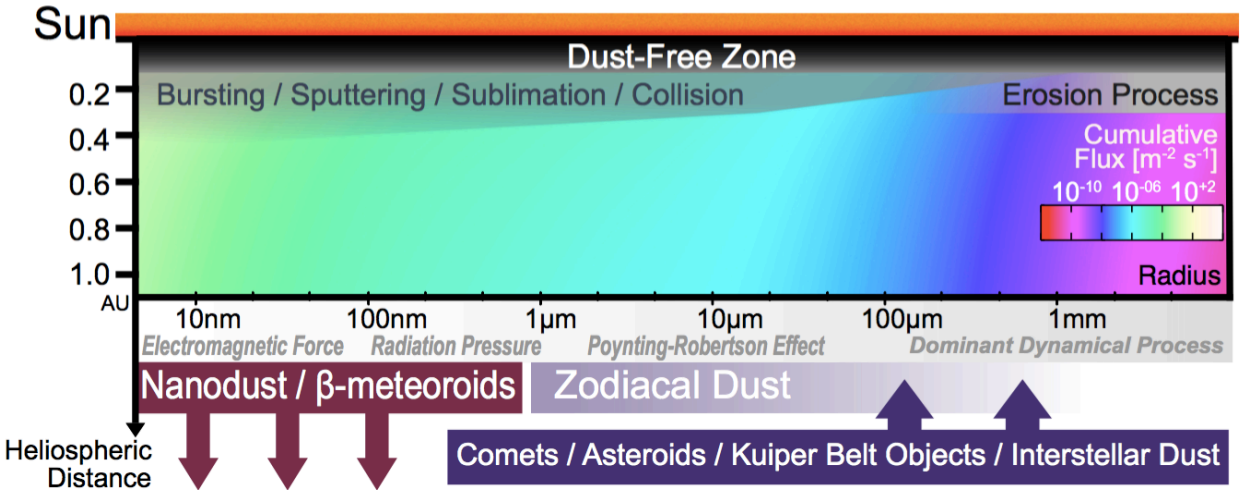

Figure 2.2 Depiction of the production and processing/evolution of dust in the inner Solar System discussed in this section (figure courtesy of Sean Hsu).

2.1.3. Estimates of Dust Flux, Density, and Size Distribution

The previous section paints a picture of the evolving dust complex of the inner Solar System through the various production and loss mechanisms. This section more specifically discusses the current understanding of the dust environment near the Sun. Observation-based

dust flux models are paired with dust production/loss models derived from collisional fragmentation laws, PR transport estimates, and dust loss rates through solar radiation pressure effects to describe a dust complex maintained by incoming and outgoing fluxes.

Dust fluxes at 1 AU have been measured/estimated by meteor observations, lunar crater samples, and satellite measurements. Models have been developed to provide context for the measured fluxes at 1 AU as a function of dust mass. Two notable models include the Lunar Dust Flux Model (LFM) and the Interplanetary Dust Flux Model (IFM). It is outside the scope of this thesis to discuss the details of the models and their construction, but a brief discussion is provided to describe how the IDP fluxes and distribution in the inner Solar System have been estimated. Both LFM and IFM models describe the particle fluxes as a function of mass (Fig. 2.3). The fluxes are derived for a spinning flat sensor at 1 AU, which has a π steradian effective solid angle and assumes an isotropic flux of dust. The LFM model is built from the size distribution of craters found on lunar rocks combined with the Pegasus spacecraft flux measurements [*Grün et al.*, 1985]. The IFM is derived from flux measurements performed by Pegasus, HEOS-2, and Pioneer 8 and 9 spacecraft. Figure 2.3 shows the LFM and IFM flux curves and includes the satellite-based flux measurements and the mass range they cover. The figure also includes the flux curve of β-meteoroids and their fluxes directly measured by Pioneer, which are generated within 1 AU and ejected across Earth's orbit through radiation pressure effects [*Grün et al.*, 1985]. The nano-dust population produced near the Sun and ejected outward to 1 AU is not represented in the dust flux models reported here.

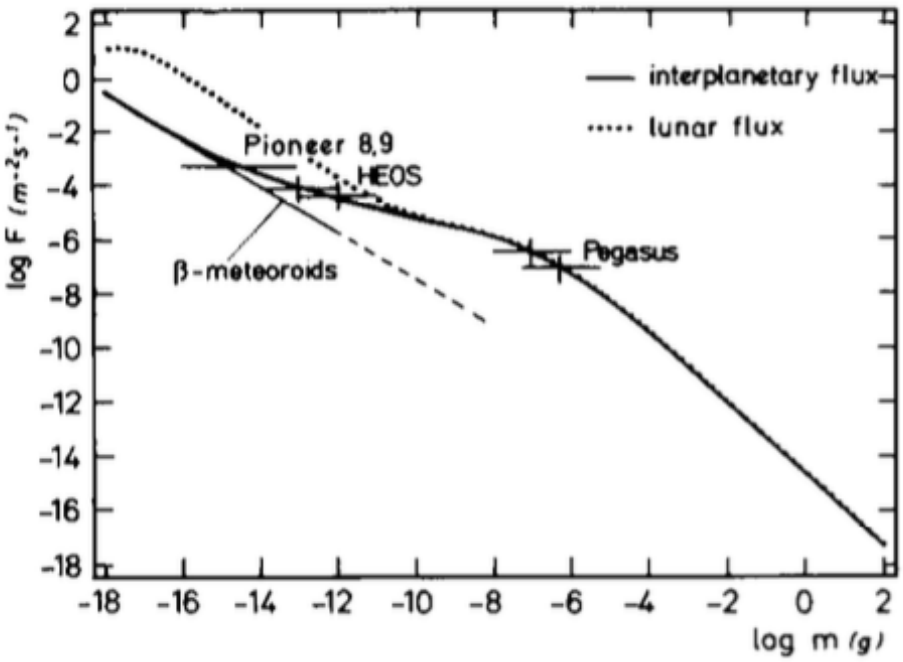

Figure 2.3 Observation-based Interplanetary Flux Model (IFM) and Lunar Flux Model (LFM) curves describing particle fluxes at 1 AU as a function of particle mass. The LFM deviates from the IFM at smaller masses due to the overabundance of micro-craters found on lunar rocks (from *Grün et al.*, 1985).

The flux information at and within 1 AU can be used to describe the flux curve as a function of radial distance from the Sun *r*. The spatial density of interplanetary dust as a function of *r* was determined by the Helios spacecraft zodiacal light measurements between 1 and 0.3 AU to be $n(r) \sim r^{-1.3}$. The flux-density relationship at 1 AU (Eq. 2.1) can then be used to estimate the dust flux at distances inside of 1 AU (Eq. 2.2).

$$F(m, r_0) = \frac{v_0}{k} n(m, r_0) \tag{2.1}$$

$$F(m,r) = \frac{v_0}{k}\left(\frac{r}{r_0}\right)^{-0.5} n(m,r_0)\left(\frac{r}{r_0}\right)^{-1.3} = F(m,r_0)\left(\frac{r}{r_0}\right)^{-1.8} \quad (2.2)$$

In these equations, r_0 = 1 AU and v_0 is the average impact speed at 1 AU, which scales with distance toward the Sun as $(r/r_0)^{-0.5}$. v_0 = 20 km s^{-1} is an assumption of the average impact speed at 1 AU that is applied in the flux curve models: i.e., the impact speed of a dust particle on the Moon, at a sensor at 1 AU, and the relative impact speed between two colliding particles and is based on meteor observations [*Zook,* 1975]. The parameter k is a function of the detector solid angle and flux directionality and is used to relate the measured fluxes to the IFM and LFM curves $F(m,r_0)$ [*Grün et al.*, 1985].

The distribution and stability of the dust complex inside of 1 AU has not been explored in great depth and the 1 AU-based flux models extrapolated to distances closer to the Sun are not fully representative of the dust environment. The spatial dust density as a function of distance from the Sun is assumed to be independent of mass/size. Thus, the flux curves are assumed to have the same shape at distances close to the Sun as they do at 1 AU. The Helios zodiacal light observations do not indicate much of a change in the size distribution of dust particles within 1 AU [*Leinert et al.,* 1981], but the observations are dominated by the ~10–100 μm (~10^{-10}–10^{-5} g) size range and might not be representative of the distribution of particles outside of this range. For example, the collision rate increases with distance toward the Sun (as $C \sim r^{-3.1}$), the large dust particle population ($m > 10^{-5}$ g) is expected to be reduced and could result in a temporary depletion without a replenishing source within 1 AU.

Studies applying the dust flux estimates and collision and fragmentation models reveal the uncertainty in the evolving dust complex in the inner Solar System, especially at distances

within 1 AU where observations are lacking. Dust production and loss rates determined from the dust flux estimates at 1 AU, collisional fragmentation models, as well as PR drag and β-meteoroid loss rates do not fully support that a steady state dust complex is maintained, suggesting potential flaws in the dust flux model and/or fragmentation laws [*Grün et al.,* 1985]. The fragmentation laws are based on laboratory measurements using large dust particles with low collision speeds (1 mm grains at 3 km s^{-1}) [*Fujiwara,* 1977], which might not accurately represent the small high-speed dust particles in the inner Solar System. Further observations of the dust distribution within 1 AU can shed light on these uncertainties of the near-Sun dust complex.

2.1.4. Orbital Evolution and Distribution Near the Sun

The spatial and orbital distribution of the dust population near the Sun is a function of the parent body orbits and the IDPs subsequent orbital evolution. IDPs generated by mutual collisions of asteroid and comet material will initially be in orbits close to that of their parent bodies. Parent body asteroids are distributed in low-inclination ($i < 30°$), low eccentricity ($e < 0.1$) orbits. Short period comets have $i < 40°$, $e < 0.4$, whereas long period comets can exist in highly inclined orbits with $0° < i < 180°$ [*Mann et al.*, 2004]. As a function of dust size and distance from the Sun, the PR drag will impose a drift toward the Sun, which causes a reduction in the semi-major axes and eccentricity of their orbits, but no change to their inclinations. Thus, the near-Sun dust cloud is expected to have a component concentrated near the ecliptic plane with eccentricities that depend on the source as well as the IDP's state of orbital evolution. For example, IDPs born from asteroids that are transported to 10 R_{Sun} under the PR effect will typically have reduced eccentricities with $e \approx 0.01$. IDPs born from short period comets can have higher initial eccentricities and will reach $e \approx 0.1$ at 10 R_{Sun} [*Mann et al.*, 2000].

A distribution of dust at higher latitudes is composed of IDPs supplied by long period/sun-grazing comets with large inclinations. Such IDPs are described by isotropically distributed orbital inclinations between 0° and 180° and orbits in both the prograde and retrograde direction [*Mann et al.,* 2000]. Figure 2.4 depicts the near-ecliptic plane distribution, referred to as the inner Solar System dust 'disk' as well as the high latitude component referred to as the 'halo' distribution. IDPs in the halo will have high velocities relative to the disk, influencing collision processes.

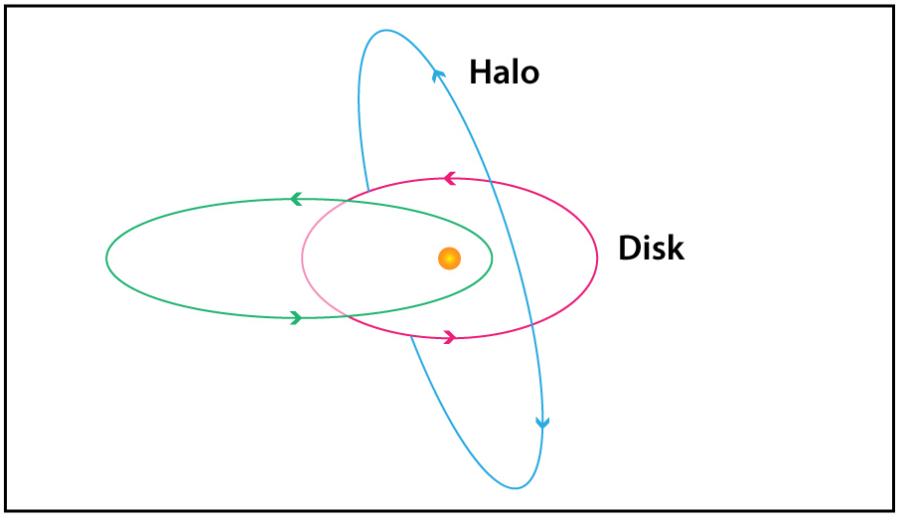

Figure 2.4 Schematic depicting IDP orbits in the dust complex of the inner Solar System. IDPs in the disk can have near-circular or eccentric prograde orbits, whereas halo dust have higher inclination orbits (prograde and retrograde). High collision rates/velocities can result between the two components.

Small-sized IDPs of asteroid and short-period comet origin can also be supplied to higher latitudes as a result of electromagnetic forces, which become stronger closer to the Sun [*Morfill*

and Grün, 1979; *Barge et al.,* 1982]. Depending on the IMF configuration, the solar wind Lorentz force will either accelerate IDPs above or below the ecliptic plane in latitude, resulting in a broadening of their inclinations. This effect is strongest for small dust particles that have a large Q/m but do not belong to the nano-dust or β-meteoroid populations. For example, model studies show that at 10 R_{Sun}, 2–5 μm particles initially with i = 30° can be deflected to inclinations ~ i = 50° and 0.5 to 2 μm can reach i = 70–90° depending on IMF strength [*Mann et al.*, 2000].

2.1.5. Summary of the Dust Evolution and Distribution

In summary, the current understanding of the mass/size, and spatial distribution of dust in the inner Solar System is described by production, loss, and transport processes of input asteroid and cometary material. The density and flux measurements at 1 AU have been used to construct dust flux curves, namely the IFM and LFM and β-meteoroid fluxes at 1 AU, that can also be extrapolated to describe the populations at < 1 AU using the dust density estimates (as a function of radial distance from the Sun) provided by the Helios measurements [*Grün et al.,* 1985]. Temporal and spatial variations in the flux/density, however, are likely introduced due to transient sources, such as Sun-grazing comets.

The spatial and size distributions of the dust population in the inner Solar System are a function of the parent body orbital elements and the orbital evolution of the IDPs. Collisional processes and the ultimate fate of the dust particles are influenced by their orbital evolution. Submicron and nanometer-sized particles are ejected from the Solar System and reach Earth's orbit weeks (β-meteoroids) and days (nano-dust) after they are generated by collisional fragmentation due to radiation pressure and solar wind effects, respectively. The dust particles

close to the Sun are eventually destroyed through sublimation, sputtering, and rotational bursting. Continual replenishment of IDPs maintains the complex.

2.2. Dust Dynamics in the Inner Solar System

The dust distribution in the inner Solar System and its evolution is characterized by competing dynamical processes. This section breaks down the discussion of dust transport and orbital characteristics mentioned in Sec. 2.1 into the fundamental forces that shape dust dynamics and evolution. The strongest forces affecting dust particle dynamics in interplanetary space are solar gravity, solar radiation, and the Lorentz force from the solar wind. The various dust populations are influenced by forces uniquely, depending on mass/size, orbital properties, and composition (e.g., light scattering properties). In particular, the populations of small (< ~1 μm) dust particles generated in the inner Solar System experience significant dynamical effects due to their strong influence by solar radiation pressure and the solar wind Lorentz force.

2.2.1. Gravitational Force

The force due to solar gravity dominates the motion of most dust particles in the Solar System, which can be approximately described by Kepler orbits around the Sun. The gravitational force is given by

$$\vec{F}_g = -\frac{GmM_{Sun}}{r^2}\hat{r}\,, \tag{2.3}$$

where G is the gravitational constant, m is the mass of the dust particle, M_{Sun} is the mass of the Sun, and r is the particle's radial distance from the Sun. As discussed in Sec. 2.1.4, IDPs

generated by collisional fragmentation or released from comets are expected to initially adopt similar orbits to the Kepler orbits of their parent bodies. This is especially true in the inner Solar System where Kepler velocities are large compared to the velocities the fresh fragments attain from the collision. Dust particles can also experience gravitational effects of planets, but these are excluded from this discussion because they are small and negligible for this inner Solar System dust complex.

2.2.2. Radiation Force

Solar radiation affects the dynamics of IDPs in three significant ways. One is radiation pressure, which is the outward radial force due to absorption/scattering of solar radiation. The second is the non-radial component of radiation pressure force that effectively 'slows down the particle' causing a drift toward the Sun. The third is the effect of dust charging due to photoelectron emission, which will be described in Sec. 2.5. Relative to solar gravity, the radiation pressure effect has the strongest influence on the dynamics of small dust particles that exist in a narrow size range (~0.1–1 μm). This is because the gravitational force is decreasing with dust size (grain radius) as r_g^{-3}, where the radiation pressure decreases as r_g^{-2}. Particles smaller than ~100 nm, however, stop scattering solar radiation efficiently and the radiation pressure effect diminishes. The momentum transferred by photons to the dust particle's surface is responsible for the radiation pressure, and the particle experiences a force directed radially outward from the Sun. The solar radiation pressure force experienced by a dust particle is described by the below equation.

$$\vec{F}_{RP} = \frac{L_{Sun} A \langle Q_{RP} \rangle}{4\pi r^2 c} \hat{r} \tag{2.4}$$

A is the cross sectional area of the dust particle, L_{Sun} is the solar luminosity, c is the speed of light, and $\langle Q_{RP} \rangle$ is the radiation pressure coefficient averaged over the solar spectrum. Q_{RP} varies as a function of dust size, radiation wavelength, and absorption/scattering properties of the dust particle, which are a function of dust composition and structure.

The radial acceleration, and overall effect the radiation pressure has on a dust particle's dynamics is evaluated in terms of the β parameter, which is the ratio of the forces of radiation pressure to solar gravity. Thus, the radial acceleration of a dust grain under the influence of both forces is

$$a_r = \frac{GM_{Sun}(\beta - 1)}{r^2} \tag{2.5}$$

For $\beta > 1$, the radiation pressure exceeds gravity and the particle is expelled outward from the Sun. Figure 2.5 shows β plotted against dust radius for a spherical silicate grain with density (2.5 g cm^{-3}) and light absorption properties expected for the IDP population [*Landgraf*, 1999]. Dust particles smaller than the characteristic wavelength of the radiation have a decreasing β with decreasing size, with a maximum at around 200 nm dust size.

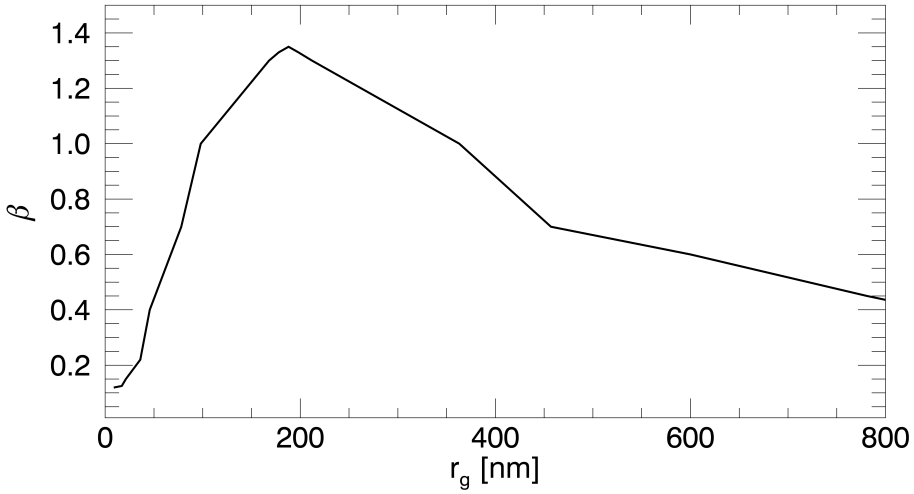

Figure 2.5 Example curve of β vs. dust size for a spherical silicate grain with an assumed density of 2.5 g cm^{-3} (data from *Landgraf,* 1999).

The radiation pressure force need not exceed the gravitational force for a particle to escape the Solar System. The particle will be ejected on a hyperbolic orbit if its specific kinetic energy is greater than the specific potential energy in the solar gravitational field, corrected for radiation pressure: $(1-\beta)U - 1/2(v^2) \geq 0$, where U is the specific potential energy. If the particle is generated at perihelion, the absolute minimum of β = 0.5 is required for the particle to be ejected on a hyperbolic orbit, and this corresponds to a particle in a circular orbit. The minimum β values can be even smaller for dust in eccentric orbits.

The second radiation effect presented is known as the Poynting Robertson (PR) drag, which influences dust transport on long timescales. In the reference frame of the Sun, the particle's absorption of solar radiation is isotropic. However, the re-emission is anisotropic due to the motion of the dust particle. Thus, the radiation carries away angular momentum from the dust particle, resulting in a small deceleration. The PR drag is most effective at perihelion, thus

the decelerating particle will experience a reduction in the semi-major axis, which means orbit circularization and slow transport toward the Sun. Without other mechanisms coming into play, the PR drag ultimately limits the lifetime of an IDP, which can equate to thousands of years, depending on the size of the particle. The equation for the PR drag and the PR lifetime of an IDP (T) are expressed below:

$$F_{PR} = \frac{r_g^2 L_{Sun}}{4c^2}\sqrt{\frac{GM_{Sun}}{r^5}} \tag{2.6}$$

$$T = \frac{r^2 c}{2GM_{Sun}\beta} \tag{2.7}$$

The small dust particles drift toward the Sun faster than the large ones. As an example of the time scale, a μm size particle will take a few thousand years to move into the Sun from 1 AU.

2.2.3. Electromagnetic (Lorentz) Force

Dust particles in the solar wind plasma are charged to a surface potential $\phi \sim +4$–5 V through photoelectron emission and collection of/secondary electron emission due to solar wind particles and will experience effects due to the solar wind Lorentz force expressed as:

$$\vec{F}_{EM} = Q(\vec{v} - \vec{w}) \times \vec{B}, \tag{2.8}$$

where Q is the net charge on the dust particle, calculated from the surface potential as $Q = 4\pi\varepsilon_0\phi r_g$ (where ε_0 is the permittivity of free space), v is the dust velocity, w is the solar wind plasma velocity, and $\vec{B}$ is the interplanetary magnetic field. Relative to solar gravity, which

increases as r_g^3, the Lorentz force increases as r_g. Thus the Lorentz force is more important for smaller sizes. Dust particles in the size range 0.5 μm < r_g < 10 μm experience orbital perturbations as a result of being deflected to higher latitudes by solar wind electromagnetic forces. The most affected are particles near the Sun, 20–60 R_{Sun} [*Barge*, 1982]. For particles farther from the Sun, the Lorentz force cancels out on average as they move across the different magnetic field sectors where field polarity reverses. The collective effect on the dust population is a broadening in latitudinal distribution (see Sec. 2.1.4), primarily near Lorentz resonances, where the orbital period of the grain matches up with the rotation periods of the magnetic field sectors.

Nanometer-sized (~1–100 nm) dust particles will experience dominant dynamical effects through interaction with the solar wind and will be picked up and accelerated by the solar wind convection electric field, $\vec{E} = -\vec{w} \times \vec{B}$. These particles gyrate along the magnetic field lines and upon being accelerated, can arrive at Earth's orbit with speeds near that of the solar wind. A more complete description of the nano-dust dynamics, understood through numerical modeling, is discussed in detail in Chapter 3.

2.3. Dust Measurements in the Inner Solar System

Information about the dust complex near the Sun can be obtained by a range of measurement methods with sensitivities over different size ranges. Figure 2.6 highlights various detection methods and the general size range they cover. Photographic and visual meteor observations, for example can detect larger dust particle sizes ~ down to 1 mm. Optical methods, such as thermal emission and scattered light (zodiacal) measurements, are dominated in the ~10–100 μm size range. Impact ionization-based measurements provide the most sensitivity and

can detect dust particles down to nanometer-sizes. This section will provide a brief description of some of the important dust measurement methods and the information they can or have revealed about the dust environment in the inner Solar System.

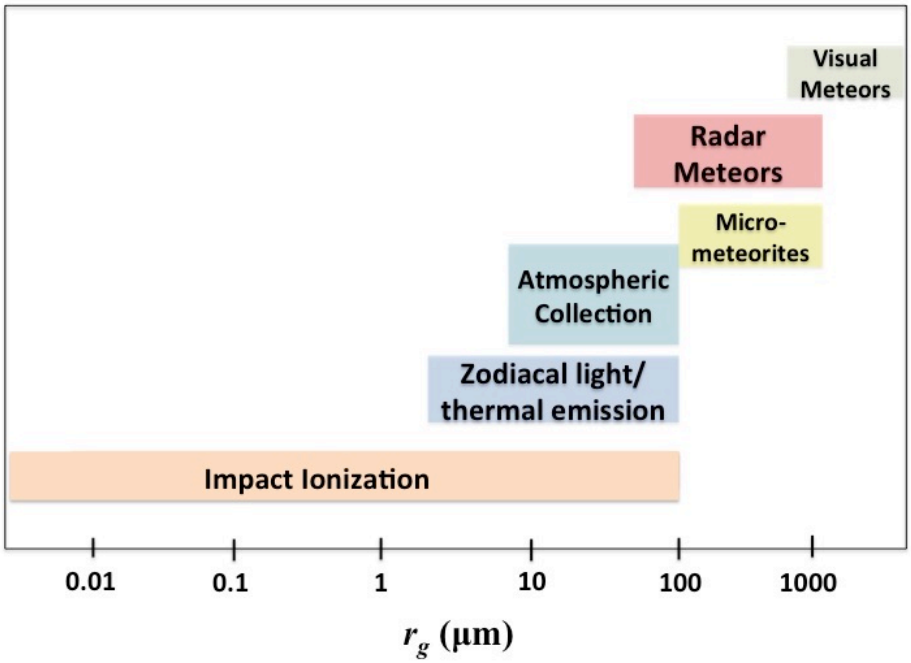

Figure 2.6 Various dust detection methods and the size ranges they typically cover. Meteor measurements cover the larger size distribution, while impact ionization covers a large range in dust sizes, extending to nanometer-sized particles. Note, impact ionization is sensitive to dust particles > 100 μm, but measurements are dominated by small particles, which have higher fluxes.

2.3.1. Zodiacal Light Observations

Zodiacal light is the solar radiation scattered and thermal radiation emitted by dust particles in the inner Solar System along the line-of-sight. Brightness, color, and polarization measurements of the scattered radiation reveals information about the dust spatial distribution,

number density, and size averaged over long distances in a size range dominated by 10–100 μm particles. Zodiacal light observations have shown that most of the dust outward from 0.3 AU is distributed in a rotationally symmetric cloud close to the ecliptic plane [*Mann et al.*, 2000]. The photometer on the Helios spacecraft revealed that the dust density (measured between 1 and 0.3 AU) increases with distance toward the Sun roughly as $n \sim r^{-1.3}$ [*Leinert et al.,* 1981].

2.3.2. Meteor Observations and Atmospheric Collection

Meteoroids entering Earth's atmosphere ablate and ionize forming a cloud of plasma, emitting radiation, known as meteors [*Ceplecha et al.,* 1998]. Photographic and radar measurements can provide information about the fluxes and velocities of the meteoroid population at 1 AU. Meteoroids surviving entrance into Earth's atmosphere have also been collected and analyzed to reveal particle density, morphology, and compositional information [e.g., *Brownlee*, 1996]. Dust particles have been collected in the stratosphere and on Earth's surface in Antarctic and Greenland ice samples, as well as samples from the ocean floor [*Maurette et al.,* 1991; *Kurat et al.,* 1994].

2.3.3 In-Situ Dust Measurements

In situ methods of dust detection have made it possible for the smaller-sized dust particles to be detected. Such methods include charge detection sensors that measure the charge induced on a conductor by a dust particle, which can reveal information about the velocity and trajectory of the dust particle [*Auer*, 2001]. Impact-related detection methods utilize the fast speed of dust particles and are biased toward measuring the smaller particles due to their higher flux. Such sensors include impact crater measurements, penetration detectors, as well as impact momentum transfer and impact ionization-based measurements. An example of one of the earliest impact sensors belonged to the Pegasus spacecraft, which used thin foil penetration detectors utilizing

dust impact-generated capacitor discharge to characterize the dust flux at 1 AU [*Naumann et al.,* 1969].

Impact ionization sensors are used because they can detect particle sizes that other methods cannot. Measurement of the ions and electrons generated in a high-speed dust impact ($> \sim 1$ km s^{-1}) can reveal information about the flux and speed of the impacting particles (will be discussed in more detail in Sec. 4.4). Pioneer 8 and 9 employed dust detection by multiple impact ionization sensors and provided reliable data of the dust flux at 1 AU using to the coincidence of multiple impact ionization signals [*Auer,* 2001]. The sensitivity of the detector enabled Pioneer to discover that most of the registered impacts were due to submicron-size particles arriving from the solar radial direction. These are the β-meteoroids expelled from the Solar System by solar radiation pressure (as discussed in Sec. 2.1 and 2.2) [*Berg and Grün,* 1973; *Zook and Berg,* 1975]. β-meteoroids were also detected by the Helios and Ulysses spacecraft [*Grün et al.,* 1980; *Hamilton et al.,* 1996]. Sensitive impact ionization detectors, including those on the Ulysses, Galileo, and Cassini spacecraft measured streams of nanometer-sized particles from the Jovian system [*Grün et al.,* 1993; *Baguhl et al.,* 1993; *Graps et al.,* 2000; *Kempf et al.,* 2005]. Impact ionization detectors, like the Helios and Cassini Cosmic Dust Analyzer (CDA) detectors, combine an impact ionization sensor with a time-of-flight mass spectrometer, which provides sensitive dust detection and compositional information about the impacting dust particle. More details of this dust detection method, which is used for the Nano Dust Analyzer, will be provided in Chapter 4.

2.4. Nano-Dust in the Inner Solar System

2.4.1 Overview

The micrometeoroid detectors on Pioneer, Helios, Ulysses, and Galileo have detected submicron-sized IDPs, known as β-meteoroids. However, nanometer-sized dust particles must also be generated in the inner Solar System, primarily close to the Sun where the dust density and collision rates are high. These particles can be influenced by the solar wind Lorentz force and are ejected from the inner Solar System with the solar wind. 'Nano-dust' is the term used to describe the nanometer-sized (~1–100 nm) dust particles that are generated near the Sun. As stated in the previous section, nanometer-sized dust particles originating from the Jovian and Saturnian systems have been measured by the dust impact detectors on the Ulysses and Galileo, and Cassini Cosmic Dust Analyzer, However, nano-dust particles, originating in the inner Solar System, have yet to be directly measured by a dedicated dust detector. This section provides a background on the current understanding of nano-dust in the inner Solar System, including their formation, basic properties, and interaction with the near-Sun environment.

2.4.2. Detection of Nano-Dust by STEREO/WAVES Antennas

While nano-dust have not yet been directly measured by a dedicated dust detector, they have possibly been detected serendipitously by the STEREO spacecraft orbiting the Sun at 1 AU. The WAVES electric field antennas on both STEREO A and B recorded large voltage pulses that are attributed to the impacts of high-speed nano-dust particles on the spacecraft or antenna [*Meyer-Vernet*, 2009]. A hypervelocity dust particle impacting a solid target will result in vaporization and partial ionization of both the dust and target material. The generated charge recollected by the spacecraft (or antenna) will result in a transient potential difference between the antenna and the spacecraft and thus a voltage pulse on the antenna signal. The amount of

charge generated by the impact is a function of both the dust mass *m* and velocity *v* as well as the target material. Through interaction with the solar wind, the smallest nano-dust particles are expected to arrive at 1 AU with $v \sim 300$ km s^{-1} (described in Ch. 3). Thus, a nano-sized dust particle moving at such a high speed could generate a measurable impact charge (see Sec. 4.4 for a description of the mass, velocity, and impact charge relationship).

One of the most interesting characteristics of the STEREO measurements is the intermittent nature of the nano-dust impact signals. Figure 2.7 shows the counts of voltage signals interpreted as nano-dust impact for the year 2007 on STEREO A and B, which are spatially separated in their orbits. This observed temporal and spatial variability could be an indication of the complex interaction of the nano-dust with the IMF [*Juhasz and Horanyi,* 2013] or could be a result of intermittent dust sources. Dedicated dust observations are needed to confirm the STEREO measurements and their interpretation.

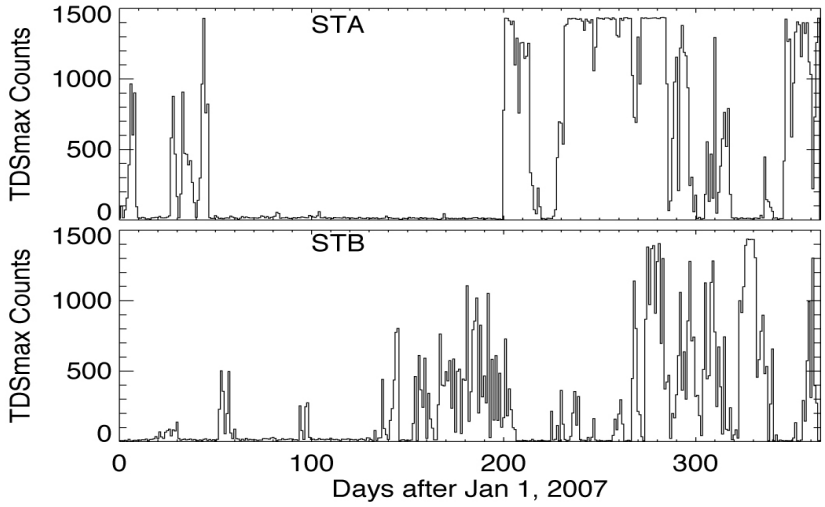

Figure 2.7 Counts of the voltage signals, interpreted as nano-dust impacts, measured on STEREO A and B (STA, STB) during 2007. Note the strong variability in time and between the spacecraft even for the early parts of the year, when the separation between the spacecraft is relatively small (from *Meyer-Vernet et al.*, 2009).

2.4.3. Formation and Existence of Nano-Dust

Nanometer-sized dust particles in the Solar System can be formed by release from comets, vapor-phase condensation, and collisional fragmentation of asteroid and cometary material. However, the process of formation of nanometer-sized dust particles in the inner Solar System is not understood well. Nano-dust can form in the inner Solar System through collisional fragmentation where the dust collision rate and relative velocities are high. Fragmentation laws are used to determine the mass distribution of impact-generated fragments and are, for example, based on empirical fragment size distribution determined by laboratory experiments with 1 mm, 3 km s^{-1} particles [*Fujiwara,* 1977]. Semi-empirical models [*Tielens et al.,* 1987, 1994; *Jones,* 1996] are also used to form the basis of knowledge of fragment sizes and distribution. Unfortunately, there have been no high-velocity experiments to show that nano-dust can be formed through dust collisions [*Mann et al.*, 2012] and the current understanding of the laws might not be valid in describing nano-dust formation. Nano-dust have a large surface-to-volume ratio where the surface atoms have more energy than the bulk atoms, thus higher energies are required to generate them, so the efficiency of nano-dust production may be lower than presumed.

Nano-dust could also be formed through condensation of gases released in an impact event. Condensation experiments of gases with meteoroid composition have shown formation of nanometer-sized refractory particles [*Reitmeijer*, 2000] and could potentially explain nano-dust formation near the Sun. Nano-dust formation this way, however, depends on the properties of the impact-generated vapor cloud and its expansion and due to the high temperatures in the solar corona and solar wind, formation through condensation may be a challenge [*Mann et al.,* 2012].

Mann and Murad [2005] discussed the possibility of silicon nano-dust particle formation and existence in the inner Solar System. While the thermo-chemical properties of nano-dust suggest that they can exist near the Sun, there is much uncertainty in how they form. Observations of nano-dust are needed to confirm their formation in the inner Solar System and investigate their abundance.

2.5. Charging of Nano-Dust

Dust particles in the Solar System are charged through a variety of mechanisms, including photoelectron emission, attachment and recombination of plasma particles, secondary electron emission, as well as thermionic and field emission. Charging through these mechanisms is a function of the particle's size, shape, structure, composition, and dust velocity relative to the plasma environment. The UV flux and plasma density/temperature corresponding to the dust particle's environment also determines the charging currents to the grain. As a dust particle becomes charged positively or negatively, it acquires an electrostatic potential that attracts particles of the opposite charge, thus, changing the fluxes of both incoming and outgoing particles until the incoming and outgoing currents balance. In the inner Solar System, where the UV flux is high, dust charging is dominated by photoelectron emission [*Mukai*, 1981]. For a dust particle in the solar wind plasma, the particle will reach a steady equilibrium potential once the flux of photoelectrons from the surface is reduced (due to the positive potential of the grain) and balances out the incoming flux of solar wind electrons. In order to do this, the dust particle's electric potential must exceed the typical kinetic energy of a photoelectron. If a Maxwellian distribution with temperature T_{pe} is assumed for a photoelectron, the dust potential must be $e\Phi = \eta k_B T_{pe}$ where η equals a few units, k_B is the Boltzmann constant, and e is the elementary

charge. The charge corresponding to the equilibrium potential is calculated as $Q = 4\pi\varepsilon_0\Phi r_g$ where ε_0 is the permittivity of free space and r_g is the dust grain radius. This charging process will be altered if the energy of incident electrons exceeds the atomic binding energy in the dust, then secondary electrons can be emitted by electron impact.

The charging of nano-dust is a bit more complicated, however. A nano-dust particle does not hold much charge (a few elementary charges for a 3 nm particle, for example) and the charging currents cannot be treated as continuous fluxes, but rather as discrete charging processes using Poisson statistics [*Hsu et al.,* 2011]. Solar wind particle impacts contribute to nano-dust charge fluctuations, which can alter the particle dynamics since the loss of a single charge can greatly change the charge-to-mass ratio. However, if the solar wind impact rate is larger than the Larmor frequency of the nano-dust particle, the impact charge fluctuations should average out [*Czechowski*, 2010]. For typical solar wind conditions, the impact rate is greater than the Larmor frequency at a range of distances from the Sun. For larger particles, the impact rate will increase and the Larmor frequency will decrease, so the estimation remains valid.

Nano-dust charging through photoelectron emission is further complicated as a result of their interaction with solar radiation. For most nano-dust, the wavelength of ionizing radiation, particularly Solar Lyman-α at 121.6 nm, is larger than the nano-dust size. For $\lambda >> r_g$, the photon absorption cross-section decreases with r_g^3, which is faster than the cross sectional area of the particle $\sim r_g^2$. Thus, the assumption that dust in the inner Solar System charge to ~ +4–5 V primarily through photoelectron emission might not be valid for the smallest nano-dust particles.

2.6. Nano-Dust interaction with the Interplanetary Medium

Dust potentially has a very important role in heliospheric processes. Plasma-dust interactions in the solar wind affect the composition, structure, and dynamics of both the solar wind and interplanetary dust cloud. A fundamental understanding of this mutual interaction can apply to other astrophysical systems as well. Nano-dust may play a critical role in this interaction due to its strong coupling to the solar wind. The nano-dust-solar wind interaction could lead to generation of inner source pickup ions and the coupling could also be responsible for the observed disturbances in the interplanetary magnetic field and transient events. This section gives a very general overview of the possible effects nano-dust have on the interplanetary medium.

2.6.1. Sources of Inner Source Pickup Ions

Pickup ions (PUIs) are neutral particles that are ionized and picked up by the solar wind. Inner source PUIs are distinguished from PUIs picked up farther from the Sun through their composition and velocity distribution. Inner source PUIs have been observed by the Ulysses mission, but their source remains unknown. Geiss *et al.* [1995] presented inner source PUI observations suggesting that dust particles orbiting the Sun release neutrals through solar UV radiation and sputtering by solar wind particles, which then become charged through photoionization or charge exchange. Such PUIs would be characteristic of the dust composition and were identified through the observation of C^+, Mg^+, and Si^+.

Measurements made by the Solar Wind Ion Composition Spectrometer (SWICS) indicate that inner source PUIs are a product of the interaction between IDPs and solar wind [*Gloeckler et al*., 2000]. The composition measured is similar to that of the solar wind and suggests that the PUIs are solar wind ions embedded in dust particles that are released as slow-moving neutrals.

Another potential mechanism could be ion penetration through a dust particle, energy reduction of the ion, and charge exchange to produce a PUI. Based on the analysis of inner source PUI velocity distribution functions, dust releasing the neutrals exist at ~0.05–0.2 AU [*Gloeckler et al.,* 2000] where the nano-dust population is expected to be largest. These observations hint that nano-dust plays a role in the generation of inner source PUIs.

2.6.2. Solar Wind Mass loading and Interplanetary Field Enhancements

Nano-dust strongly couples to the solar wind through the Lorentz force. The solar wind convection electric field accelerates the nano-dust, requiring the nano-dust to exchange momentum with the solar wind. This effect can potentially lead to shock formation or solar wind slow down in localized regions where there dust density is high. When a large amount of dust is released in a destructive collision of asteroid or cometary material, localized solar wind mass loading by the nano-dust cloud may be responsible for local distortions in the interplanetary magnetic field (IMF) known as Interplanetary Field Enhancements (IFEs). It is hypothesized that a cloud of nano-dust is generated during a localized catastrophic collision event. The nano-dust is picked up and accelerated by the convection electric field and, to conserve momentum, the solar wind protons are pushed antiparallel to this field, resulting in a distortion in the IMF that they are tied to [*Jia et al.,* 2012]. Such disturbances were observed during the passage of asteroid Oljato between the Sun and Venus. More recently, STEREO, WIND, and ACE have also detected these IMF disturbances [*Russell et al.,* 2010]. A similar warping of a coronal mass ejection (CME) magnetic field was observed when a CME encountered the dust trail of comet McNaught [*Russell et al.*, 2009].

2.7 Motivation and Open Questions

Dust is thought to play a critical role in the dynamics and evolution of the inner Solar System, though this role is not fully understood yet. Current understanding of the dust complex near the Sun is limited to zodiacal light observations and in situ measurements of near-ecliptic plane populations between 0.3 AU and 1 AU. The interplanetary dust flux models at 1 AU are paired with experiment-based collisional fragmentation laws to estimate fluxes within 1 AU. Further observations are necessary to determine dust sources, distribution, and collisional processes near the Sun. It is expected that nanometer-sized dust particles are generated near the Sun, but there still is no direct proof. If they exist, how do they form and in what abundance? A few outstanding science questions are: what are the sources and sinks of IDPs existing in the inner Solar System? What is the relative asteroid and cometary contribution? How do they evolve in size distribution/dynamics and what fraction is lost to the Sun through sublimation or sputtering vs. the fraction that is driven out of the Solar System through solar radiation pressure and solar wind pickup?

Furthermore, these particles interact with the interplanetary medium, affecting major heliospheric processes such as the dynamics, composition and structure of the solar wind. These are also unexplored, open questions. Fortunately, nano-dust and β-meteoroids are expelled out of the inner Solar System where they can be detected near Earth's orbit. They carry with them information about the origin, formation, distribution, and interactions of dust in the inner Solar System. The work described in this thesis presents the groundwork for measuring these particles and addressing the open questions.

Chapter 3: Nano-Dust Dynamics and Transport

3.1. Motivation

A numerical model has been developed to simulate dust dynamics in the inner Solar System and, in particular, to describe the dynamical interaction of charged nano-dust with the solar wind and how this interaction shapes nano-dust trajectories. Measurable features such as nano-dust velocity, directionality, flux, and the variability of these parameters are tell-tales of nano-dust interaction with the solar wind, and modeling provides the groundwork for interpreting measurements. The model is used to determine both nano-dust speed and angular distribution of their velocity vectors at 1 AU near Earth's orbit where a dedicated dust detector like the Nano Dust Analyzer (NDA) could detect them. The model results are also critical for determining instrument operation requirements. Furthermore, new insight is to be gained from nano-dust interactions with solar transient events that can uniquely alter their trajectories. In particular, nano-dust can be picked up by interplanetary coronal mass ejections (ICMEs), which significantly alter their dynamics and, in turn, can potentially affect the ICME magnetic field structure [*Russell et al.,* 2009]. This chapter will describe the model and how it is used to investigate the interaction between nano-dust and the solar wind (as well as ICMEs). It also presents results from the dust trajectory calculations that are later used to derive the NDA design and operation requirements, which are described in Chapter 4.

3.2. Model Description

The model described in this chapter has been adopted from that developed by *Juhasz and Horanyi* [2013] and is extended to allow the study of nano-dust interaction with ICMEs. In the model, individual dust particle trajectories are calculated by numerically integrating their equations of motion. The numerical calculations are performed in the Heliocentric Inertial (HCI) coordinate system, where the z-axis is centered on the solar rotation axis and the x-axis aligns with the solar ascending node on the ecliptic. The equations of motion below include the forces due to solar gravity, solar radiation pressure, and the solar wind Lorentz force. The Poynting-Robertson drag is not included in this model since the effect is negligible compared to the effect of solar radiation pressure for the time scales of interest.

$$\frac{d\vec{v}}{dt} = -\frac{GM_{Sun}(1-\beta)}{r^2}\hat{r} + \frac{Q}{m}(\vec{v}-\vec{w})\times\vec{B} \tag{3.1}$$

where Q, $\vec{v}$, and m describe the charge, velocity, and mass of the dust particle. G is the gravitational constant, M_{Sun} is the solar mass, r is the radial distance from the center of the Sun, and β is the ratio of solar gravity to solar radiation pressure. Here $\vec{w}$ describes the solar wind velocity and $\vec{B}$ describes the interplanetary magnetic field (IMF). In the model, it is assumed that a nano-dust particle in the inner heliosphere has a constant surface potential of Φ = + 5 V, corresponding to the equilibrium potential of a grain, in which the charging currents are expected to be dominated by photoelectron emission [*Mukai*, 1981]. Thus, the charge is then calculated for a spherical grain as $Q = 4\pi\varepsilon_0\Phi r_g$. In this model, the grain radius r_g is an input parameter and m is determined under the assumption that the particle has a density of ρ = 2 g cm^{-3}. For β-meteoroids, the function β (r_g) reported in *Landgraf et al.* [1999] for IDPs is used. For the full range of nano-

dust particles (< 100 nm), $\beta \sim 0.1$ is used. β is not known for nano-dust particles, but due to their small size compared to the radiation wavelength, the scattering efficiency is low and the absorption is proportional to the particle volume and mass, thus β is assumed to be constant [*Gustafson,* 1994].

In the basic model, the solar wind is assumed to flow solely in the radial direction at a speed of w = 400 km s^{-1}. This assumption of radial velocity is applicable to the region outside of the 'intermediate zone' located at ~10–20 R_{Sun}, where the magnetic field lines are assumed frozen in the plasma and convected by the plasma emitted from a point on the surface of the rotating Sun [*Schatten*, 1969]. Thus, the field shape forms a spiral-like configuration (see Fig. 3.1) described by the Parker field equation expressed in the following form [*Pei et al*., 2012].

$$\vec{B} = pB_0 \frac{r_0^2}{r^2}\left(\hat{r} - \frac{(r - r_{SS})\Omega_{Sun}}{w}\sin\theta\hat{\phi}\right)\left[1 - 2H(\theta - \theta_{CS})\right] \tag{3.2}$$

B_0 = 3.5 nT is the IMF magnitude at r_0 = 1 AU, (r, θ, ϕ) are the conventional spherical coordinates in the Heliocentric Inertial (HCI) coordinate frame where $\hat{r}$, $\hat{\theta}$, and $\hat{\phi}$ correspond to the unit vectors, H is the Heaviside step function, and θ_{CS} is the latitude of the heliospheric current sheet (HCS), Ω_{Sun} is the angular rotation rate of the Sun, and r_{SS} = 2.5 R_{Sun} is the radius of the solar wind source surface. p describes the polarity of the IMF and is opposite on either side of the HCS. The IMF polarity p reverses every 11 years with solar cycle. When p = +1, the convection electric field $\vec{E}_{EM} = -\vec{w} \times \vec{B}$ on either side of the current sheet points away from it. This is known as the 'defocusing configuration'. For p = -1, the field points toward the current sheet and is known as the 'focusing configuration'. The HCS, depicted in Fig. 3.1, represents the

boundary between IMF of opposite polarity and gives rise to the sector-structure of the IMF, which is important in shaping nano-dust trajectories. The HCS in this model is described by the surface that satisfies the following equation [*Pei et al.,* 2012]:

$$\tan(\frac{\pi}{2} - \theta_{CS}) = \tan\alpha(t,r)\sin\left(\phi - \phi_0 - \Omega_{Sun}t + \frac{\Omega_{Sun}(r - r_{SS})}{w}\right) \tag{3.3}$$

where θ_{CS} describes the latitude of the HCS and $\alpha(t,r)$ describes the tilt angle of the HCS with respect to the solar equator at time t and radial distance r. $\alpha(t)$ is obtained from the potential field source surface model (available from wso.stanford.edu/Tilts.html), which defines the maximum extent in latitude of the HCS on the solar wind source surface r_{SS} as a function of time [*Hoeksema,* 1995], which is assumed here to be the same in the northern and southern hemisphere. ϕ_0 represents the initial orientation of the rotating HCS. This model describes a two-sector IMF structure where a dust particle positioned above/below the tilted current sheet boundary experiences an IMF of opposite polarity. A more realistic alternative for modeling the HCS uses the Wilcox Observatory photospheric observations, which give the position $\theta_{CS}(r_{SS})$, $\phi_{CS}(r_{SS})$ of the neutral line on the source surface. Thus, the position of the footprint of the magnetic field line on the Sun that corresponds to the position of the dust particle can be calculated [*Juhasz and Horanyi,* 2013]. This method reproduces a more realistic sector structure and allows for the IMF polarity at the dust particle's position to be determined, but cannot be used to predict the shape of the HCS at future observation times. The model implementing the two-sector structure (Eq. 3.3) derived from $\alpha(t,r)$ from the potential field source surface model was used for the work reported in this chapter.

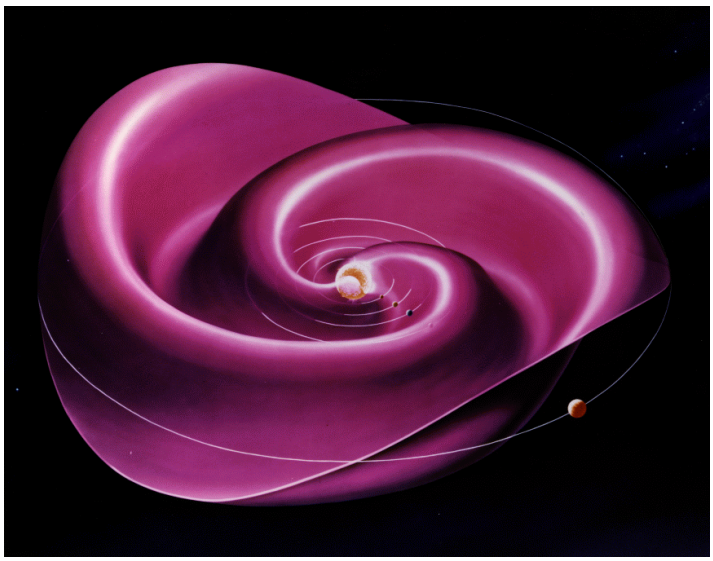

Figure 3.1. Depiction of the heliospheric current sheet (HCS). Solar rotation leads to a spiral shape of the IMF convected by the solar wind. The tilt of the Sun's magnetic dipole field relative to the solar rotation axis results in a wavy structure (courtesy of NASA).

3.3. Nano-Dust Pickup and Acceleration

Nano-dust particles are initially in Kepler orbits similar to that of their parent bodies. Shortly after generation, they are accelerated perpendicular to $\vec{B}$ by the convection electric field $\vec{E}_{EM} = -\vec{w} \times \vec{B}$. They are picked up and begin gyrating along the IMF field lines with a Larmor frequency $\Omega_L = |Q|B/m$ and Larmor radius $R_L = |\vec{v}_\perp - \vec{w}_\perp| / \Omega_L$ where $\vec{v}_\perp$ and $\vec{w}_\perp$ correspond to components of the nano-dust and solar wind velocity perpendicular to $\vec{B}$. The amplitude of their velocity oscillations is thus determined by $|\vec{v}_\perp - \vec{w}_\perp|$. The dust particle's velocity evolution is dependent on its distance from the Sun at the time of generation (pickup). Farther from the Sun, the azimuthal component of the IMF is large, so $w_\perp$ is large and the nano-dust particles oscillate in velocity with amplitudes reaching nearly twice the solar wind speed within one Larmor

rotation. The velocity oscillations decrease as the magnitude of $\vec{B}$ decreases with radial distance from the Sun. Nano-dust picked up closer to the Sun will not have as large initial velocity oscillations since the IMF is more radial in this region and they do not reach near-solar wind speed until they are farther from the Sun. Figure 3.2 shows the velocity evolution of a nano-dust particle picked up at 0.2 AU compared to one picked up at 0.5 AU, where their initial orbital velocities are ~ 66 km s^{-1} and 42 km s^{-1}, respectively.

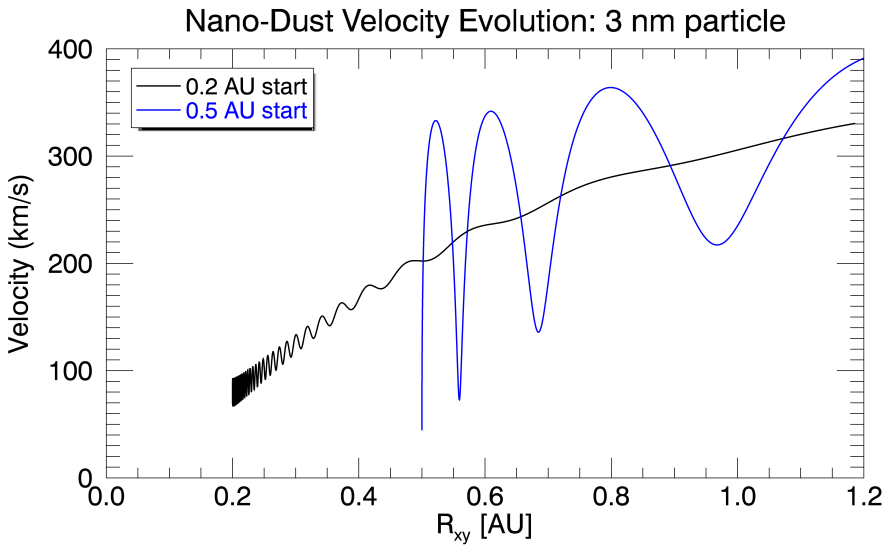

Figure 3.2. Velocity evolutions of 3 nm size dust particles picked up at 0.2 AU vs. 0.5 AU as a function of radial distance from the Sun. The velocity oscillations are much larger for the particle picked up at 0.5 AU due to the orientation of *B* relative to the solar wind plasma velocity.

3.4. Nano-Dust Transport Through the Guiding Center Approximation

Before discussing the trajectories calculated by the numerical model, a physical description of nano-dust dynamics is provided using the guiding center approximation, which is useful in the interpretation of the numerical results. The approximation is only valid for the smallest nano-dust (< ~10–15 nm) in a unipolar IMF region where the Larmor radius is much smaller than the scale of change of the IMF ~ $R_L << B/\nabla B$. The acceleration and energy gain of the nano-dust particles is provided by the convection electric field that results from the relative solar wind/IMF motion $\vec{E}_{EM} = -\vec{w} \times \vec{B}$ where $\vec{w} = w\hat{r}$ and $\vec{B} = B\hat{\phi}$, thus $\vec{E}_{EM} = E\hat{\theta}$. The gyro-center of the dust particle exhibits motion known as the guiding-center motion. The velocity of the guiding center is broken down into two components: $\vec{u}_g = \vec{u}_{\parallel} + \vec{u}_{\perp}$ where $\vec{u}_{\parallel}$ represents the guiding center velocity parallel to the magnetic field and $\vec{u}_{\perp}$ is the perpendicular component. $\vec{u}_{\perp}$ contributes largely to the total nano-dust velocity as well as its drift out of or toward the ecliptic plane and is expressed by the following equation [*Northrop*, 1961, 1963]:

$$\vec{u}_{\perp} = \vec{u}_{E\times B} + \frac{\hat{b}}{B} \times \left[\frac{\mu}{Q} \vec{\nabla} B + \frac{m}{Q} \left(-\vec{g} + u_{\parallel}^2 (\hat{b}\nabla)\hat{b} + u_{\parallel} (\vec{u}_{E\times B}\nabla)\hat{b} + u_{\parallel} (\hat{b}\nabla)\vec{u}_{E\times B} + (\vec{u}_{E\times B}\nabla)\vec{u}_{E\times B} \right) \right] \quad (3.4)$$

where the 1st term $\vec{u}_{E\times B} = \vec{E}_{EM} \times \vec{B} / B^2$ is the $E\times B$ drift velocity, which has components ($u_{E\times B\, r}$, 0, $u_{E\times B\, \phi}$), $\hat{b} = \vec{B} / B$ is the IMF unit vector, $\mu = m v_{\perp}^2 / 2B$ is the magnetic moment, and g is the gravitational acceleration. Some of the notable drift motions are the 2nd and 4th terms, which are due to the gradient and curvature of $\vec{B}$, and the 3rd term accounts for the drift due to the gravitational force.

The nano-dust total velocity is dominated by $\vec{u}_{E\times B}$, which can also be described as the solar wind velocity component perpendicular to the IMF, or $\vec{w}_{\perp}$. $\vec{u}_{E\times B}$ becomes increasingly radial with increasing distance from the Sun where B_{ϕ} increases. The smallest nano-dust (< 10 nm) wind tightly along the IMF as it spirals outward from the Sun. These particles reach ~ 300 km s^{-1} once they reach Earth's orbit and continue to approach solar wind speed as they travel beyond. The acceleration parallel to the magnetic field also contributes to the nano-dust velocity, but is not as large as $\vec{u}_{E\times B}$. Larger nano-dust (> ~10 nm) are not accelerated to such high velocities. Furthermore, large particles will have more significant drift motion in the vertical direction u_{θ} due to the m/Q dependence of some of the drifts shown in Eq. 3.4. The largest contribution comes from the $\hat{b}\times(\vec{u}_{E\times B}\nabla)\vec{u}_{E\times B}$ and $\hat{b}\times u_{\parallel}(\hat{b}\nabla)\vec{u}_{E\times B}$ terms [*Juhasz and Horanyi*, 2013]. The direction of the drifts depends on the IMF configuration. In defocusing configuration, the dust particles drift away from the HCS. Thus, the largest nano-dust particles will drift to higher latitudes. In focusing configuration, the drift is toward the HCS. Nano-dust that cross the HCS will be decelerated when they encounter the IMF of opposite polarity. This interaction reduces the speed of nano-dust and can induce a drift along the current sheet, especially if the current sheet is nearly flat and closely aligned with the solar equator, as it is during solar minimum. A particle will cross the HCS if the field line it is tied to is at a distance from the HCS that is within the particle's Larmor radius. It is also more likely for a large nano-dust particle to cross the HCS during focusing configuration when the particle drifts toward the HCS. These effects on the nano-dust trajectories are reflected in the results from the numerical modeling and will be discussed in Sec. 3.6.1.

The above description of nano-dust pickup by the solar wind applies to particles existing outward of ~0.15 AU. Inside of this region, the nano-dust are trapped in complex non-Keplerian

orbits around the Sun that result from the combined effects due to solar gravity, the magnetic mirror force, and centrifugal force [*Czechowski and Mann*, 2010]. The investigation here focuses on the nano-dust that are generated outside of this trapping region and accelerated outward from the Sun by the solar wind.

3.5. Initial Conditions

The initial orbits of nano-dust particles play an important role in their trajectories and distribution near Earth's orbit. There are two initial dust distributions used in this model: the circular ecliptic dust cloud and the more realistic circumsolar dust disk. In the former, nano-dust particles of uniform size are distributed uniformly around the Sun in the ecliptic plane in circular Keplerian orbits at some heliocentric distance (0.2 AU for example). These simplified initial conditions are useful in gaining a physical understanding of how the structure of the IMF influences nano-dust trajectories.

In the circumsolar dust disk distribution, the initial orbits of the nano-dust are described by the Kepler orbits of their parent bodies. As discussed in Sec. 2.1.4, it is assumed that most of the dust is distributed in a cloud concentrated close to the ecliptic plane. Nano-dust of uniform size are assigned random orbital elements: eccentricity ~ $0 < e < 0.01$, inclinations $i < 10°$, true anomaly, argument of periapse, and longitude of ascending node ~ $0° < \upsilon, \omega, \Omega < 360°$. The generation of nano-dust particles is restricted to 0.2 AU $< r <$ 0.3 AU distances from the Sun. This approximation is reasonable because the dust density and collision rate is expected to increase inversely with r, thus the largest nano-dust population is expected to exist close to the Sun. The lower limit of 0.2 AU is chosen due to the nano-dust trapping phenomenon that occurs inside this region. It should be noted that the modeling reported here focuses on the dynamical

effects of nano-dust-solar wind interaction and does not include realistic dust size and number density distributions that are based on dust collision/production models. Rather, each model run includes a uniform dust size to analyze the size-dependence of the dynamical interaction.

3.6. Numerical Model Results

The nano-dust trajectories are calculated using the model described in Sec. 3.2. This section explores the effects of dust size, IMF structure, and initial conditions (i.e., initial orbital elements and IMF/HCS configuration at time/location of pickup) on nano-dust dynamics. Nano-dust trajectories are traced to 1 AU and their distribution near Earth's orbit where they can be detected by a dust instrument such as NDA is investigated.

3.6.1. Trajectories and Distribution at 1 AU

The numerical model results reported here show that the distribution of nano-dust near Earth's orbit (upon reaching 1 AU) reflects a very strong spatial and temporal variability that is dependent on dust size, IMF configuration, and initial dust orbits/spatial coordinates. These results were reported in *Juhasz and Horanyi* [2013] and will be described here.

The numerically calculated dust velocity evolution as a function of dust size and pickup location corresponds well with the theoretical description provided in Sections 3.3 and 3.4. Figure 3.2 shows the velocity evolution of a 3 nm and 15 nm dust particle, corresponding to both focusing and defocusing IMF configurations. In defocusing configuration, the smallest nano-dust picked up close to the Sun exhibit velocity oscillations decreasing as they approach 1 AU and the total velocity (dominated by $u_{E\times B}$) increases to ~ 300 km s^{-1}. The 15 nm dust particles are not as efficiently accelerated by the solar wind and reach 1 AU with lower speeds. In focusing configuration, the HCS crossing effect is more pronounced for the 15 nm particles, which

quickly drift toward the HCS. They reach 1 AU with lower speeds compared to the defocusing case.

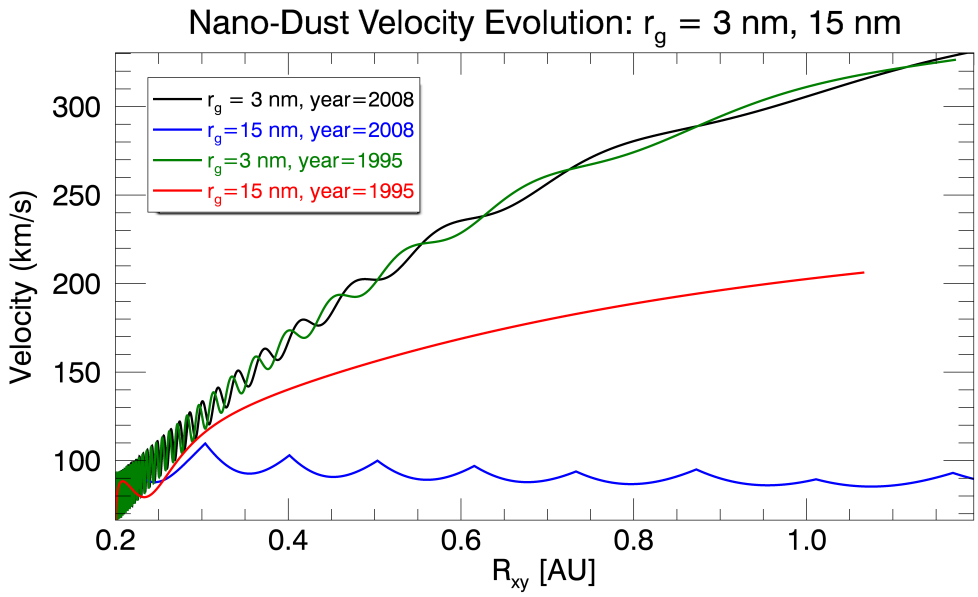

Figure 3.3 Velocity profiles of 3 nm and 15 nm dust particles started in circular Kepler orbits at 0.2 AU. The evolution depends on dust size and configuration of the IMF, which was in focusing configuration in 2008 and defocusing configuration in 1995.

These dynamical effects greatly shape the nano-dust fluxes at 1 AU and their potential for detection near Earth's orbit. With this in mind, the nano-dust trajectories are followed out to 1 AU where their azimuthal distribution ϕ (around the Sun) is evaluated. In the model, a 'near-earth orbit' (NEO) region is defined as $|r-1| \le 0.025$ where r (AU) is the radial distance from the Sun and $|z| \le 0.05$ where z (AU) here is the distance above or below the ecliptic plane (corresponding to a range in latitude of $\sim \Delta\theta = 3°$). NEO is somewhat arbitrarily chosen to

describe the region in which nano-dust could be detected near Earth's orbit from an observer in the ecliptic plane and highlights the spatial/temporal variability of nano-dust fluxes that a spacecraft orbiting at 1 AU in the ecliptic plane might observe [*Juhasz and Horanyi*, 2013].

To demonstrate the variability in distribution near Earth's orbit, the trajectories for nano-dust particles distributed at 0.2 AU in the uniform circular ecliptic distribution are followed out to 1 AU. The results are plotted using the Heliocentric Aries Ecliptic (HAE) coordinate system where the *x*-*y*-plane lies in the ecliptic plane and the *x*-axis aligns with the first point of Aries, and the *z*-axis is oriented perpendicular to the ecliptic plane. The nano-dust have uniform size and fixed *Q/m*. Figure 3.4 (top) shows the trajectories of 3 and 15 nm particles as viewed in the ecliptic (*x*-*y*) plane. Shown in red are the trajectories of the particles that reach the NEO region. Figure 3.4 (bottom) shows the azimuthal distribution ϕ (around the Sun) at 1 AU of the particles that pass through the NEO region. The number of nano-dust arriving at NEO as a function of ϕ is highly variable and it is clear that the initial position ϕ_i of the dust particle strongly affects whether or not the particle will reach NEO. This effect is most dramatic for small nano-dust, resulting in a nearly 180° periodicity in the azimuthal distribution, which can be explained by the 7.25° tilt of the ecliptic plane with respect to the solar equatorial plane. The small nano-dust particles thread closely along the rotating magnetic field lines and are displaced in azimuthal angle by $\Delta\phi = \phi_f - \phi_i$ where ϕ_f is the final azimuthal position of the particle at 1 AU. While the particle started in the ecliptic plane, its final latitude θ_f may be well above the ecliptic plane and not detectable in the NEO region due to the tilt.

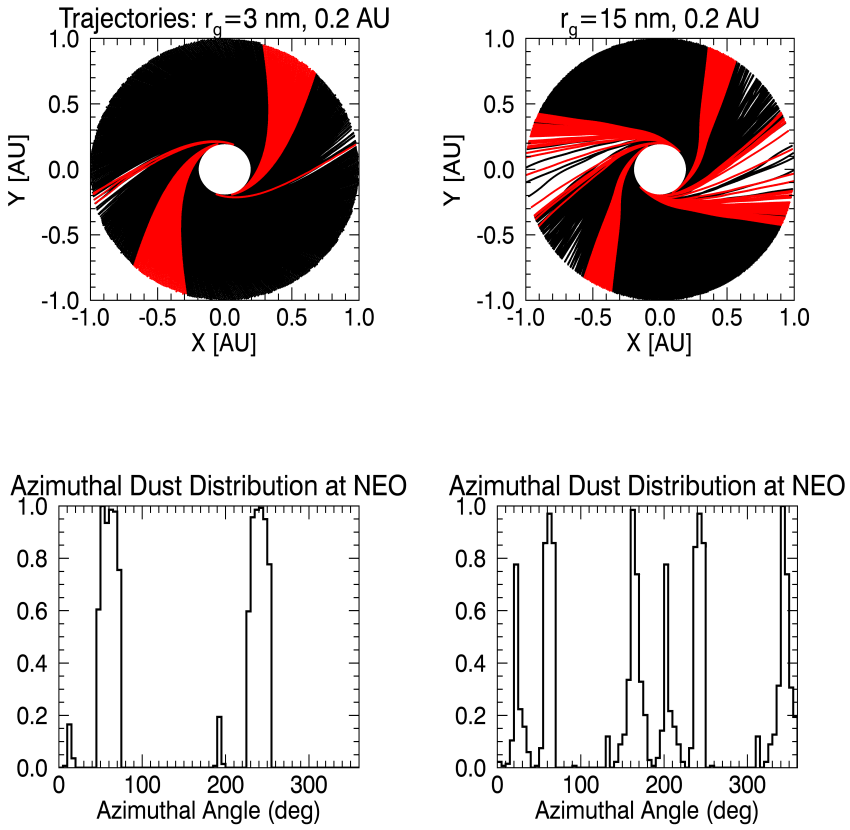

Figure 3.4 (Top) 3 nm and 15 nm dust trajectories in the ecliptic (*x*-*y*) plane. Initially, nano-dust particles are uniformly distributed around the Sun in circular orbits at 0.2 AU. Red lines are the trajectories of particles that reach NEO at 1 AU. Note the dependence of nano-dust reaching NEO on their initial azimuthal position around the Sun. (Bottom) The normalized distribution of nano-dust at NEO as a function of azimuthal position at 1 AU, showing strong variability. Note the nearly 180° periodicity in the distribution corresponding to the 3 nm particle. The result of larger nano-dust drifts in latitude is a small broadening of their azimuthal distribution at NEO.

The model is run with the circumsolar dust disk initial distribution to obtain a more realistic representation of the nano-dust trajectories and their distribution at NEO. As one might expect, the variability in the initial orbital parameters of the nano-dust results in a broadening of the azimuthal distribution at NEO, and the distribution varies as a function of nano-dust size due to the mass-dependent drift velocities (Fig. 3.5).

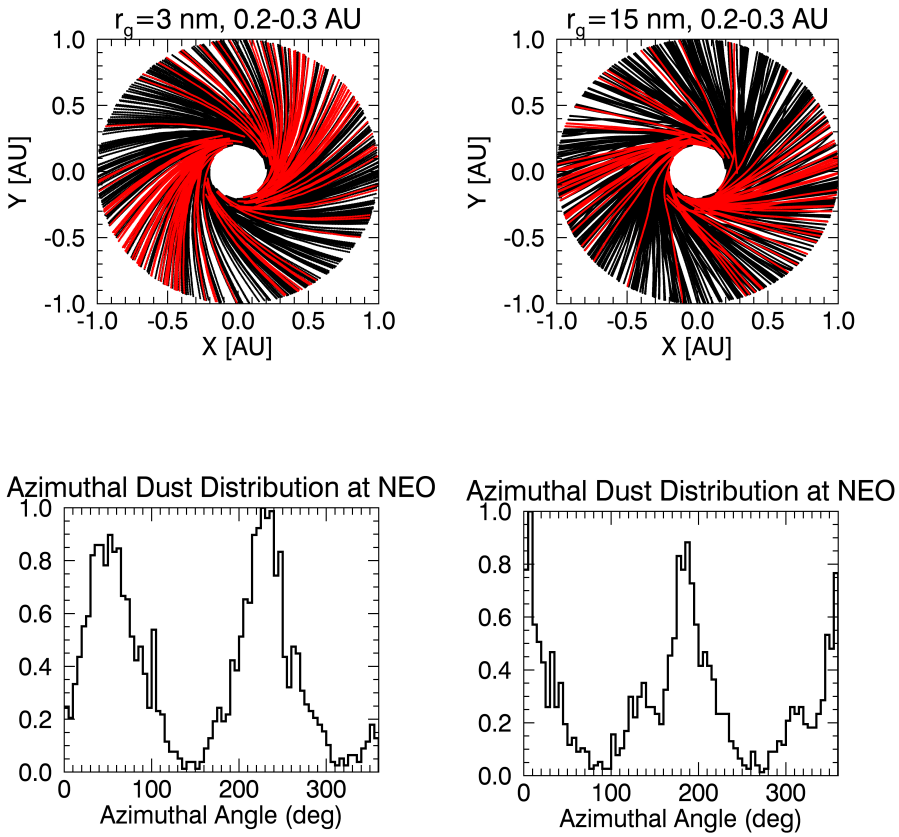

Figure 3.5 (Top) Trajectories of 3 nm and 15 nm particles with the circumsolar dust disk initial distribution around the Sun. Trajectories of nano-dust that reach NEO are highlighted in red. There is a wider range in initial azimuthal positions corresponding to nano-dust that reach the NEO region. (Bottom) Normalized azimuthal distribution of nano-dust at NEO is broadened for the case of random initial dust orbits and the distribution is dependent on dust size.

3.6.2. Trajectory Dependence on Initial Orientation of the HCS

The important dependence of nano-dust trajectories and distribution at NEO on the nano-dust initial orbits was discussed in Sec. 3.6.1. The initial conditions of the IMF also play a critical role in shaping the nano-dust trajectories and their distribution at NEO. In particular, ϕ_0 in Eq. (3.3) represents the initial orientation of the rotating current sheet, which defines the

azimuthal position corresponding to the latitude at which the IMF direction changes. ϕ_0 influences the azimuthal distribution of nano-dust at NEO. Figure 3.6 shows the azimuthal distribution for various values of ϕ_0 for a 5 nm particle. It is clear that the distribution of dust at NEO is highly variable with ϕ_0. The variation in the distribution is negligible for the smallest nano-dust particles (~1 nm), but becomes important for those that are 5 nm and larger. Figure 3.6 corresponds to the year 2007 when the IMF was in focusing configuration, but the variation is present when the IMF is in defocusing configuration as well. The value of ϕ_0 is a function of the observation time, and is defined arbitrarily in the model as $\phi_0 = 0$. However, it is important to point out that it contributes to the variability of the nano-dust distribution at NEO.

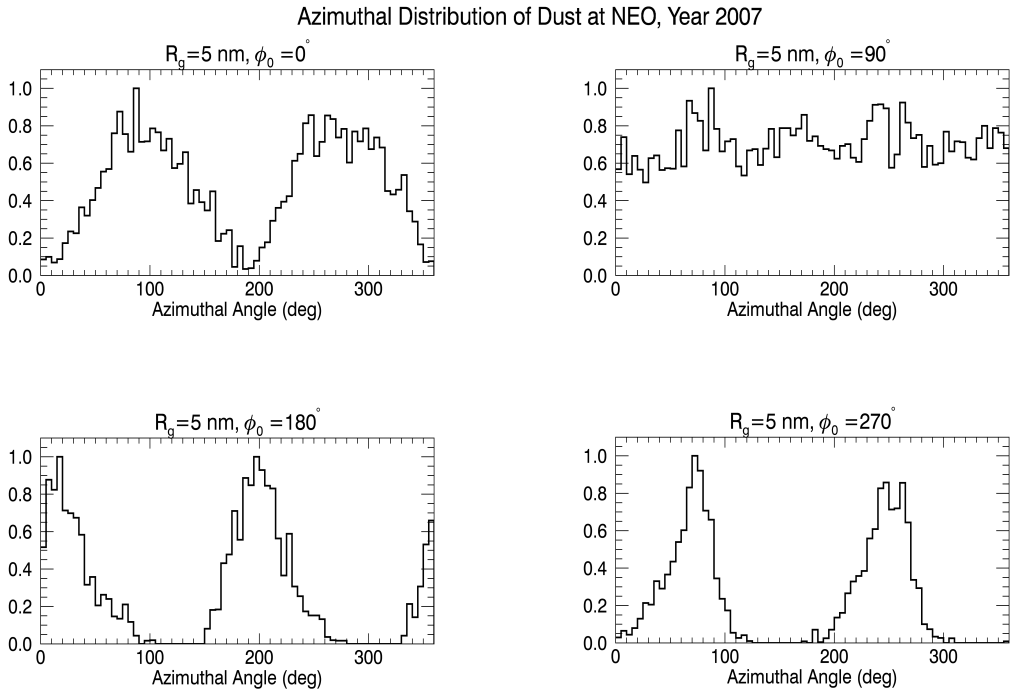

Figure 3.6 The azimuthal distribution of 5 nm particles at NEO with different initial HCS orientations ϕ_0. The NEO distribution varies greatly as a function of ϕ_0.

3.6.3. Velocity and Arrival Direction of Nano-Dust Near Earth's Orbit

The nano-dust velocity distribution and arrival directions in the NEO region are determined using the trajectories calculated with the numerical model and were first reported in *O'Brien et al* [2014]. These parameters are critical for designing the Nano Dust Analyzer instrument, as well as its accommodation on a platform and observational strategy in future missions. Specifically, the calculated distributions are used to define the NDA requirements, e.g., instrument pointing, FOV, sensitivity and dynamic range.

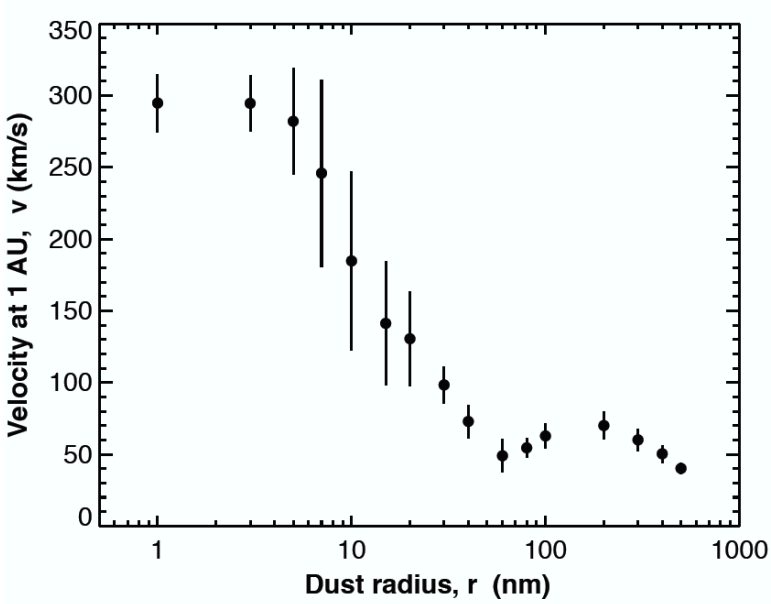

Figure 3.7 Velocity distribution of nano-dust and *β*-meteoroids reaching Earth's orbit. Error bars represent the spread in velocity described by a 1 *σ* standard deviation. Velocity decreases as nano-dust size increases. The dynamics of the larger *β*-meteoroids (100-500 nm) are governed by solar radiation, resulting in a local maximum in velocity.

Figures 3.7 and 3.8 show the velocity distribution and angular distribution of the velocity vector of the nano-dust that reach the NEO region, respectively. The size distribution was extended to include the β-meteoroids since they can also be detected by the NDA. The numerical model was run for the year 2007, in which the IMF was in focusing configuration. A large number of dust particles of uniform size are initialized in the circumsolar dust disk distribution and the dust trajectories are traced to 1 AU. Only particles that reach the NEO region are included in the distribution shown. Figure 3.7 shows that the smallest particles (1–5 nm) are accelerated efficiently and arrive at NEO with a narrow velocity distribution centered at about 300 km s^{-1}, while the spread of velocities is wider for larger particles that drift more in the vertical direction. The total velocity decreases with increasing dust size, supporting the discussion in Sec. 3.3. The β-meteoroid portion of the distribution (~100–500 nm) shows a local maximum in velocity where the radiation pressure effect is strongest.

The angular distribution in velocity of these particles is calculated and plotted in Figure 3.8. The 'azimuth' describes the angle, within the ecliptic plane, between the dust particle and the solar radial direction as seen from a platform orbiting the Sun at 1 AU. This quantity is calculated as $\tan\alpha = v_\phi / v_\rho$ where v_ϕ is the azimuthal component of the dust velocity, corrected for Earth's orbital velocity so that the velocity is realized in Earth's frame of reference, and v_ρ is the radial component of the dust velocity at 1 AU. The 'zenith' describes the angle above/below the ecliptic plane at which the dust arrives at 1 AU and is calculated as $\tan\delta = v_\phi / v_{\rho\phi}$ where $v_{\rho\phi} = \sqrt{v_\rho^2 + v_\phi^2}$. Figure 3.8 shows that the distribution span is limited to < 40° from the Sun's direction for all particles. The smallest nano-dust are bound tightly to the IMF and arrive at 1 AU in or close to the ecliptic plane and about 20° from the Sun's radial direction. The larger dust particles are distributed over a wider range in zenith due to their motion in the vertical direction.

The symmetry of the distribution in zenith results from the trajectories being averaged over an entire Earth's orbit around the Sun. Thus, the arrival direction of nano-dust (above or below the ecliptic plane) depends on the orientation of the IMF at that point in space and time. These results are reported for the year 2007 when the IMF was in focusing configuration. The arrival directions do not differ much when the IMF is in defocusing configuration, however, because the particles that are outside of the NEO region are not included in the distribution. The large nano-dust will drift away from the ecliptic plane during a defocusing period and fewer of these particles will reach the NEO region, so the detected fluxes and size distribution will be different from a focusing period.

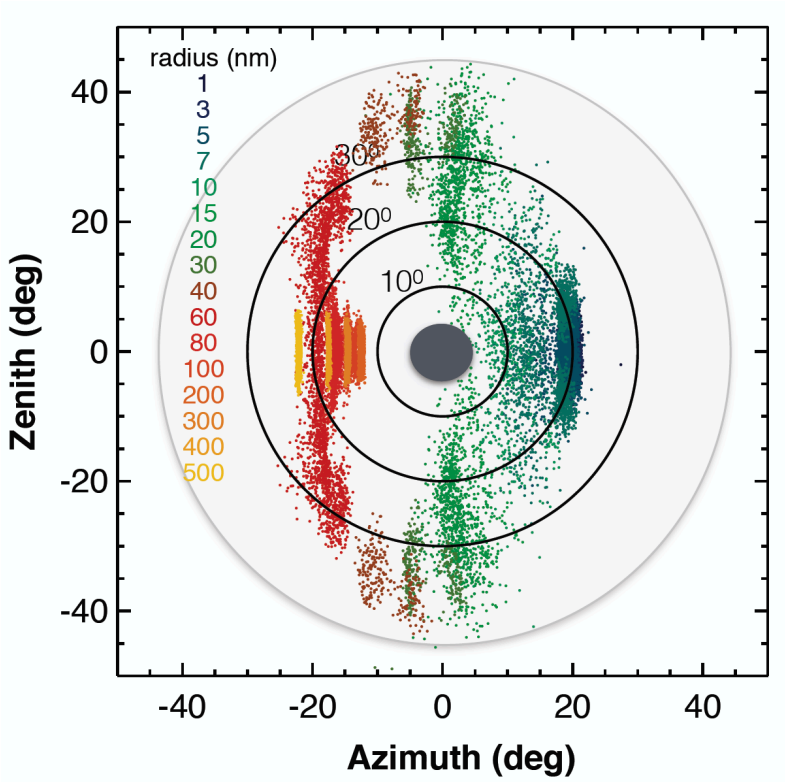

Figure 3.8 Arrival directions of nano-dust and *β*-meteoroids that reach NEO, as a function of their size. The Sun is depicted at the center. The azimuth is the angle from the Solar radial direction and the Zenith is the angle above/below the ecliptic plane. Note the smallest nano-dust arrive in or near the ecliptic plane from close to the Sun and the larger nano-dust spread over a wider range of zenith angles. The arrival directions plotted here are as seen from Earth.

The *β*-meteoroids are expelled radially outward by radiation pressure and arrive at 1 AU nearly in the ecliptic plane. They arrive at increasingly negative angles with respect to the solar radial direction because the radial acceleration of these particles increases with β and the azimuthal component of the *β*-meteoroid velocity runs behind Earth's orbital velocity. In the plot, there are also distributions corresponding to dust particles that are in a transition phase between nano-dust and *β*-meteoroids (~50–100 nm) where the motion is a function of both the Lorentz force and solar radiation pressure.

The angular distribution in Fig. 3.8 has major implications for the observation strategy of the nano-dust particles by the NDA instrument. First, as it will be shown later, NDA can operate only when the Sun is excluded from the instrument field-of-view (FOV), thus the different dust populations cannot be observed simultaneously and scanning is necessary. The simplest observation strategy appears to be a spinning platform with a spin axis pointed at the Sun. Second, NDA will need to point close to the solar radial direction (~20–25°) and have a sufficiently large FOV to encompass all populations shown in Fig. 3.8. The predicted velocity distribution shown in Fig. 3.7, on the other hand, is a key factor in determining the instrument sensitivity, ion optics properties, and detector dynamic range, for example. These requirements/constraints and their implications for NDA instrument design and operation will be discussed in more detail in Chapters 4 and 5. It is, however, important to point out that the dust velocities and arrival directions near Earth's orbit reported here are based on a simplified model of the solar wind and IMF/HCS structure and do not take into account the fast solar wind and other variable solar wind conditions. It also does not include the high latitude dust distribution and/or spatial variations of their sources. Nevertheless, the estimates make it clear that nano-dust are expected to arrive from a range of directions, including the near-solar radial direction, and NDA must be able to accommodate these distributions.

3.7. Nano-Dust Interaction with Interplanetary Coronal Mass Ejections (ICMEs)

3.7.1. Overview

The work presented in this section is based on the study by *O'Brien et al*. [2017] of nano-dust dynamics/trajectories through their interaction with interplanetary coronal mass ejections. Sections 3.1–3.6 describe the modeling of nano-dust dynamics through their interaction with the

solar wind and, as a result, their trajectories to 1 AU. However, the effect of temporal or spatial variability in the IMF due to solar activity on dust dynamics has not been addressed in the original model. Solar transient events introduce unique magnetic structures and generate temporary disturbances in the outflowing solar wind. Coronal mass ejections (CMEs), co-rotating and stream interaction regions (CIRs, SIRs) are examples of such events. This section investigates the interaction of nano-dust with CMEs propagating through interplanetary space, known as interplanetary coronal mass ejections (ICMEs). ICMEs are large clouds of plasma and magnetic field launched from the Sun into the solar wind and could significantly alter the dust dynamics and trajectories upon encounter. Nano-dust, in turn, can potentially disturb the ICME magnetic field structure through pickup and mass-loading effects [*Russell et al.,* 2009].

The influence of ICMEs on the motion of interplanetary dust particles (IDPs) that are nanometer–micron in size have been previously explored [*Ragot and Kahler*, 2003; *Wagner et al*., 2009]. However, the interaction between nano-dust and ICMEs and their effect on nano-dust transport, which could be quite strong, has remained largely unexplored. *Russell et al*. [2009] proposed that observed structural changes in the ICME magnetic field might be a result of nano-dust being picked up and accelerated by ICMEs and that ICME acceleration of nano-dust could be a likely mechanism of clearing out dust in the inner Solar System. Furthermore, *Le Chat et al*. [2015] reported an increase in the frequency of the voltage signals observed by STEREO at 1 AU (interpreted as nano-dust impacts, see Sec. 2.4.2) corresponding to periods of observed ICMEs. These results suggest that an ICME can effectively pick up and deliver a large, concentrated flux of nano-dust to a spacecraft during its passage. If this is true, the effect could be observable in nano-dust flux measurements, and if the ICME magnetic field is measured simultaneously, their interaction could be correlated.

The investigation reported in this section is a pilot study to develop a physical understanding and a first-approximation of the interaction of nano-dust with ICMEs. The questions investigated here are: (1) How can nano-dust dynamics be altered by interaction with ICMEs? (2) Is it possible for an ICME to deliver nano-dust to the NEO region, and in large quantities? (3) How will a more realistic global ICME structure affect the nano-dust delivery to NEO? (4) Is it possible for NDA to detect the nano-dust fluxes delivered by the ICME? It is important to point out that a representative and realistic model of the interaction and measurable distribution at 1 AU would require a continuous source of nano-dust with a realistic size distribution. Here, only the trajectories of nano-dust generated in one instant and of uniform size are followed through their interaction with the ICME. Furthermore, the ICME shapes and geometries used are approximate forms of the true structure, and their effect on the surrounding solar wind has not been taken into account. Nonetheless, the study provides insight into the dynamical effect ICMEs can have on nano-dust and the conditions that can result in their delivery to NEO.

The study focuses on nano-dust interaction with magnetic clouds, which are a subclass of ICMEs. Their properties, while only partially understood, are better recognized than the broader class of ICMEs. Magnetic clouds can be described as twisted magnetic flux tubes carrying large amounts of magnetic helicity, flux, mass, and energy from the Sun out into interplanetary space. Their structure is described by a large magnetic field strength, smooth magnetic field vector rotation through a large angle (nearly 180°) and low proton temperature [*Lepping et al.,* 1990]. Thus, due to their low plasma beta (i.e., the ratio of magnetic pressure to plasma particle pressure), the magnetic field structure can be described by a force-free flux rope configuration

[*Burlaga,* 1988]. Locally, the magnetic cloud exhibits cylindrical symmetry, but has a global structure that is curved and possibly terminates back at the Sun, as shown in Fig. 3.9.

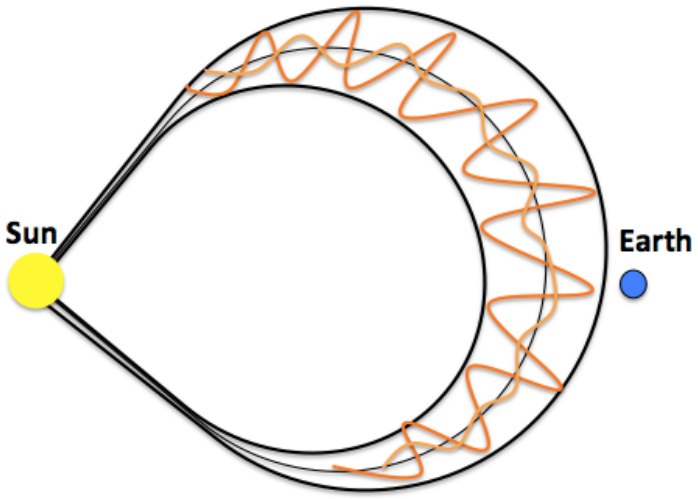

Figure 3.9 Global structure of a force-free magnetic cloud with local cylindrical symmetry, which has propagated out toward Earth's orbit. The curved line in the center represents the axial component of the flux rope field and the oscillating lines represent the azimuthal component. The true global shape likely deviates from the idealized depiction shown here.

3.7.2. Magnetic Cloud Modeled as a Cylindrical Force-Free Flux Rope

The magnetic cloud model adopted for this analysis is that of a cylindrical force-free flux rope. A force-free magnetic field is one in which the Lorentz force vanishes, and thus can be described by the current density in the plasma J being parallel to the magnetic field B. The solution is described as a magnetic field $\vec{B}$ satisfying the relationship: $\vec{\nabla} \times \vec{B} = \alpha \vec{B}$, where the factor α is generally a scalar function of the spatial coordinates [*Burlaga,* 1988]. The solution

used in this model is that presented by *Lundquist* [1950], which describes a cylindrically symmetric force-free flux rope with constant α:

$$\begin{aligned} B_A &= B_0 J_0(\alpha R) \\ B_\theta &= H B_0 J_1(\alpha R) \\ B_r &= 0 \end{aligned} \tag{3.5}$$

where B_A describes the component of the field in the direction of the cloud's axis, B_θ describes the azimuthal component and B_r is the radial component, all in the cylindrical coordinate frame (r, θ, z). B_0 describes the strength of the magnetic field along the axis, and $H = \pm 1$ is the direction of rotation of B_θ. The axial and azimuthal fields are described by 0^{th} and 1^{st} order Bessel functions of the first kind. These solutions describe a flux rope where $B_A = B_0$ and $B_\theta = 0$ on the axis. B_A decreases and B_θ increases with radial distance from the axis R, so that $B_A = 0$ and $B_\theta = B_0$ at $R = R_0$ where R_0 is the radial boundary of the flux rope. Thus the boundary condition $B_A = 0$ at $R = R_0$ yields $\alpha = 2.4048/R_0$. The simple solution described above has provided good fits to a number of magnetic cloud observations made at 1 AU, though the model better fits the observed structure/direction than the actual variation in strength of the magnetic field [e.g., *Burlaga,* 1988; *Lepping et al.,* 1990]. Still, the solution provides a good first-approximation of the magnetic cloud structure that a nano-dust particle will interact with.

The ICME (magnetic cloud) structure described above is incorporated into the existing dust dynamics model. When a nano-dust particle is inside of the ICME boundary, it interacts with only the ICME structure. Outside of the ICME, the regular solar wind is assumed for the dust trajectory calculations. Figure 3.10 depicts the ICME geometry in the Heliocentric Aries Ecliptic (HAE) coordinate system. The ICME propagates through interplanetary space with a

bulk velocity typically varying between 300 and 900 km s^{-1} [*Vandas et al.,* 2015]. *Le Chat, et al.,* [2015], for example, reports that STEREO measured enhanced nano-dust fluxes during ICMEs propagating at 300-400 km s^{-1}, thus a modest bulk velocity of 400 km s^{-1} is initially assumed in this model. The ICME expands as it propagates outward from the Sun, which is driven through its force balance with the surrounding solar wind. The total solar wind pressure decreases with distance from the Sun, thus, the flux rope expands and its internal pressure decreases to balance the pressure from the solar wind. Magnetic flux conservation then drives the magnetic field strength to also decrease with distance.

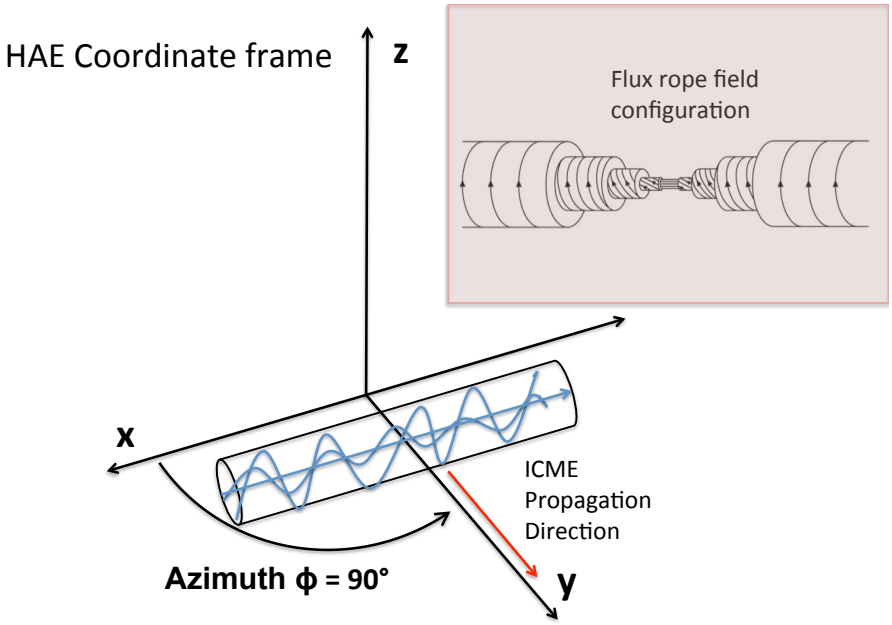

Figure 3.10 Depiction of a cylindrically symmetric flux rope geometry, axis orientation, and propagation direction in the Heliocentric Aries Ecliptic (HAE) coordinate frame. The flux rope propagates at along +*y* axis at azimuthal angle 90°.

In this model, it is assumed that the ICME expands uniformly and self-similarly. The evolution/expansion of the flux rope is described by the following equations:

$$R_0(t) = R_0(t_0) + v_{\exp}(t - t_0) \tag{3.6}$$

$$B_0(t) = B_0(t_0)\left[\frac{R(t_0)}{R(t)}\right]^2 \tag{3.7}$$

where $R_0(t_0)$ is the radius of the flux rope at the start of its propagation and v_{exp} is the expansion velocity of the radial boundary, which contributes to the radial velocity as $v_r(R) = (R/R_0)v_{exp}$ [*Wang et al.,* 2015]. $B_0(t_0)$ is the magnitude of the magnetic field along the ICME axis at the initialization time/position of the ICME. $R_0(t_0)$ and $B_0(t_0)$ (at $r = r_0$, where r is the radial distance from the Sun) are approximated using the power law relationships, $B_0(r) = 18.1r^{-1.64}$ (nT) and $R_0(r) = 0.24r^{-0.78}$ (AU) and an expansion speed $v_{exp} = 0.12v_{ICME}\, r_{Sun}{}^{-0.39}$ (km s^{-1}) is used, which are all derived from statistics of data obtained from Helios 1 and 2, WIND, PVO, ACE, and Ulysses, which measure ICME properties between 0.3 and 5.4 AU [*Leitner*, 2007 and *Wang*, 2005]. The ICME is centered in the ecliptic plane with B_A oriented perpendicular to its propagation direction, which is the x-axis (Fig. 3.10). ICMEs propagate outward from the Sun with a range of orientations and propagation directions, which vary in their influence on nano-dust trajectories.

3.7.3. Nano-dust interaction with ICMEs

In this section, a physical description of the interaction between nano-dust and ICMEs is discussed to elucidate the numerical model results that will be presented in the next section. The nano-dust interaction with an ICME can be explained in the same way as the interaction with the solar wind (described in Sec. 3.3). Nano-dust particles are picked up by the ICME and undergo

velocity oscillations with amplitude ~ $\left|\vec{v}_{\perp} - \vec{v}_{ICME,\perp}\right|$ where $\vec{v}_{ICME,\perp}$ is the component of the ICME plasma velocity perpendicular to the magnetic field. Thus, if $\vec{v}_{ICME,\perp}$ is large compared to $\vec{v}_{\perp}$, the dust velocity oscillations will also be large. The frequency of oscillations decreases as the magnetic field strength decreases with distance from the Sun.

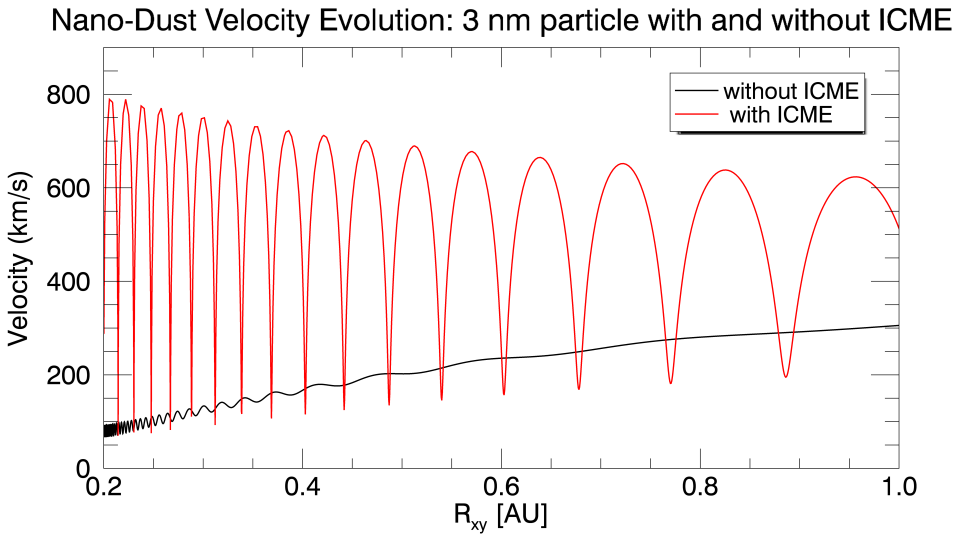

Figure 3.11 Velocity evolution of a 3 nm dust particle born in the center of an ICME propagating at 400 km s^{-1} perpendicular to its axis (red) vs. a 3 nm particle interacting with the regular solar wind. Note the large velocity oscillations of the particle picked up by the ICME.

Here, the guiding center approximation is valid for small nano-dust (< ~10 nm) interacting with the ICME. The largest contribution to the nano-dust velocity is also from the drift velocity $\vec{u}_{E\times B} = \vec{E}_{EM} \times \vec{B} / B^2$ where $\vec{E}_{EM} = -\vec{v}_{ICME} \times \vec{B}_{ICME}$. If $v_{ICME\perp}$ is large, the dust particle will initially have velocity oscillations with amplitude $v_{\max} \approx 2u_{E\times B} \approx 2v_{ICME,\perp}$ (as shown in Fig. 3.11). The x, y, and z components of $\vec{u}_{E\times B}$ (in the HAE frame) are dependent on the relative

magnitude of B_A and B_θ (i.e., they depend on the position within the ICME). Additional drift motion is introduced by the magnetic field gradient and curvature drifts: $\vec{u}_{cg} = (m/2QB)(v_\perp^2 + 2v_\parallel^2)(\vec{B} \times \vec{\nabla} B / B^2)$. For a cylindrical ICME, $\vec{\nabla} B$ is in the $\hat{r}$ direction, so $\vec{u}_{cg}$ is along the flux rope surface, perpendicular to $\vec{B}$ and the dust particle will not escape the flux rope through these drifts [*Krittinatham and Ruffolo,* 2009].

3.7.4. Numerical Model Results

ICMEs with the field structure and evolutionary properties described in Sec. 3.7.2 are incorporated into the existing model and nano-dust trajectories are followed out to 1 AU. The dust particles are initially distributed in the circumsolar dust disk, i.e., randomly distributed around the Sun with distances between $0.2 < r < 0.3$ AU, $e < 0.01$, and $0° < i < 10°$ (described in Sec. 3.5). The expanding cylindrical ICME is launched at 0.2 AU and initially has a radius of 0.04 AU, thus a fraction of the nano-dust are initially distributed inside of the ICME and a fraction lie outside of it. Particles distributed in front of the ICME can get picked up as the ICME passes through them. All particles are initially traveling at velocities corresponding to their Kepler orbits. The particles initially starting within the ICME represent nano-dust that have been produced within the ICME.

The trajectories of the particles interacting with the ICME are compared to those that do not. The modeling is mostly focused on ICMEs that propagate in or nearly in the ecliptic plane, perpendicular to their axis (as shown in Fig. 3.10), which are likely to deliver an enhanced nano-dust flux to NEO. Due to the magnetic field structure and the radial expansion of the ICME, the dust trajectories/velocity profiles will depend on their location within the ICME. Figure 3.12 shows the velocity evolution of 3 nm dust particles that are picked up at varying locations within the ICME.

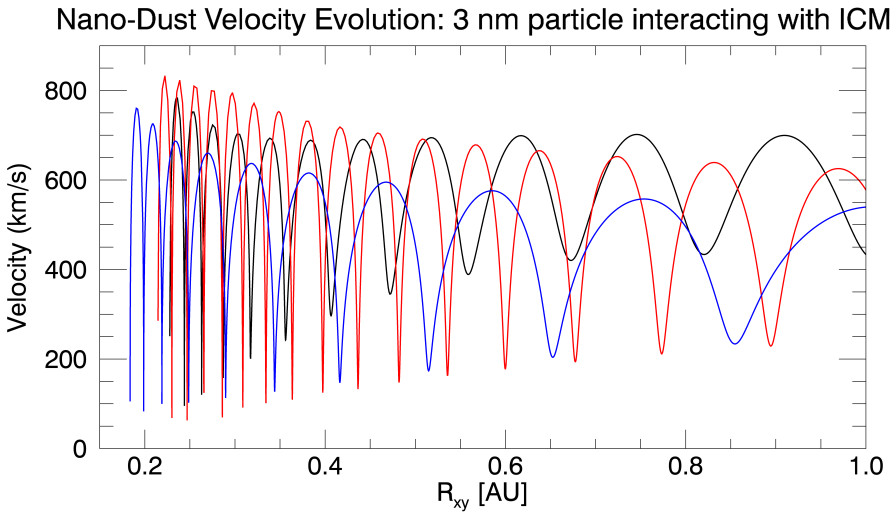

Figure 3.12 Velocity profile of 3 nm particles born within an ICME traveling at 400 km s^{-1}. The different colors represent the velocity evolution of different particles picked up by the ICME. The variation in the velocity evolution of each particle is a result of the particles starting in different positions within the expanding ICME.

Figure 3.13 shows the nano-dust trajectories from a model run in which a cylindrical ICME is launched at 0.2 AU and propagates at a modest speed of 400 km s^{-1} in the $+y$ direction. The ICME has the orientation shown in Fig. 3.10. The integration time step is 600 seconds and the coordinates are plotted every 10 time steps. The two trajectory plots (top) of Fig. 3.13 correspond to a model run in which nano-dust were initially distributed uniformly around the Sun in circular orbits in the ecliptic plane at 0.2 AU. The (bottom) trajectory plots correspond to a model run using the circumsolar dust disk initial distribution described above. The trajectories belonging to nano-dust that interact with the ICME are highlighted in red and the positions at which they are inside of the ICME are labeled in blue.

The top plots show some basic characteristics of the trajectories of nano-dust interacting with the ICME. The motion is dominated by $\vec{u}_{E\times B} \parallel \vec{v}_{ICME} = u_{E\times B}\hat{y}$. The trajectories also include

the smaller contribution from their initial Kepler velocities and motion parallel to the field, as well as the $u_{E\times B}\hat{x}$ and $u_{E\times B}\hat{z}$ drift components that are a function of $\vec{B}$ and the ICME bulk and the radial expansion velocities. The drift $\vec{u}_{cg}$ contributes to the particle motion along the flux rope surface. The particles born near the edges of the ICME escape, however, most particles remain inside of the flux rope throughout its propagation to 1 AU. Particles born along the ICME axis remain close to the ecliptic plane throughout their trajectory to 1 AU, thus they are most likely to reach the NEO region. The bottom plots of Fig. 3.13, which correspond to an initial dust distribution in the circumsolar disk, reflects a wider range of initial positions in the ICME and a fraction of the initial distribution is generated outside of the ICME. The dust trajectories are still dominated by $\vec{u}_{E\times B} \parallel \vec{v}_{ICME}$, but have a larger dispersion in their trajectories.

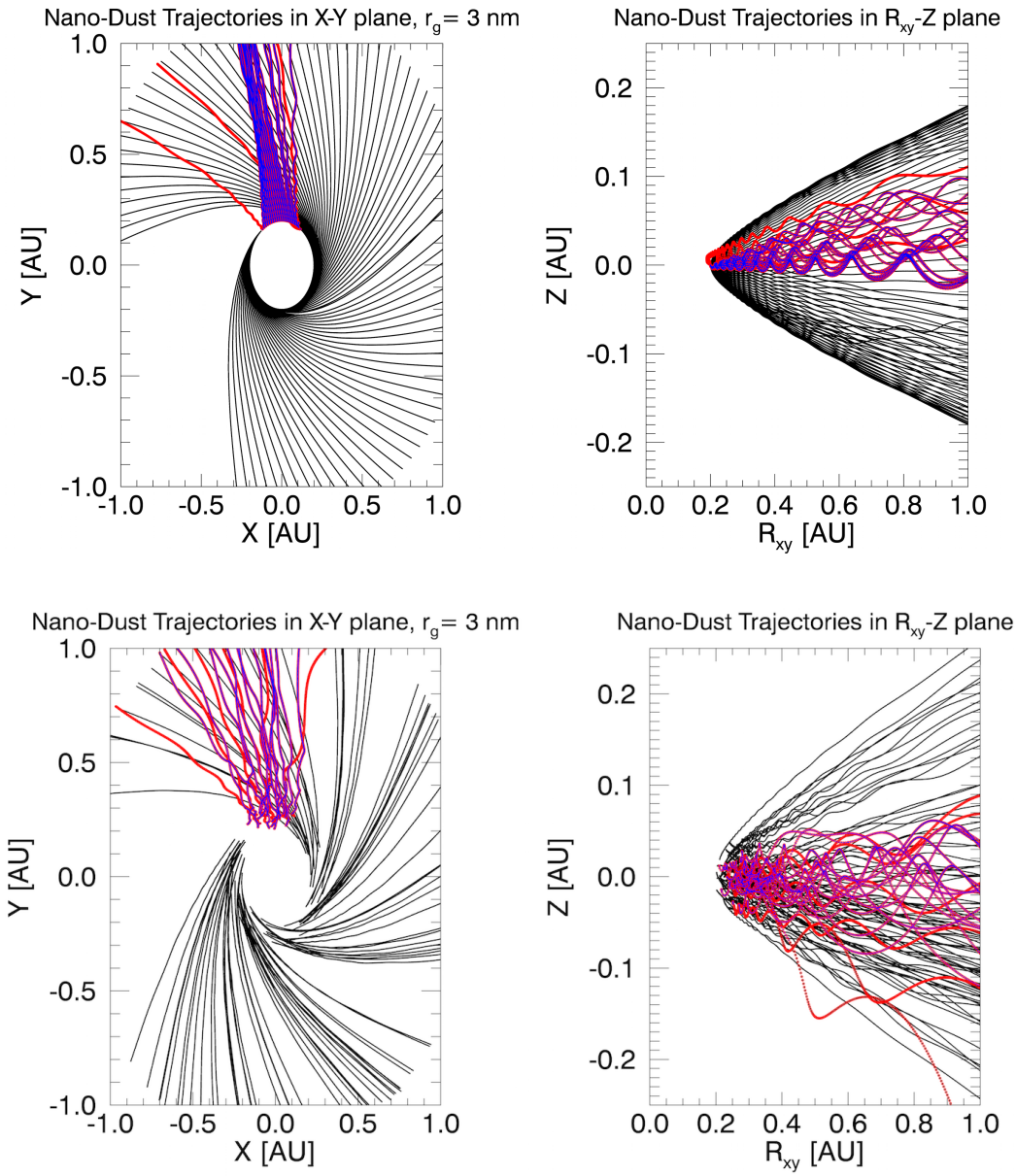

Figure 3.13 Nano-dust trajectories to 1 AU with ICME-included model (Top, left) Trajectories (viewed in the *x-y*/ecliptic plane) of 3 nm particles initially distributed uniformly in the ecliptic plane at 0.2 AU. The red traces are the trajectories of nano-dust that interact with the ICME and blue traces are the positions at which the nano-dust are inside of the ICME. (Top, right) Trajectories viewed from the R_{xy}-Z plane showing that nano-dust interacting with the ICME stay close to the ecliptic plane. (Bottom, left and right) Nano-dust trajectories for the more realistic circumsolar disk initial dust distribution (see text for details). Note, the nano-dust are initially distributed randomly inside and outside of the ICME in this case and thus, have a wider spread in the directions of their trajectories.

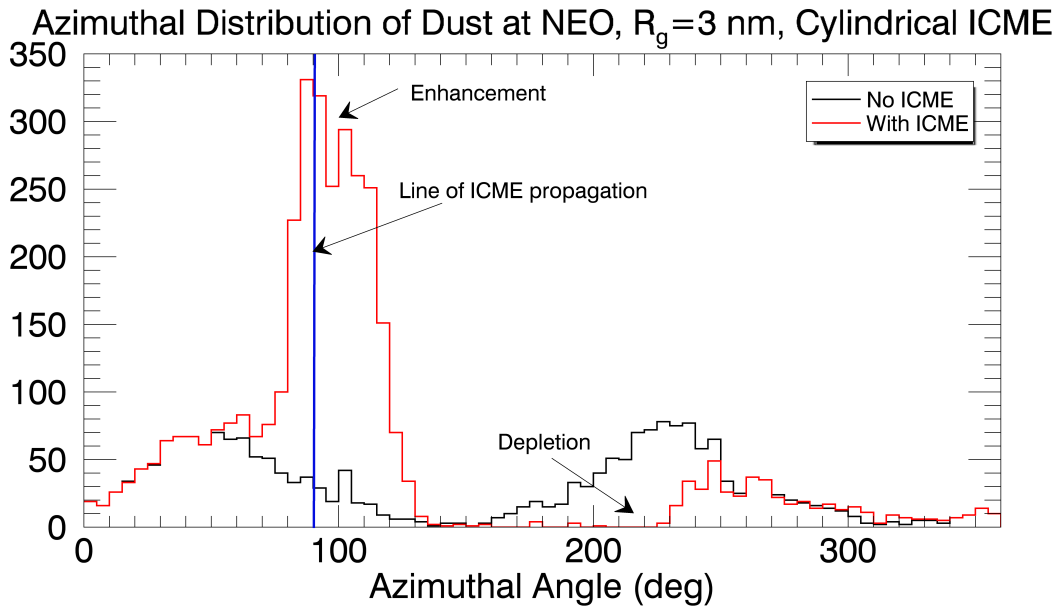

Figure 3.14 Azimuthal distribution of 3 nm particles that reach the NEO region with and without an ICME. 10,000 particles are initially launched in the circumsolar dust disk distribution and only a fraction of them reach NEO. The red histogram shows a clear enhancement in the flux at NEO near 90°, along the line of the ICME propagation. Note the flux depletion in other regions that is caused by the ICME clearing out nano-dust. For comparison, the black histogram plots the distribution for a model including the regular solar wind but no ICME.

Figure 3.14 shows the number of nano-dust particles reaching the NEO region as a function of azimuthal angle around the Sun for the models with and without an ICME. Both models are run with 10,000 3 nm-sized particles distributed in the circumsolar dust disk. The ICME conditions used are the same as that corresponding to the trajectory plots of Fig. 3.13. There is a clear enhancement in the number of nano-dust particles reaching NEO near 90°, which is the azimuthal angle corresponding to the ICME's line of propagation (see Fig. 3.10). The spread in this distribution is attributed to the variable initial positions of nano-dust inside and out of the ICME, which ultimately affect their motion in the *x*, *y*, and *z* directions (as can be seen in Figure 3.13). The interaction is strongest for the smallest nano-dust particles (< 10 nm). Large

particle trajectories are still altered by the ICME, but they quickly escape due to their large Larmor radii. Figure 3.15 shows the trajectories of 15 nm dust particles and also shows the azimuthal distribution at NEO for a number of dust sizes. The model was also run for the case where the ICME was launched 0.5 days later than the dust, showing that nano-dust accelerated by the solar wind prior to an ICME encounter can still be picked up and delivered to NEO, albeit in a lower concentration (Fig. 3.16).

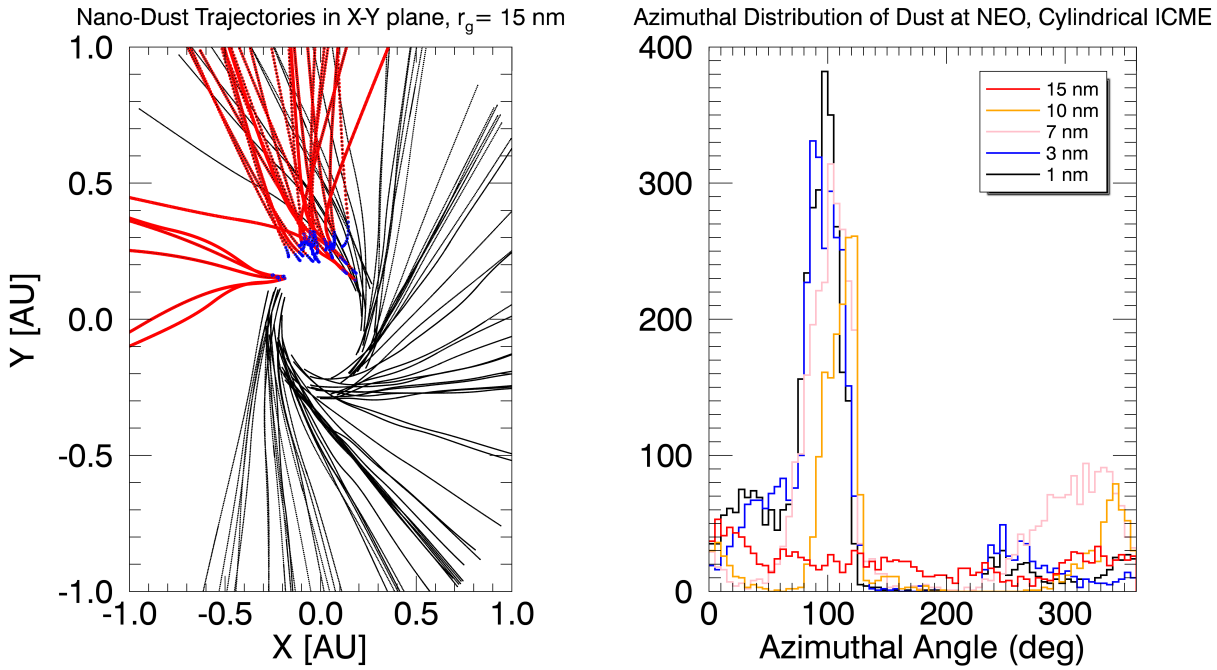

Figure 3.15 (Left) Trajectories of 15 nm particles that quickly escape the ICME due to their large Larmor-radii (e.g., initial Larmor radius of 0.05 AU compared to the ICME radius of 0.04 AU). (Right) azimuthal distribution at NEO comparing various nano-dust sizes. The effect is reduced for larger particles and is changed most drastically for the 15 nm particles that quickly escape the flux rope.

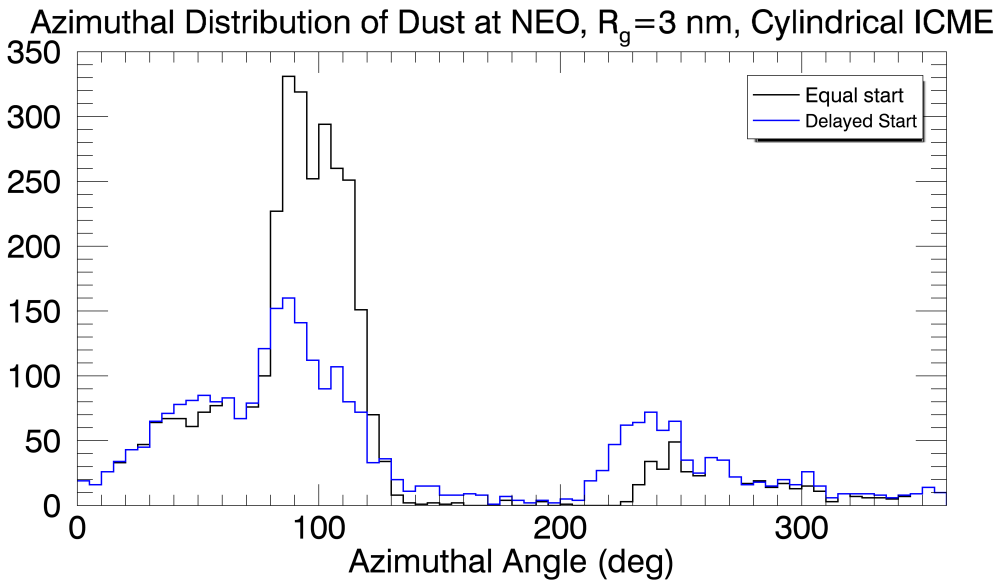

Figure 3.16 The azimuthal distribution at NEO for an equal start time of nano-dust and ICME compared to a run where the ICME was initiated 0.5 days after the nano-dust. The enhanced distribution is smaller and shifted in azimuth because the nano-dust trajectories are shaped by the solar wind prior to being picked up by the ICME. Note: large nano-dust might avoid interaction with the ICME if they have already drifted significantly out of the ecliptic plane prior to the ICME launch.

Detection of the enhanced fluxes at NEO shown in the above examples would correspond to the front of an ICME propagating along the Sun-spacecraft line in the ecliptic plane, as depicted in Figure 3.17 (right). If the spacecraft also measures the magnetic field profile of this ICME, the measured magnetic clock angle θ would change from -90°–90° and the cone angle would correspond to 90°, indicating the ICME axis lies in the ecliptic plane. The ICME events during which it is reported that STEREO measured an increased flux in nano-dust, correspond to similar magnetic field profiles (Fig. 3.17). While the STEREO observations (see Sec. 2.4.2) cannot be confirmed as events due to nano-dust impacts, this is an interesting correlation that could possibly support the hypothesis that STEREO detected nano-dust–ICME interaction. To

show the effect of ICME orientation on the pickup and delivery of a large concentration of nano-dust to NEO, two other ICME orientations are implemented in the model (Fig. 3.18).

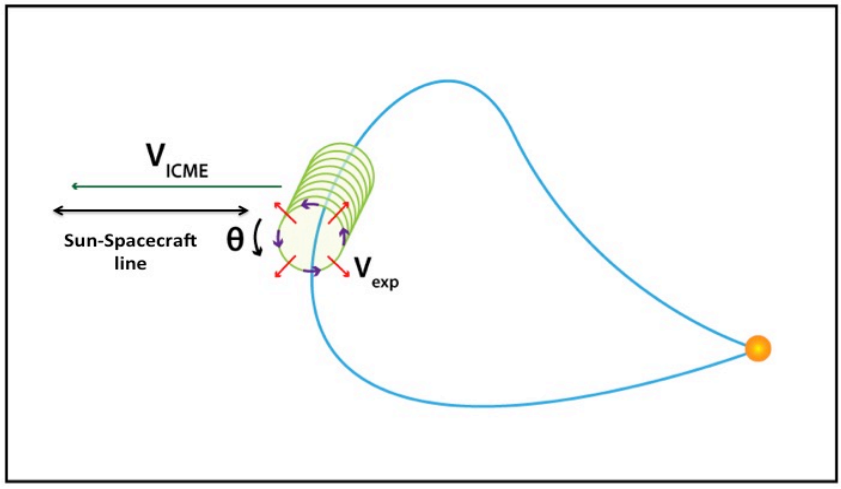

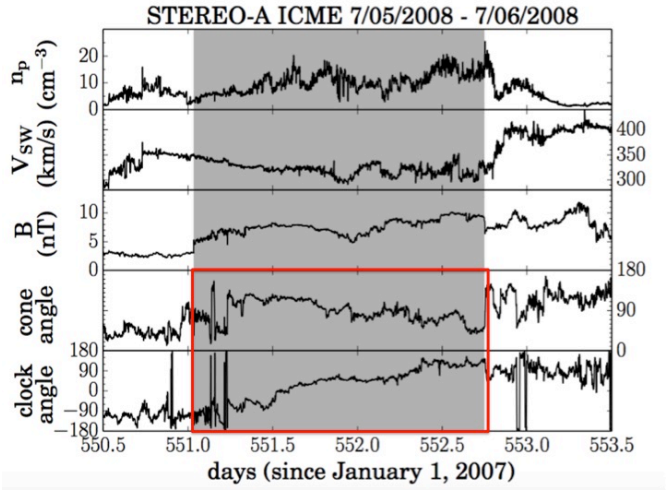

Figure 3.17 (Top) Depiction of the front of an ICME (approximated as a radially-expanding cylindrical flux rope) propagating along a hypothetical Sun-Spacecraft line in the ecliptic plane. *θ* denotes the clock angle of the azimuthal magnetic field, where a spacecraft passing through the flux rope would measure *θ* = -90°-90°. (Bottom) The ICME magnetic profile measured by STEREO during the reported increase in nano-dust fluxes corresponds to similar magnetic field characteristics, i.e., a similar clock angle profile and a constant cone angle at ~90°, which should correspond to an ICME propagating in the ecliptic plane (STEREO magnetic field data from *Le Chat et al.*, 2015).

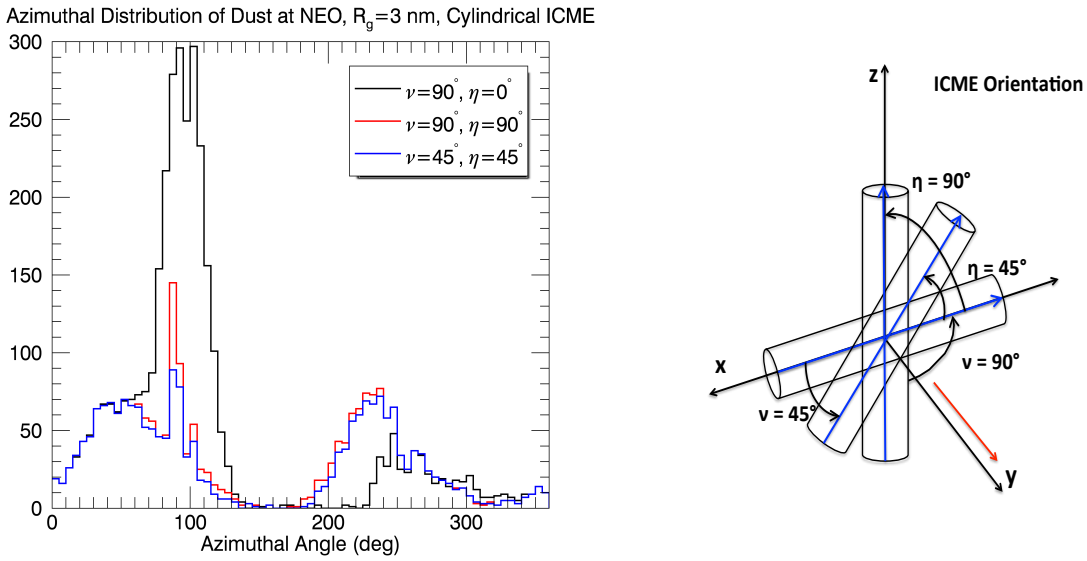

Figure 3.18 (Left) Comparison of the azimuthal distribution of 3 nm particles in the NEO region for different ICME axis orientations (right). The delivery of a concentrated nano-dust flux to NEO is not as pronounced. The reduced effect in the η = 90° case is due to the ICME encountering fewer dust particles. In the η = 45°, ν = 45° ICME, the axis is not oriented perpendicular to the propagation direction and the nano-dust delivery is not as strong.

The delivery of nano-dust to 1 AU and their azimuthal distribution at NEO varies with ICME propagation speed. The relative velocity of the ICME is a function of both the bulk velocity and radial expansion velocity. So, a change in the bulk velocity will result in a change of the convective electric field $\vec{E}_{EM}$, altering the nano-dust acceleration and drift motion. Figure 3.19 shows the azimuthal distribution at NEO corresponding to ICMEs with bulk speeds 400, 800, and 1000 km s^{-1}. The enhanced flux is reduced for both the 800 km s^{-1} and 1000 km s^{-1} cases where more nano-dust particles are transported out of the NEO region.

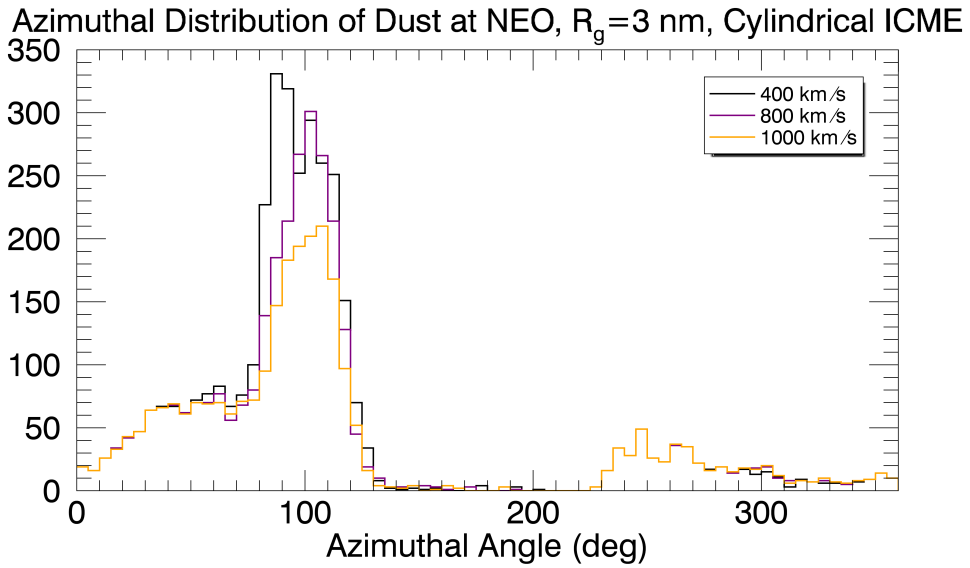

Fig. 3.19. Azimuthal distribution of 3 nm dust particles at NEO for ICMEs with bulk velocities of 400, 800, and 1000 km s^{-1}. The delivery of a concentrated flux to the NEO region is reduced for ICMEs with higher propagation speeds.

As discussed in Sec. 3.4, nano-dust born inside of ~0.15 AU become trapped in complex orbits around the Sun through their interaction with the solar wind. *Czechowski and Mann* [2010] suggested that the extent of this trapping region might change due to the effect of transient events, which could accelerate nano-dust that would otherwise remain trapped close to the Sun. An ICME can pick up particles born within this region and deliver them to 1 AU (Fig. 3.20). Thus, the nano-dust flux at 1 AU could include an even larger fraction of the near-Sun nano-dust distribution.

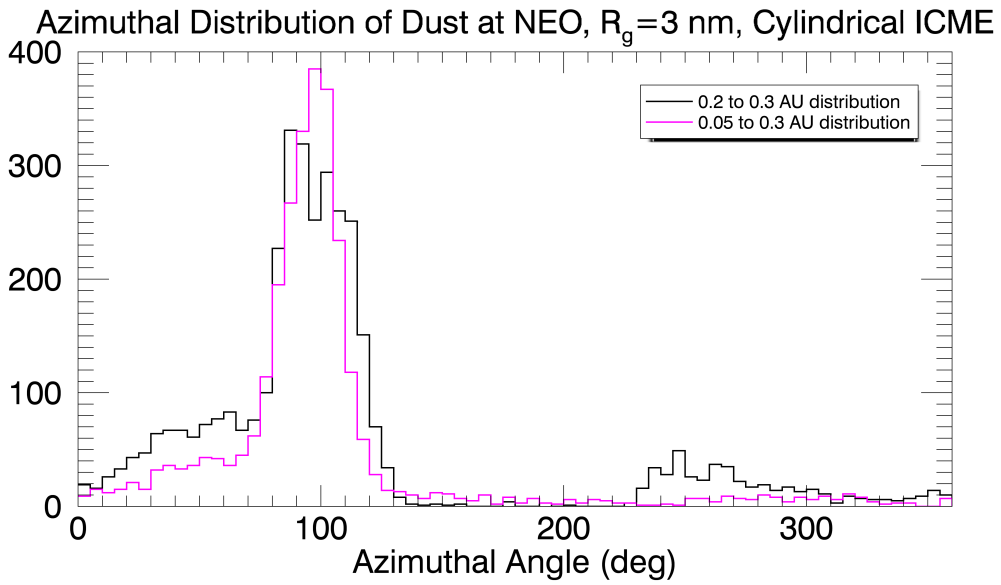

Figure 3.20 The azimuthal distribution of 3 nm particles at NEO is enhanced when the nano-dust distribution close to the Sun (< 0.2 AU) is included in the model. In this case, the particles are initially distributed in the circumsolar disk spanning orbits between $0.05 < r < 0.3$ and the ICME is launched with its axis centered at 0.1 AU. In the non-ICME model, the distribution within ~0.2 AU are not transported to 1 AU by the solar wind but are in trapped orbits around the Sun. The distribution here shows that an ICME can pick up and transport nano-dust born at < 0.2 AU to 1 AU.

3.7.5. Nano-Dust interaction with an ICME with Toroidal Geometry

The cylindrical flux rope model can describe the local geometry of an ICME, but the global structure is curved along the axis (see Fig. 3.9). One way to approximate/model this curvature and analyze the effects on nano-dust delivery to NEO is to use a generalization of the *Lundquist* [1950] cylindrical solution adapted to a toroidal geometry. The adapted solution is described below [*Romashets and Vandas*, 2003, *Miller and Turner,* 1981].

$$
\begin{aligned}
B_r &= B_0 \frac{R_0 - 2r\cos\theta}{2\alpha R_0 (R_0 + r\cos\theta)} J_0(\alpha r)\sin\theta \\
B_\phi &= B_0 \left(1 - \frac{r}{2R_0}\cos\theta\right) J_0(\alpha r) \\
B_\theta &= -\frac{B_0}{2\alpha R_0 (R_0 + r\cos\theta)} \{2\alpha R_0^2 J_1(\alpha r) \\
&\quad -R_0[J_0(\alpha r) - \alpha r J_1(\alpha r)]\cos\theta \\
&\quad +r[2J_0(\alpha r) - \alpha r J_1(\alpha r)]\cos^2\theta\}
\end{aligned}
\tag{3.7}
$$

where R_0 describes the major radius of the torus and $r = r_0$ describes the minor radius. The geometry is shown in Fig. 3.21. The aspect ratio of the torus is defined as R_0 / r_0. The equations used to describe the torus are approximately force-free solutions only for large aspect ratios ($R_0 / r_0 >> 1$). In the model used here, a flux rope of toroidal shape is added to the model. So that the torus doesn't completely encircle the Sun, a half-torus is used (similar to Fig. 3.21). Analogous to the cylindrical case, its axis is centered in the ecliptic plane at 0.2 AU and propagates in the $+y$ direction (HAE coordinate frame) at a constant speed of 400 km s^{-1}. The minor radius of the torus r_0 expands in the same way the cylindrical flux rope expands. The aspect ratio remains constant throughout the torus propagation: R_0 increases proportional to r_0. The toroid geometry used corresponds to an aspect ratio of $R_0 / r_0 = 3$. Even if the force-free condition is not met, the approximation is adequate to simulate the effect of a curved flux rope geometry on nano-dust trajectories.

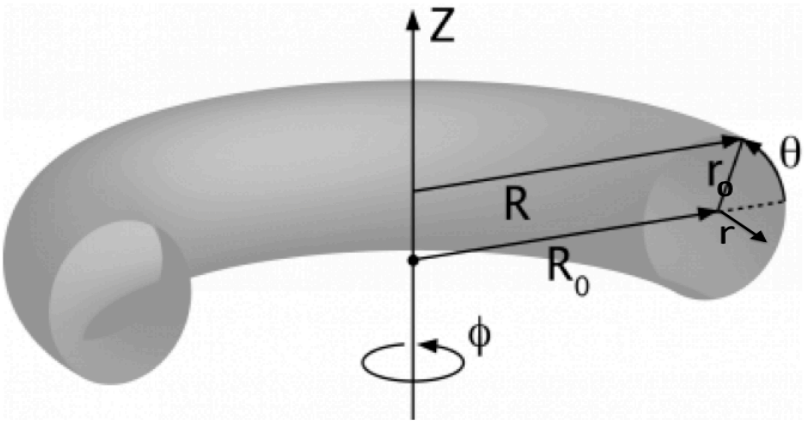

Figure 3.21 Geometry of a torus depicting the major radius R_0, and radial position from the torus axis r. The radial boundary of the torus is described by $r = r_0$.

The particles are picked up by the toroidal ICME and propagate along with it. The additional axial curvature introduces an additional drift component $u_{cg}\hat{z}$, which provides another opportunity for the nano-dust to escape from the flux rope. Figure 3.22 shows the azimuthal distribution of nano-dust at NEO for a 3 nm particle. The concentrated flux at NEO along the line of ICME propagation is reduced, but still present for the toroidal structure.

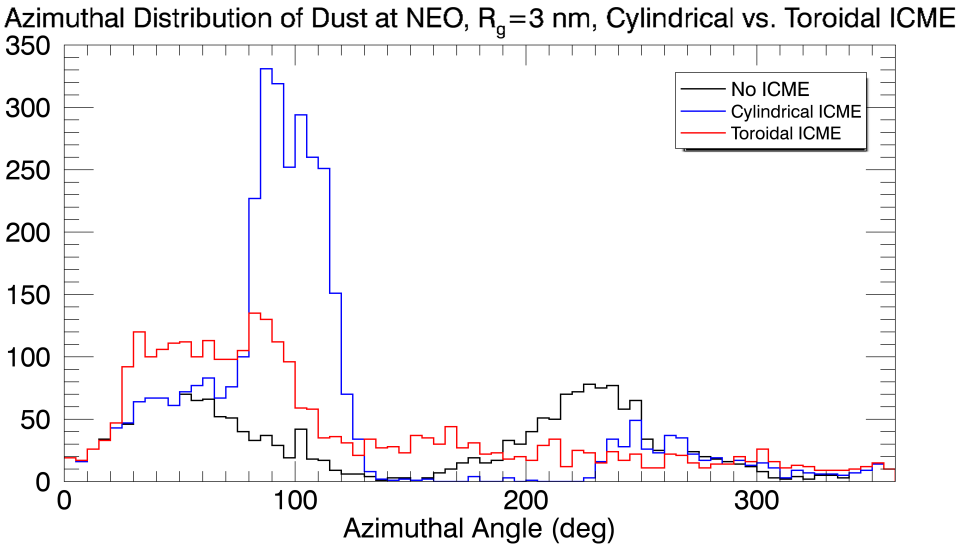

Figure 3.22 Azimuthal distribution of 3 nm particles at NEO for the toroidal ICME. The enhancement in the distribution along the direction of ICME propagation is similar to that of the cylindrical ICME case, but smaller. Note that the enhancement is broadened about the 90° azimuthal angle corresponding to the ICME propagation direction. This is a result of the spread in direction of nano-dust trajectories and also represents the nano-dust particles that have escaped the ICME.

3.7.6. Discussion

The investigation of nano-dust–ICME interaction presented in this section suggests that it is possible for small nano-dust (< ~10 nm) to become picked up by an ICME and transported to NEO in a concentrated form. There is additional potential enhancement of dust fluxes at NEO from particles born at < 0.2 AU, which would otherwise be trapped near the Sun. On the other hand, this interaction would translate to an ICME transporting small nano-dust away from the NEO region in the case of an ICME propagating far from the ecliptic plane. Thus, an ICME can greatly disturb the nano-dust trajectories and can clear out a small portion of the near-Sun dust environment. A spacecraft equipped with a well-calibrated dedicated dust instrument operating near 1 AU should be able to measure enhanced nano-dust fluxes delivered by ICMEs, provided

that it propagates along the Sun-spacecraft line. In the investigation reported here, it was shown that a cylindrical flux rope with its axis lying in the ecliptic plane, perpendicular to its propagation direction, which can approximate the local geometry of an ICME, will deliver a concentrated flux of nano-dust particles to NEO. A toroidal-shaped ICME incorporates the global curvature of an ICME into the model and shows that nano-dust trajectories are more scattered in direction and more particles also escape the ICME.

For the ICME model described in this chapter, the distribution in arrival directions indicates that these particles are detectable by NDA, with an azimuth that spans a range of -20°–20° with the peak at 0° and a zenith spanning -40°–40° also with a peak at 0° (see Fig. 3.8 for comparison). The larger nano-dust (> 10 nm) quickly escape the ICME, resulting in a wide range in both the azimuth (-20°–20°) and zenith (-40°–40°). Only a fraction of the particles delivered to NEO by the ICME would be detected and, at this time, it cannot be confirmed that the measurements would identify a nano-dust–ICME interaction. However, simultaneous measurements of ICME properties could allow for correlation between the two measurements. It is also important to note that the structure and evolution of ICMEs propagating through the inner Solar System is more complex than the model used in this investigation. For example, an ICME likely deviates from a perfectly expanding cylinder. Through its interaction with the surrounding solar wind, the resulting structure will be more oblate. Depending on the relative ICME and solar wind velocity, the non-isotropic dynamic pressure of the solar wind can deform the ICME considerably and tend to elongate or flatten out the flux rope, especially for ICMEs with velocities much greater than the solar wind [*Riley et al.,* 2004; *Owens and Cargill,* 2006]. These deviations from a cylindrically symmetric flux rope could change the reported results, but it is expected that the alteration of nano-dust trajectories will still be significant.

3.8. Summary of Nano-Dust Dynamics Investigation

Modeling nano-dust dynamics through their interaction with the solar wind is important to understand the complex interaction of matter in the inner Solar System and its effect on dust transport and evolution. This interaction describes a picture of nano-dust becoming entrained in the solar wind, propagating outward in the Solar System with varying distribution in latitude and longitude, as well as speed and directionality, all a function of dust size, initial conditions of the dust distribution, and solar wind/HCS structure and dynamics. Importantly, the detailed investigation indicates that the nano-dust is delivered to NEO, where they can be detected and analyzed by dedicated instruments. Transient events like ICMEs have their own unique interaction with nano-dust particles and the nature of these interactions can be explored. The modeling is also particularly helpful in constraining the expected flux variability, velocity and angular distribution of nano-dust at 1 AU where a dust instrument like NDA could potentially detect them. Signatures in the measured fluxes such as flux variability and directionality report on the nature of the dust-solar wind interaction processes and can be interpreted by dynamical modeling.

Chapter 4. The Nano Dust Analyzer: a Linear TOF Mass Spectrometer to Detect and Measure the Chemical Composition of Nano-Dust

4.1. Introduction and Motivation

The content in this chapter describing the development of the Nano Dust Analyzer is based on the work presented in *O'Brien et al.* [2014]. Nano-dust and β-meteoroids are ejected from the inner Solar System where a fraction of them can be detected at Earth's orbit. This provides a unique opportunity to learn about processes in the inner Solar System even at 1 AU. The reported detection of nano-dust originating in the inner Solar System by STEREO, as discussed in Sec. 2.4.2, was the main motivation for developing a dedicated dust instrument that can measure the nano-dust and β-meteoroid flux, reveal information about their mass and/or velocity distributions, and determine their elemental composition. These measurements can improve the understanding of the near-Sun dust distribution and its variability, point to the origin of nano-dust and β-meteoroids, and investigate the complex interaction of nano-dust with the solar wind (see Ch. 2).

This chapter presents the concept and development of the Nano Dust Analyzer (NDA) instrument designed for detection and elemental analysis of nano-dust particles originating in the inner heliosphere. NDA is a uniquely designed instrument: while derived from previously-flown dust detectors, it must operate while pointed close to the Sun's direction (see discussion in Sec. 3.6.3), which presents significant challenges for a dust instrument for three primary reasons: (1) heat load from the solar radiation and related temperature variations, (2) exposure to solar wind electrons and ions, and (3) operation under solar UV illumination. A preliminary thermal analysis showed that the NDA design is suitable for operation in the expected temperature range

[*O'Brien et al.,* 2014], (2) will be discussed in Sec. 4.9.2, and (3) is addressed in Chapter 5. In addition to close Sun-pointing operation, NDA must have a sufficiently large target area to detect statistically significant dust fluxes and must achieve a mass resolution of $m / \Delta m > 40$ to identify elemental constituents, which will be discussed in more detail in following sections. Furthermore, the expected dust velocities and distribution in the dust arrival directions, shown in Figures 3.7 and 3.8, are used to guide the instrument operation requirements such that NDA can measure the full range of nano-dust and β-meteoroids. These results reveal that the optimal operation of the NDA is from a spacecraft that spins about the Sun-spacecraft line.

The NDA instrument deployed on a future heliospheric mission operating outside of Earth's magnetosphere could directly address the following key science goals: (1) Confirm the existence of nano-dust fluxes, as inferred by the STEREO observations. (2) Reveal the dynamics of the nano-dust particles by correlating the observed particle fluxes (and their variability) with the parameters of the solar wind plasma and interplanetary magnetic field. (3) Determine the source of the nano-dust particles by measuring their size distribution and chemical composition. The instrument will also measure the fluxes and composition of β-meteoroids at 1 AU, addressing the long-standing uncertainties of their origin and constrain their fluxes. This chapter describes the concept and design of the NDA, which is an instrument design suitable for development for a future space mission. A laboratory prototype was built and tested, and all details involving the prototype version are discussed in Sec. 4.8.

4.2. Instrument Concept

4.2.1. Principle of Operation

The NDA is a linear time-of-flight (TOF) mass spectrometer designed specifically to detect nano-dust delivered from the inner Solar System to 1 AU. The instrument is derived from previously-flown dust detectors and is most similar to the Cosmic Dust Analyzer (CDA) on the Cassini spacecraft [*Srama et al.,* 2004]. Figure 4.1 shows the NDA design and the principle of operation. A dust particle entering the instrument from the top passes through a set of grid electrodes (biased to keep out solar wind particles) and then impacts a curved metallic target. The high-speed impact generates a cloud of ions, electrons, and neutral particles, which are released from both the dust and target material. The positive and negative charges are separated by an electric field applied between the target held at a positive potential, and a grounded grid in front of it. The positive ions are accelerated toward the grid and the electrons and negative ions are recollected by the target. The positive ions pass through the grounded grid, entering a field-free drift region where they arrive at a detector in sequence according to their mass, producing a TOF mass spectrum. The instrument measures three signals: (1) the impact charge signal: the negative charge recollected by the target is measured by an AC-coupled charge sensitive amplifier (CSA). The impact charge measurement provides information about the mass and velocity of the impacting particle (see Sec. 4.4). (2) The ion grid signal: a fraction of the positive ions are collected on a 58% open area grid in front of the ion detector and the collected charge is also measured by a CSA. The remaining ions pass through the grid to reach the detector. The ratio of the charge collected by the detector to the impact charge measured at the target allows the detector ion collection efficiency to be determined. Knowledge of the charge collected by the

detector also allows the ion detector performance to be monitored. (3) The ion detector TOF signal, which provides the mass spectrum.

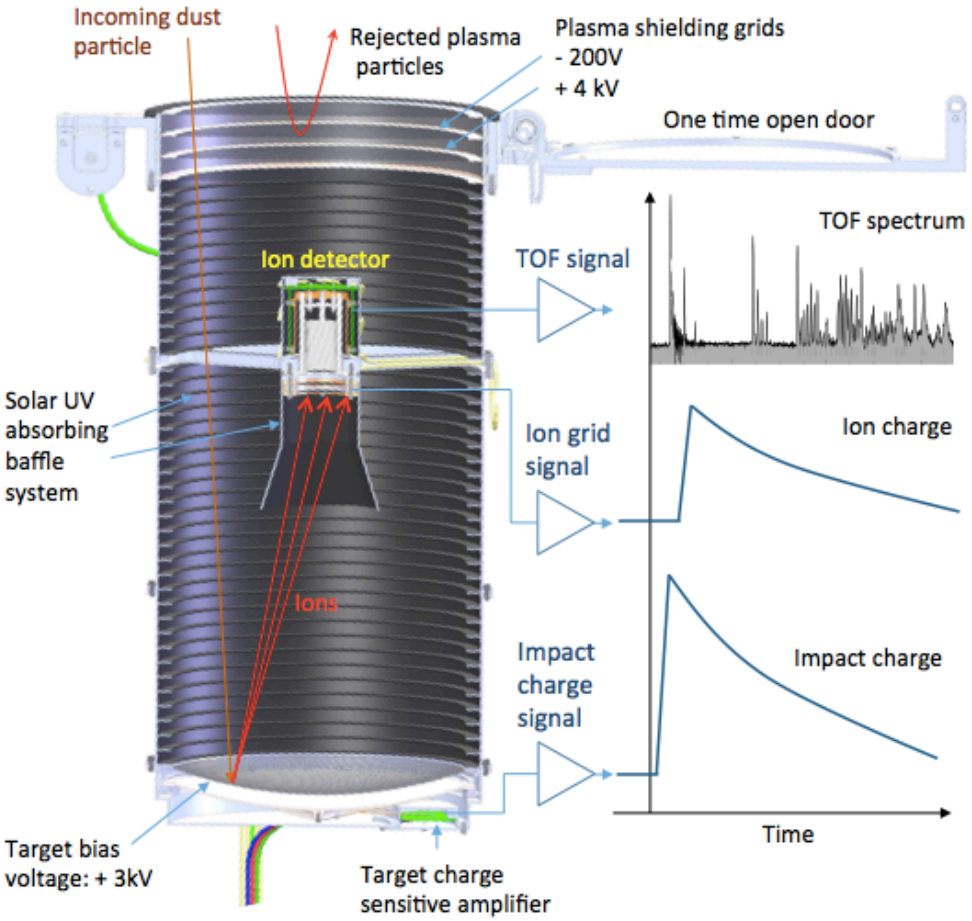

Figure 4.1. Schematic of the NDA instrument. The main subsystems are the SW rejection grid system on the top, the curved impact target on the bottom, and the ion detector system in the middle. The instrument housing is lined with an optical baffle system to reduce the fraction of solar UV photons scattering into the detector. A one-time open door is also shown that would keep the instrument from contamination prior to launch. The instrument measures three electric signals that are discussed in the text with more detail.

4.2.2. Instrument Design and Main Subsystems

The main instrument subsystems include the entrance grids, the impact target, the ion detector, and the optical light trap (other subsystems including the high and low-voltage power

supplies, data acquisition system, etc. are not unique to this instrument and will not be discussed in detail). The 22 cm diameter instrument body houses the main subsystems. NDA achieves a 40° full width cone field-of-view (FOV) and is designed for a fixed 25° pointing direction from the Sun-spacecraft line, about which the spacecraft is spins, allowing the finite FOV to cover the wide range of dust arrival directions at 1 AU (Sec. 3.6.3). The FOV and pointing requirements are driven by the expected directions of dust flux and the effect of solar UV radiation on the instrument's performance (see Sec. 3.6.3 and 5.6).

The entrance grid subsystem will reduce the number of solar wind particles entering the instrument that could scatter into the detector and interfere with the dust measurements. The system consists of four identical molybdenum grids with 92% open area, spaced 10 mm apart. The innermost and outermost grids are connected to chassis ground and the two grids in the middle are biased at -200 V and +4 kV to reject solar wind electrons and ions but allow charged dust particles to enter. Details of the effectiveness of the grid system are described in Sec. 4.7.2.

The impact target is a curved super-polished (< 5 nm *rms* surface roughness) titanium substrate with a 2 μm coating of Rhodium. Rh is the target material of choice because it is chemically inert, has a high impact charge yield, and at a mass of 103 *u* will not interfere with the expected mass lines (see Sec. 4.5.4). Rh as the target material has heritage in other dust impact detectors, including CDA [*Srama et al.,* 2004] and LDEX on the LADEE lunar mission [*Horanyi et al.,* 2015]. The impact target is biased at +3 kV and a high open area grid (concentric with the target) is placed 1 cm in front of it. This grid is connected to chassis ground, providing the acceleration region for the positive ions to be extracted. The target is 20 cm in diameter and has a ~100 cm^2 effective collecting area, when the shielding of the grids in the front and in the ion detector housing are considered. This target area is sufficient for making statistically

significant nano-dust measurements. Nano-dust flux estimates at 1 AU are derived from the STEREO measurements interpreted as impacts of nano-dust on the spacecraft. *Meyer-Vernet et al.* [2009] analyzed the data and reported a cumulative flux of F = 0.03 to 5 m^{-2} s^{-1}. These fluxes correspond to ~6–1000 impacts per day onto the NDA target when the expected nano-dust distribution/directional scan are factored in. Based on the Pioneer 8 and 9 measurements of β-meteoroids, which report a flux of ~ 10^{-4} m^{-2} s^{-1}, only 0.03 impacts per day (12 per year) on NDA are estimated [*Berg and Grün,* 1973].

The ion detector subsystem includes the Hamamatsu R2362 electron multiplier, which has a 3 cm^2 active area. The detector is located at the radial center of the target's curvature in a cylindrical housing that is mounted to the instrument walls on a tripod. The selected detector achieves the required sensitivity and dynamic range to measure the expected nano-dust and β-meteoroid distributions, which will be discussed in detail in Sec. 4.7. There are two grids in front of the detector. The outer one is the ion grid that is connected to a CSA. In between the ion grid and the detector is a grounded, high open-area grid, which acts as a Faraday shield, allowing low-noise measurements. The ion grid CSA and the detector front-end electronics are co-located within the detector housing.

The optical baffle subsystem reduces the fraction of incident solar UV photons scattering into the detector and interfering with the TOF ion signals. It is composed of two main components: (1) a set of baffles coated in low-reflectivity material, lining the inner walls of the instrument housing and (2) a conical extension to the detector housing, with the same coating. The baffle system is designed such that UV photons from the Sun can reach the detector only after multiple scattering events from these low-reflectance coated surfaces. Chapter 5 describes the detailed analysis that led to the design of the optical baffle subsystem.

4.3. NDA Testing and Calibration Facility

Before proceeding to discuss the details of the instrument functionality and design, the facility that will be used for testing and calibration of the NDA is discussed to provide background on the current laboratory test and measurement capabilities, which will be useful in following sections. The calibration and testing of the NDA includes functionality verification, performance characterization, and laboratory analogues that aid in the interpretation of TOF mass spectrum data. The NDA can be calibrated using high-speed dust particles with known composition, mass, and velocity. This type of testing is performed using a dust accelerator such as that operated at the University of Colorado. The operation principle and capabilities of the accelerator can be found in *Shu et al.* [2013]; here only a brief description is given. The facility is a 3 MV electrostatic generator (Fig. 4.2) that is capable of accelerating micron and submicron-sized dust particles to high velocities. Dust particles are charged and then transported into a homogeneous accelerating field before traveling down a beam line to a vacuum chamber where they impact on the instrument's target. Before reaching the target, the particles are characterized in terms of their mass m and velocity v by image charge measuring sensors. The velocity is determined by the time difference between two separate sensors spatially separated by a known distance along the beam line. The mass is derived from the conservation of energy equation $m = 2QU_{accel}/v^2$ where U_{accel} is the accelerator terminal potential, and Q is the measured dust charge. The particle selection unit is a subsystem of the facility that allows user-defined mass and velocity ranges to be set for the particles that are allowed to enter the experimental chamber.

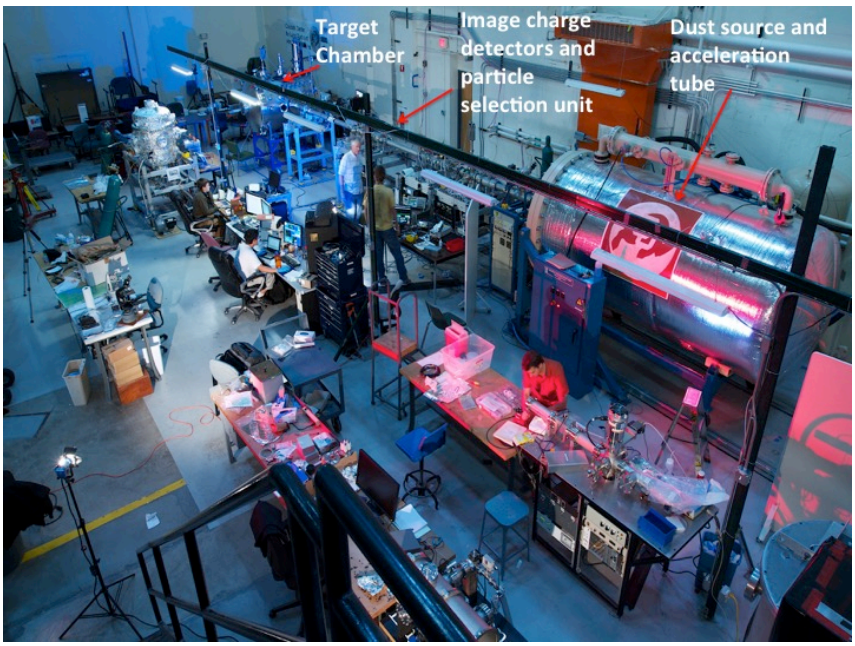

Figure 4.2 Picture of the dust accelerator at the University of Colorado.

Figure 4.3 shows the accelerator capabilities in terms of dust particle mass/size and velocity distribution. Particles between ~ 30 nm to 2.5 μm are accelerated to velocities typically between ~ 1–60 km s^{-1}. Generally, smaller particles can reach higher velocities as mass is proportional to r_g^3, while charge, assuming a constant surface potential, is proportional to r. The attainable velocity is constrained by two factors: (1) the ion field emission that limits the charge on the dust particles and (2) the noise floor of the electronics used for the detection of the smallest dust charges. Dust particles that can be used in the accelerator are either of a conductive material or coated in a conductive material. Iron particles are commonly used due to their stable and good performance. Recently, coating methods have been developed that can be applied to mineralogical samples to make relevant dust samples usable in the accelerator (see, for example, *Hillier et al.,* 2009).

The current capability of the dust accelerator is close to 100 km s^{-1} velocity, nevertheless, this is still considerably smaller than velocities that nano-dust can reach near 1 AU of ~300 km s^{-1} (see Fig. 3.7). This means that there is no facility that would allow testing and calibration of the NDA over the entire mass/velocity ranges of interest. The following sections describe how the scaling laws are used to define the expected operational parameters of the NDA and that ample margin is built in for uncertainty.

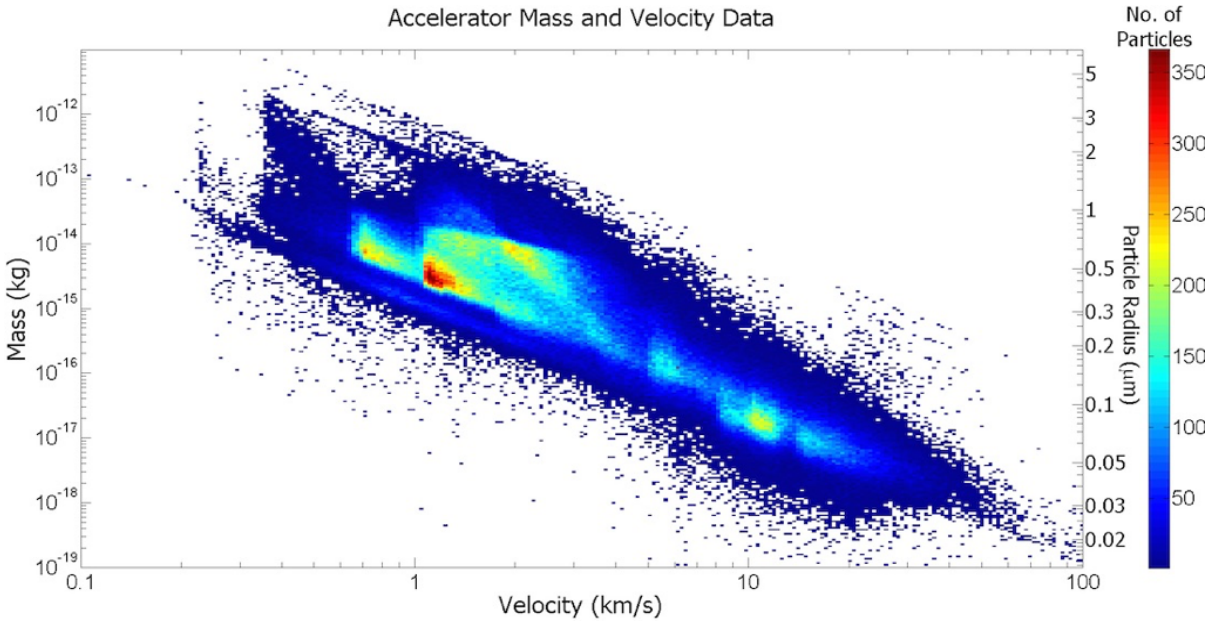

Figure 4.3 Distribution of dust velocity and mass/size range covered by the dust accelerator at the University of Colorado.

4.4. Impact Ionization Process

This section will provide a more detailed discussion of the impact ionization process that is utilized by NDA to detect and analyze cosmic dust particles. When a high-velocity dust

particle impacts a solid surface, a cloud of ejecta including neutrals, ions, and electrons is released from both the dust particle and target material. Upon impact, a shock wave is generated through the dust particle and target, causing compression and heating. Depending on the dust mass and impact velocity, the particle is partially or completely vaporized. For lower-speed impacts ($5 < v < 10$ km s^{-1}), ionization of the particle is incomplete and a significant part of the ion species originates from the surfaces of the dust and target material and is often dominated by impurities with low ionization potential [*Drapatz and Michel,* 1974]. At higher speeds, temperatures are high enough to dissociate the molecules and ionize the atoms composing the particle, thus volume ionization becomes more prominent. For particles with speed ≥ 50 km s^{-1}, the particle is expected to be ionized throughout its entire volume. From the impact, the cloud of vaporized/ionized material expands adiabatically into vacuum [*Hornung and Drapatz*, 1979]. Ions are also generated from the target, including the target material as well as impurities and contaminants on the target surface.

Thus, the composition of ions generated by low-velocity dust impacts tends to have a relatively higher content of low-ionization potential components, such as the Na and K alkali metals, which are commonly present as impurities. Lower-velocity impacts also generate more molecular and cluster ions [*Knabe and Krueger*, 1982], which are either characteristic of the material or can form in the expanding plasma cloud. High-velocity impacts, on the other hand, will exhibit a larger contribution from atomic ions of the target/dust bulk material [*Kempf et al.,* 2005a; *Mocker et al.,* 2013]. Experimental studies have shown that the kinetic energy of the ions generated by the impact has little variation with impact velocity and is typically around 20-40 eV per ion. However, impurity ions show different behavior due to their different formation processes [*Ratcliff et al.,* 1997]. The initial energy distribution of the ions is an important concept

in TOF mass spectrometry since it affects the widths of the mass lines, which will be discussed more in Sec. 4.4. The impact ionization process is complex and still not fully understood. Both impact charge/TOF spectrum measurements and impact ionization models explore the impact process to improve understanding, but this is outside of the scope of this thesis and will not be discussed further.

Dust detection through impact ionization is the most sensitive method, and provides the best option for measuring nano-dust particles [*Auer,* 2001]. The total charge generated upon a dust impact reveals information about the mass and speed of the dust particle. The impact charge yield is typically measured by a CSA attached to the target. If the target is biased positively, the positive ions will be accelerated away and the electrons and negative ions will be recollected by the target, and vice versa. The positive and negative charges generated are equal, so the measurement of the charge recollected by the target represents the total charge generated in an impact. Impact charge measurements have been performed over a wide range of dust masses and velocities (50 m s^{-1}–90 km s^{-1}) and also for a number of dust-target material pairs. These measurements reveal that the impact charge generated is related to the mass and velocity of the dust particle by a power law of the form:

$$Q = \left|Q^-\right| = Q^+ = Km^{\alpha}v^{\beta} \tag{4.1}$$

where K, α, and β are fitting parameters that are experimentally determined for a given target material. The impact charge typically varies linearly with $m \sim \alpha = 1$, and v (km s^{-1}) to the power of $3.5 \leq \beta \leq 5.6$, depending on the target material, and K = ~0.5 is also a function of the target material [*Auer*, 2001; *Collette et al.,* 2014]. For dense and high tensile strength target materials,

the limited available information indicates that the impact charge depends mostly on the mass of the impactor, rather than its material. The rise time of the impact charge signal is also a function of the dust velocity and is shorter for high-speed impacts [*Auer*, 2001]. The relationship between signal rise time and impact velocity is derived purely from experiments and is useful in estimating the dust velocity if there are calibration measurements to compare to.

The impact charge dependence on the target material is one of the important factors for the selection of the appropriate target. Due to the small mass of the nano-dust particles of interest it is important that a target with a high impact charge yield be selected. Figure 4.4 shows plots of the impact charge yield per unit mass for different target materials (based on the experimentally-derived power laws). The curves are extrapolated to higher velocities to include nano-dust. The second important factor in selecting the impact target material is simple chemical composition and cleanliness. Pure precious metals with high atomic number are an obvious choice. (The high atomic number ensures that there is no interference between the TOF mass lines from the dust particle and the target material.) Rhodium has been used successfully as a target material in the CDA instrument [*Srama et al.,* 2004] and there is no reason to deviate from this choice for NDA.

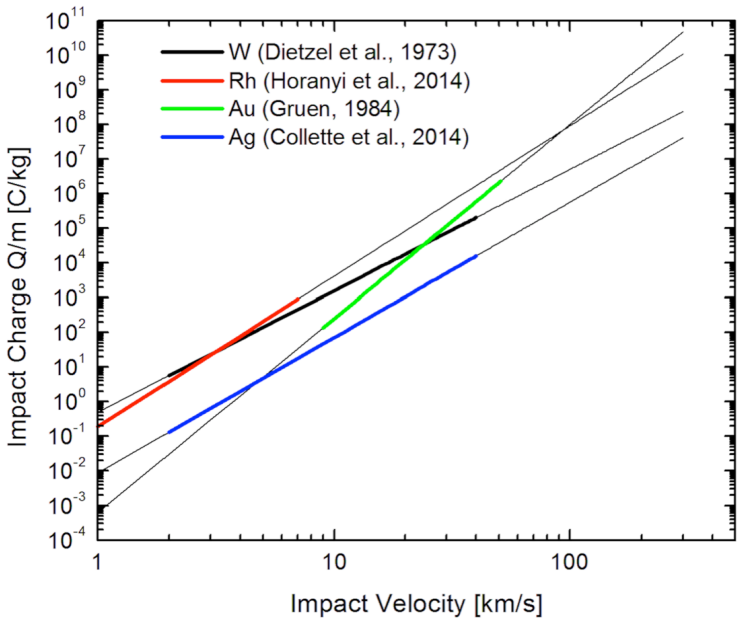

Figure 4.4 The variation of the impact charge Q, normalized to the mass m of the particle, as a function of impact velocity for target materials W, Rh, Au and Ag with Fe projectiles. The colored part of each curve indicates the velocity range over which the calibration measurements were performed. The data are then extrapolated over 1–300 km/s (from *O'Brien et al.*, 2015).

4.5. Time-of-Flight Mass Spectrometry

An impact ionization-based TOF mass spectrometer provides (1) sensitive detection of dust impact events, (2) impact charge measurements yielding information about the mass and velocity of the impacting dust particle and (3) a mass spectrum revealing the dust elemental composition. For the impact velocities of nano-dust particles, the measured mass spectrum will be entirely composed of atomic ions, revealing the elemental composition of the dust particle.

4.5.1. Linear TOF Mass Spectrometer Concept

The NDA belongs to the linear TOF mass spectrometer class, which is described in this section. Within the spectrometer, the ions generated by the dust impact on the target are accelerated by the potential difference U_{acc} applied between the target and a grounded grid. The

polarity of the applied potential determines whether positive or negative ions are accelerated toward the detector. The accelerated ions of a given species, labeled by the subscript *i*, have energy $Q_i U_{acc} = 1/2(m_i v_i^2)$ where Q_i, m_i, and v_i are the ion charge, mass, and velocity. After passing through the grounded acceleration grid, the ions travel through a field-free region to the ion detector where they are registered sequentially according to their mass.

$$t_{TOF}(m_i) = t_0 + a\sqrt{m_i} \tag{4.2}$$

Equation 4.2 relates the ion mass to the ion flight time recorded by the detector. t_0 is the shift parameter, which accounts for any offset between the trigger for recording the signal and the actual start of the spectrum. a is the stretch parameter dependent on the instrument parameters, including U_{acc} and the distance of the ion flight path to the detector. The initial energy and angular distributions of the impact-generated ions cause a spread in their arrival times and, thus, a broadening of the recorded mass peaks. This broadening limits the mass resolution as it presents a challenge in distinguishing mass lines in close proximity, which may overlap.

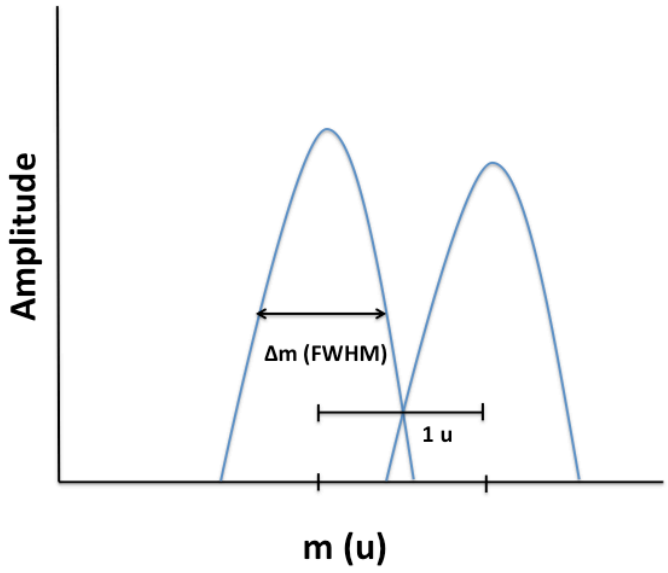

Figure 4.5 Simple example of two adjacent mass lines. The width is *Δm* measured at 50% of the amplitude of the mass peak as shown.

The standard way to characterize the spectrometer's performance and ability to resolve mass lines in the spectrum is by its mass resolution, $m/\Delta m$, where m is the mass of the line-forming ion and Δm is the full width of the mass peak at half maximum, FWHM (Fig. 4.5). The mass resolution is related to the time resolution of the TOF signal through the relationship $m/\Delta m = 1/2(t/\Delta t)$. A large mass resolution is desired to separate ion species that are close in mass for a wide range of masses, and the resolution required by an instrument is dependent on the ion species that need to be resolved. One important thing to note is that Δm is dependent on the ions' initial energies and angular spread. The initial energy spread, and consequently the mass resolution, may be different for ions that are generated by different processes, e.g., volume vs. surface ionization. Distinguishing between adjacent mass lines is especially difficult when a

small amplitude peak is next to a larger one, this overlap can be significant since the small mass peak becomes immersed in the wider part of the large mass peak. One way to improve the mass resolution in a linear-type TOF spectrometer is the use of a higher accelerating potential U_{acc} that reduces the relative importance of the spread in initial ion energies [*Kempf et al.,* 2012; *Mocker et al.,* 2011].

4.5.2. Reflectron TOF Mass Spectrometer

A reflectron-type TOF mass spectrometer can achieve a higher mass resolution than the linear design. In the reflectron, the accelerated ions do not drift straight toward the detector. Instead, they enter a decelerating electric field where they will slow down and eventually be turned around (on a parabolic path) and focused onto the detector. Ions with higher speed (larger initial kinetic energies) will have a longer flight path, traveling deeper into the decelerating field, allowing time for the lower energy ions to catch up to them. Instruments of this kind include the Cometary and Interstellar Dust Analyzer (CIDA) on the Stardust mission [*Kissel et al.,* 2003]. Further, Large Area Mass Analyzers (LAMA) have been developed to employ high mass resolution, a large target area, and low mass [*Austen et al.,* 2002; *Rachev e al.,* 2004; *Srama et al.,* 2004; *Sternovsky et al.,* 2007]. Reflectron-type instruments, however, either do not possess adequate target areas or they have their detectors exposed towards the aperture and are not suitable for operation while pointing close to the Sun's direction. Furthermore, as discussed in Sec. 4.9.1, the NDA has sufficient mass resolution for the sensitive detection of all species expected to be present in nano-dust particles (see Sec. 4.5.4 and 4.9.1).

4.5.3. Cassini Cosmic Dust Analyzer (CDA)

The basic concept of NDA is derived from the Cassini Cosmic Dust Analyzer (CDA), [*Srama et al.,* 2004] the linear TOF mass spectrometer on the Cassini mission to Saturn. Thus, it

is important to discuss CDA's ability to successfully detect and measure the composition of dust particles near Saturn even with a moderate mass resolution. In particular, it is interesting to point out that CDA was sensitive enough to detect and analyze the composition of high-speed nanometer-sized dust particles from both the Jovian and Saturnian systems. Similar to NDA, CDA includes a curved Rhodium target, which is biased at +1 kV and focuses positive ions onto the centrally-located ion detector in a TOF fashion. The CDA achieves a mass resolution $m/\Delta m$ ~20–50.

The mass and speed of the nanometer-sized dust particles from the Saturnian system, known as the Saturnian stream particles, is determined through a combination of CDA measurements and dynamical calculations [*Horanyi,* 2000; *Kempf et al.,* 2005b; *Hsu et al.,* 2011]. The directionality and flux variability of the detected particles as well as the solar wind conditions and Saturnian magnetosphere are used to trace the dynamical properties of the stream particles. The stream particles are estimated to be $\leq$ 10 nm in size with speeds between 50–200 km s^{-1}. These sizes and speeds lie outside of the calibration range of accelerator facilities and could not be determined from CDA's impact charge signal. The impact charge generated by nanometer-sized dust particles is small, so often the TOF signals were weak in individual spectra, but the most common mass lines were identified by using a method of adding signals from spectra with similar strength and features [*Kempf et al.,* 2005a]. The mass spectra recorded by CDA indicate that the impact energies were high since the impact spectra show distinct mass lines corresponding to mostly atomic ions and consist of rocky elements such as Si and O, as well as Rh and H from the target and the alkali metals Na, and K, as shown in Fig. 4.6.

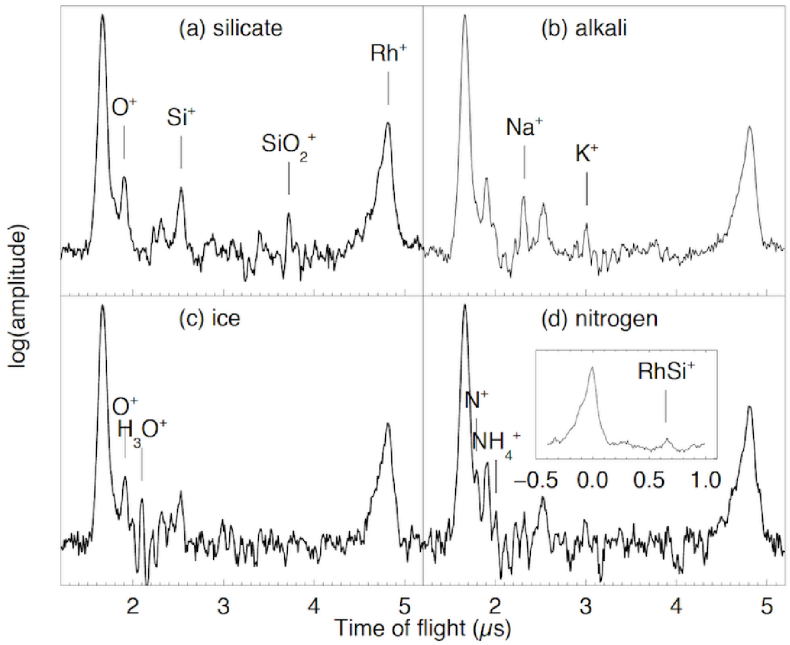

Figure 4.6 The time-of-flight mass spectra recorded by the CDA instrument on Cassini. The figure depicts the composition of nanometer-sized dust particles that are emerging from the inner Saturnian system. The spectra are grouped into four types. Note that features of the other types still exist in each spectrum (from *Kempf et. al.*, 2005a).

The analyzed spectra were identified to belong to four distinct composition groups (as shown in Fig. 4.6): a silicate group, an alkali group, a water ice group, and a nitrogen group. The spectral analysis indicates that most of the stream particles are composed of a silicate mineral with some showing water ice signatures. Such composition could possibly be due to collisions in Saturn's main ring or collisions between ring particles and an icy moon [*Kempf et al.,* 2005a]. Stream particles originating from the Jovian system were also observed, and the compositional analysis of CDA spectra confirmed the volcanic plumes of Io as their source [*Kempf et al.,* 2005b; *Postberg et al*., 2006]. In conclusion, CDA achieved sensitive detection of nanometer-sized dust and has shown that the compositional analysis can reveal information about their sources.

4.5.4. NDA Required Mass resolution

Due to their high-speed, nano-dust particles will result in a mass spectrum composed mostly of atomic ions with very few molecular and cluster ions, as was revealed in the CDA stream particle measurements (Fig. 4.6). Based on the expected composition of comets and asteroids described in Sec. 2.1.1, the elemental composition of the dust particles might include H, C, N, O, Na, Mg, Al, Si, S, K, Ca, Ti, and Fe. The mass resolution requirement is then likely driven by resolving the K and Ca peaks, which would be $m/\Delta m$ = 40 if they are similar in strength. The target material Rh will also show up in the spectrum at 103 *u*. CDA stream particle spectra shows cluster ion formation with Rh, such as $RhSi^+$ and $RhFe^+$, which must be covered by the mass range. Thus, a spectrometer sampling greater than 160 *u* with a mass resolution of $\geq m/\Delta m$ = 40 is required. Based on the performance verification of the NDA prototype (Sec. 4.9.1), the NDA will have sufficient mass resolution to measure ion species of interest.

4.6. Ion Optics Simulations

The NDA design was aided by the numerical simulation of the motion of the ions within the instrument using the SIMION software package [*Dahl,* 2000]. Due to the initial spread in the energy/angular distribution of the impact-generated ions and the finite size of the detector, only a fraction of the generated ions will be collected by the detector. As was discussed in the previous section, the initial spread in energies also widens the mass lines and limits the instrument mass resolution. Thus, the simulations are used to estimate the fraction of impact-generated ions collected by the detector, which plays an important role in the detector sensitivity requirements described in Sec. 4.7 and are also used to predict the instrument performance as a function of

mass resolution. The SIMION simulations are useful in guiding and confirming the high-level design of the NDA since instrument design parameters (e.g., target voltage, detector size, and ion flight path) influence the collection efficiency and mass resolution. A simplified geometry was modeled including the curved target and ion accelerator grid, the cylindrical instrument housing and the housing of the ion detector with the biased detector surface and the ion collection grid in front. It is important to point out that the initial energy and angular distributions of the impact-generated ions are unknown. It is believed that the ion energy is in the ~20–40 eV energy range and independent of velocity as reported by experimental measurements (see Sec. 4.4). However, they may be higher for velocities at which nano-dust particle impacts are expected. In the performed simulation, ion energies up to 50 eV were considered. Figure 4.7 shows a plot of the SIMION calculation of the ion collection efficiency as a function of voltage applied to the target (for a range of initial ion energies). The collection fraction increases with target voltage and is reduced for higher energy ions. For a nominal target voltage of + 3 kV and expected ion energies of ~ 40 eV, an ion collection efficiency of ~5% is expected. The SIMION simulations also indicated that for the instrument geometry used, the impact position would have only a small effect on mass resolution. This was later confirmed by the measurements performed on the prototype (see Fig. 4.15).

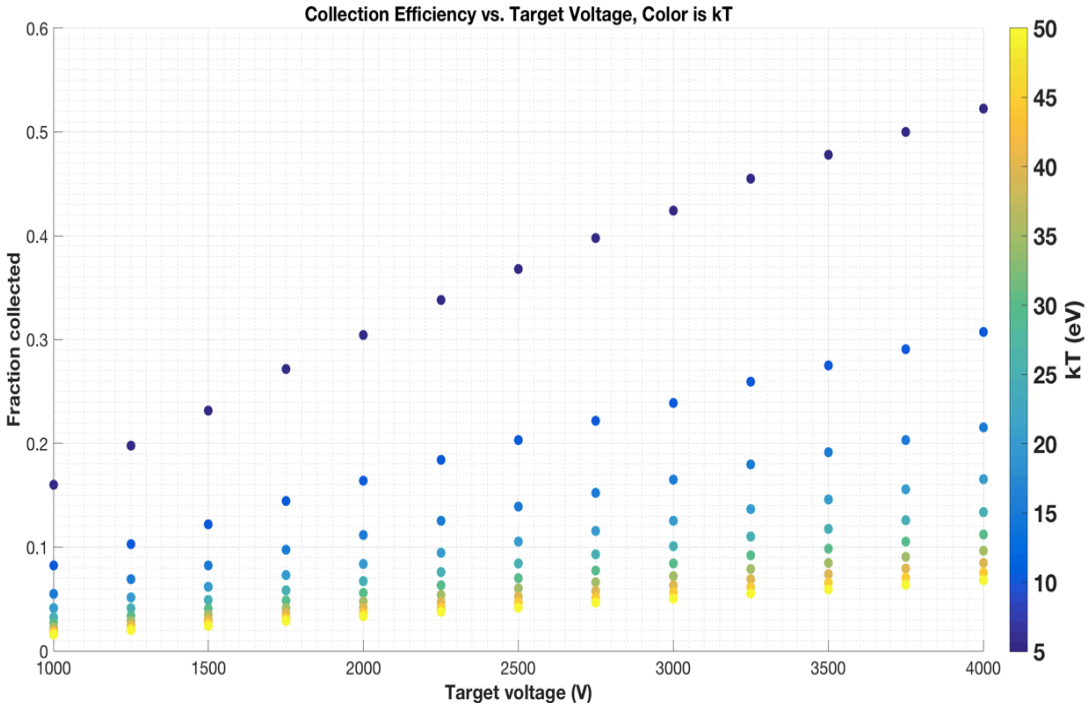

Figure 4.7 Fraction of impact-generated ions collected by the NDA ion detector as a function of voltage applied to the impact target. The color scale represents the initial distribution in ion energies assumed for the impact plasma and shows that for the expected ion energies and target bias of 3 kV, about 5% of the ions should be collected by the detector (courtesy of Ethan Williams).

4.7. NDA Ion Detector

The selection of the ion detector for NDA is driven by the instrument sensitivity and dynamic range requirements. The detector must be able to measure the smallest signal above the noise level, but also must be capable of measuring the TOF spectra from the strongest impact signals, without saturating the detector or signal-processing electronics. The expected speed distribution plotted against dust mass for the expected range of nano-dust and β-meteoroids (for typical solar wind conditions) is shown in Fig. 3.7. The mass and speed of the particles is converted to impact charge by the power law relation measured for the Rh target material $Q = 0.19mv^{4.34}$ [*Horanyi et al.,* 2015] and is plotted in Fig. 4.8. The impact charge varies over

several orders of magnitude, and for most particles, is within a range of about 10^{-13}–10^{-9} C. Note the impact charge plot flattens in the 10–50 nm range because the increase in mass is compensated by the decrease in velocity the particles attain from the interaction with the solar wind magnetic field. The large dynamic range in impact charge drives the detector selection to a discrete dynode electron multiplier such as the Hamamatsu R2362 coarse mesh Beryllium Copper detector. This detector can achieve a high dynamic range by measuring two signals of different gain from the detector.

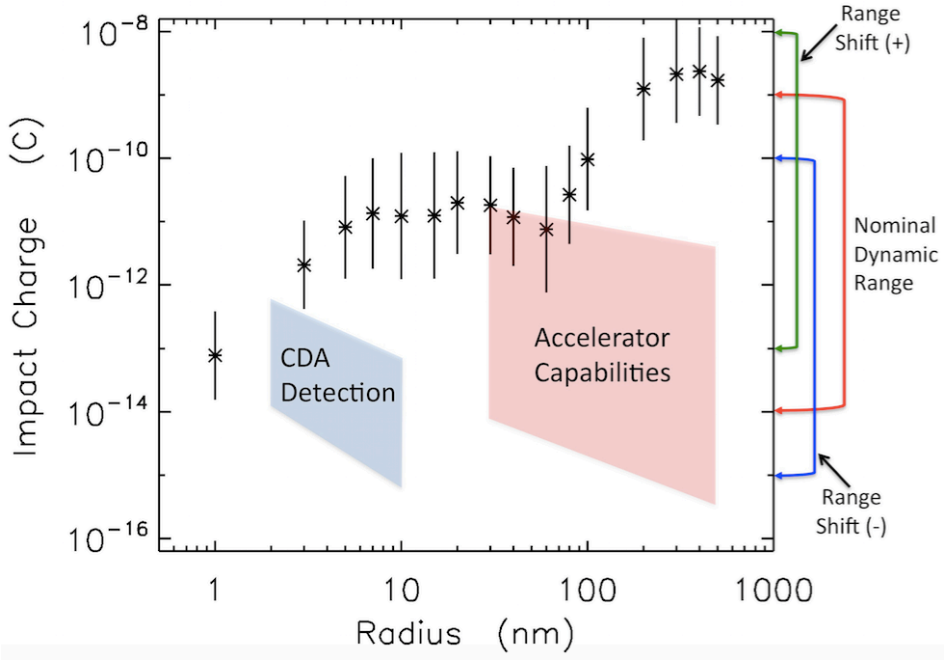

Figure 4.8 Expected impact charge as a function of dust size for a Rh target. The red shaded region shows the range in which accelerators can provide calibration measurements. The power law derived for the measured range was extrapolated to include nano-dust and *β*-meteoroids (shown here). The blue shaded area shows the impact charge corresponding to the nanometer-sized dust particles measured by CDA, indicating that even a 1 nm particle should be detectable by NDA, provided that the dynamical calculations presented in Fig. 3.8 are correct. The plot also shows the regions of impact charge covered by the detector's dynamic range and the ability to shift the dynamic range to cover signals from all dust particles of interest.

Approximately 5% of the impact-generated ions reach the detector due to the combined effect of the finite open area grids used in front of the target and detector, and the divergence of the ions produced. These results are based on the performed ion optics simulations (discussed in Sec. 4.6). In addition, a conversion factor of ~1 electron per incident ion is assumed for the Hamamatsu electron multiplier [*Hamamatsu Photonics K.K,* 2015]. Altogether ~5% of the ions generated in the impact are detected. Based on the impact charge values shown Fig. 4.8, this corresponds to an effective detected ion signal range of 10^{-16}–10^{-10} C. Thus, ~ 10^{-16} C, or 10^{3} ions, is the minimum detected charge in the TOF mass spectrum from the smallest (1 nm) nano-dust particle impact.

The detector must have sufficient dynamic range to measure the smallest signal above the noise floor, which is limited by the noise of the detector and the analog to digital converter (ADC) electronics. The detector must then also be able to measure the largest expected signal without saturating the electronics. To achieve this, the signal is measured at two locations in the stack, one high gain channel measured at the detector anode and another at a lower gain stage in the middle of the stack. If each channel is sampled with a 14 bit resolution, a dynamic range of 10^{5} can be achieved, covering signals from most of the dust particles of interest, as shown in Fig. 4.8. The voltage applied to the detector is adjustable between -1.5 – -4kV, allowing for adjustable gain since the detector gain increases with applied voltage. This allows the full range of dust particles to be covered and also provides some reserve gain in the case of performance degradation. Furthermore, the dynamic range is adjustable up or down by a factor of 10 as a result of the adjustable detector voltage (gain) as well as the adjustable target voltage, which can either increase or reduce the ion collection efficiency onto the detector.

As discussed previously in this chapter, most of the nano-dust and β-meteoroids sizes/velocity lie outside of the range of capability of dust accelerators. Thus, there is uncertainty in extrapolating the power law (derived from the impact measurements on Rh) relating impact charge to dust mass and velocity to nano-dust and β-meteoroids, so there is some uncertainty in the estimated impact charge. However, enabling adjustable detector gain addresses this uncertainty.

4.8. Development of an NDA Prototype

4.8.1. Mechanical Design

A laboratory prototype of the NDA instrument (Fig. 4.9) was developed as a proof of concept. The prototype differs from the NDA flight concept/design that has been described in previous sections. The prototype was developed with a number of simplifying compromises driven by the limited scope of the project which will be pointed out in this section. The instrument housing is composed of a 43 cm long cylindrical aluminum tube with a 22 cm inner diameter. The instrument geometry thus has a 60° full angle FOV. Instead of the more expensive process of Rh target development, the target surface is polished and coated with a layer of Ag doped with a small amount of sulfur to prevent the surface from tarnishing. The target has a 300 cm^2 area and is curved with a 30 cm radius. The acceleration grid is placed 1 cm in front of the target. The manufacturing of a 20 cm diameter curved acceleration grid was also outside of the scope of this project. Instead, the grounded ion acceleration electrode was manufactured out of solid aluminum. There is a 20 mm wide slit opening overlaid with an 80% open-area grid that is designed to approximate the shape of the acceleration grid surface.

The ion detector is enclosed in a short cylindrical aluminum housing and is held in place

using a three-legged mount 30 cm from the target. In the prototype, the ion detector is a two-stage micro-channel plate (MCP) with an active area of 2.5 cm^2. An MCP was initially selected as the ion detector due to its compact size, good time resolution, and extensive flight heritage. However, it was later decided that a discrete-dynode electron multiplier was necessary to achieve the dynamic range requirements, thus, the Hamamtsu R2362 was selected for the flight design (Sec. 4.7).

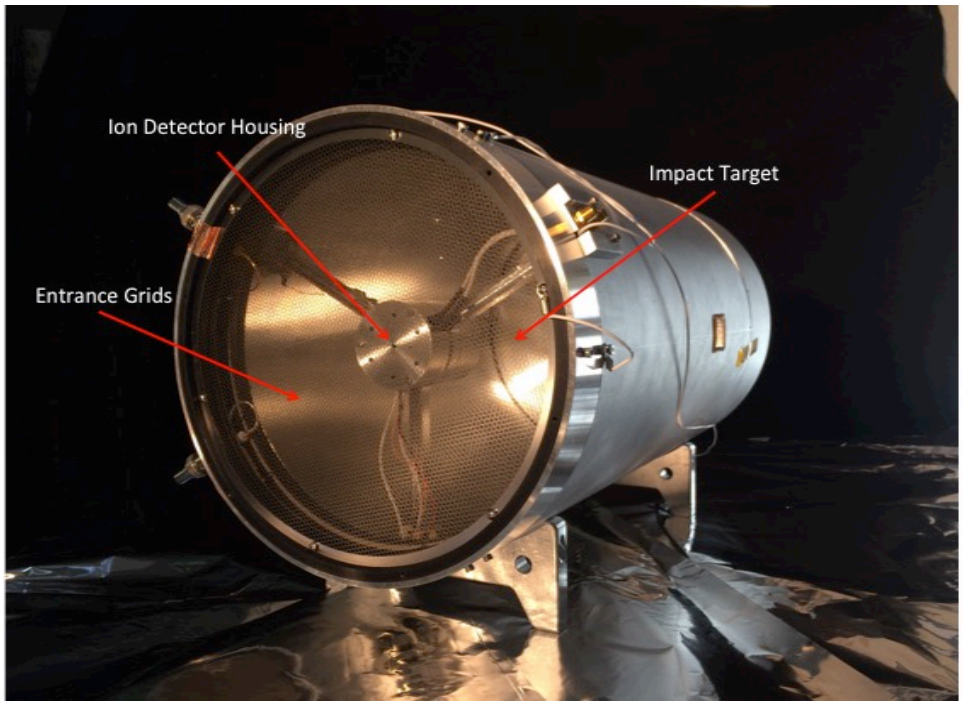

Figure 4.9 The fully assembled NDA instrument prototype. The instrument is 43 cm long and 22 cm in diameter. The target sits at the back of the instrument. At the front is the set of grids and the detector housing attached to the instrument walls by the three-legged mount.

The front-end electronics, including the CSA of the ion grid and the MCP transimpedance amplifier, are enclosed within the detector housing in close proximity to their

respective signal sources. All signal leads are shielded to reduce noise pickup. The prototype also includes the four identical solar wind rejection grids over the aperture. The manufacturing of highly transparent grids (~ 90%) necessary to achieve an effective sensitive area of 100 cm^2 (see Sec. 4.2.2) was out of the scope of the current development program. The grids integrated into the prototype are 0.18 mm thick with 80% open area and are manufactured by photo-etching. Figure 4.10 shows a schematic drawing of the lab prototype.

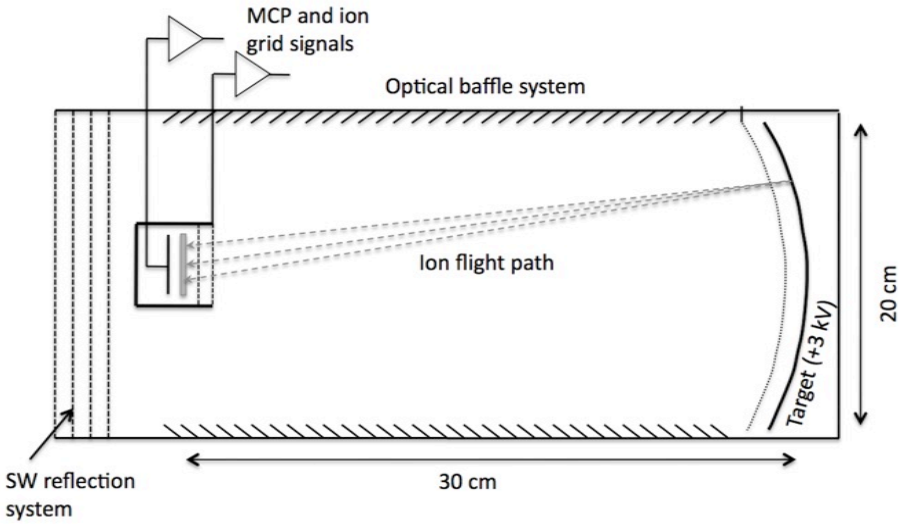

Figure 4.10 The schematic diagram of the NDA lab prototype. The dust particles enter from the left and pass through a set of grids before impacting the target. The ions are extracted from the impact plasma and focused onto the ion detector by an electric field applied between the target and the curved grid, which are separated by 1 cm. Note: optical baffles (like those shown) were not included during main functional testing (from *O'Brien et al.*, 2014).

4.8.2. Electronics

The laboratory version of NDA measures two analog signals: the charge of ions collected

on the ion grid mounted on the front of the detector housing, and the TOF ion signal from the anode behind the MCP. The total impact charge can be measured as the charge collected on the target, similarly to the CDA instrument [*Srama et al.,* 2004]. However, this signal channel is not implemented in the current simplified version of NDA.

The ion grid signal is measured using a charge sensitive amplifier (CSA) with the schematics shown in Fig. 4.11(A). The first stage is followed by an AC coupled second stage with a gain of approximately 6. The RC decay time constant is set at 100 μs, much longer than the arrival time of the ions. The bandwidth of the CSA is limited to 1 kHz–70 MHz. The gain and the noise levels were determined through laboratory calibration measurements to be 5×10^{12} V/C and 3 mV_{rms}, respectively. The MCP anode signal is connected to ground through a 50 Ω resistor and a voltage follower with a gain of 2 is used to drive the coaxial cable to the digitizer (Fig. 4.11(B)). A pair of diodes is used to protect the input of the amplifier from a potential breakdown of the high voltage applied to the MCP. The amplifier bandwidth is DC to 625 MHz and the noise is at a low level of 0.1 mV_{rms}. The electronics components were selected for low noise and large bandwidth. The electronics were designed to fit into the small volume of the ion detector housing. External laboratory supplies were used for both the high bias voltages and the low-voltage power for the electronics.

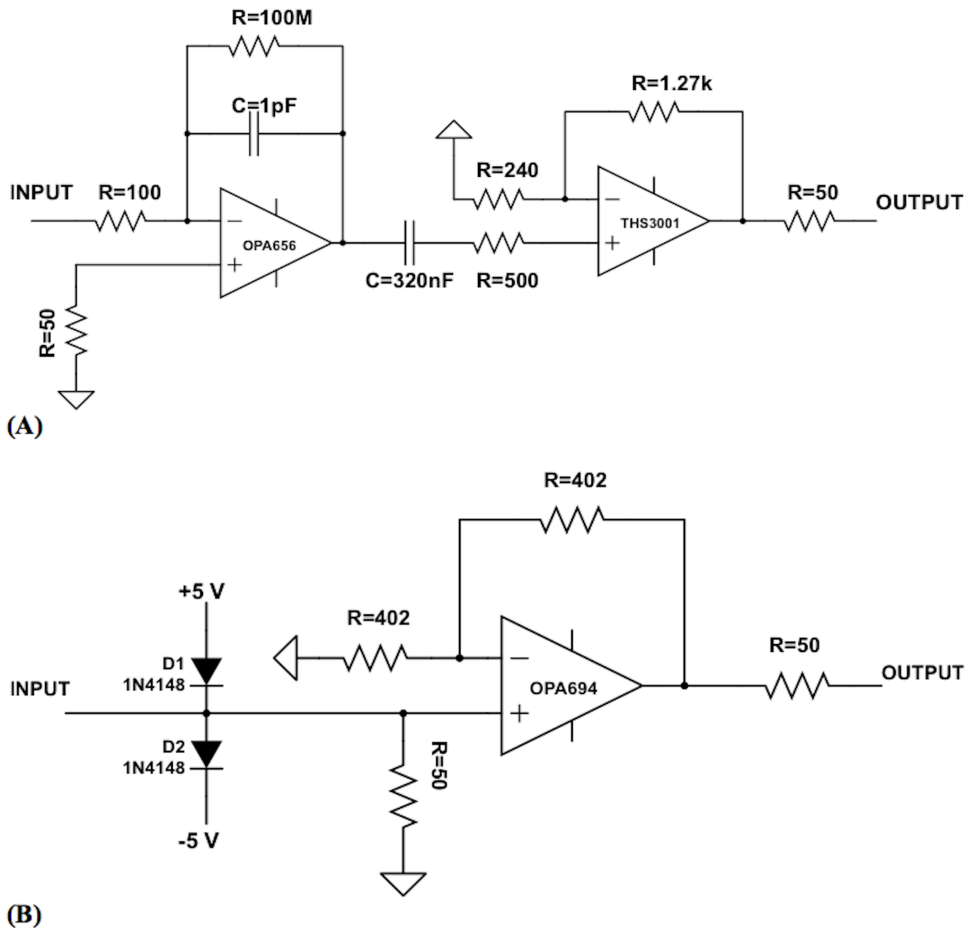

Figure 4.11 The schematic diagram of (A) the transimpedance amplifier of the TOF ion detector and (B) the ion grid charge sensitive amplifier (from *O'Brien et al.*, 2014).

4.9. NDA Prototype Performance Testing

4.9.1. Performance Measurements

The NDA was characterized using the 3 MV electrostatic accelerator at the accelerator facility. Spherical iron dust particles were used in the testing. The dust particles covered velocities ranging from 8–60 km s^{-1}. The NDA instrument was mounted on a linear-moving stage that allowed selecting the position of dust impacts on the target (Fig. 4.12). The impacting

particles were spatially distributed over a circle of 10 mm in diameter and the dust beam was aligned with the gridded portion of the acceleration electrode. The two main goals of the instrument's performance characterization were to determine the mass resolution as a function of the (1) target bias potential, and (2) impact position on the target. Altogether, about 900 TOF mass spectra were recorded. The velocity dependence was measured over the specified velocity range. The target bias was varied between +1.5 – +4 kV and additional measurements were made at -3kV to record the mass spectra of negative ions. The variation with impact position was measured for 2.5, 4, 5.5, 7, and 8.5 cm distance from the target center. The analog TOF mass spectra and ion grid signals were recorded using a 500 MS/s digitizing oscilloscope with 8 bit resolution. For increased dynamic range, the TOF signal was split and digitized simultaneously on two channels configured to different voltage ranges. These two signals were then combined into one before analysis. The bias voltage used to power the MCP detector was adjusted to optimize the signal amplitudes, and its typical value throughout the measurements was +1.4 kV.

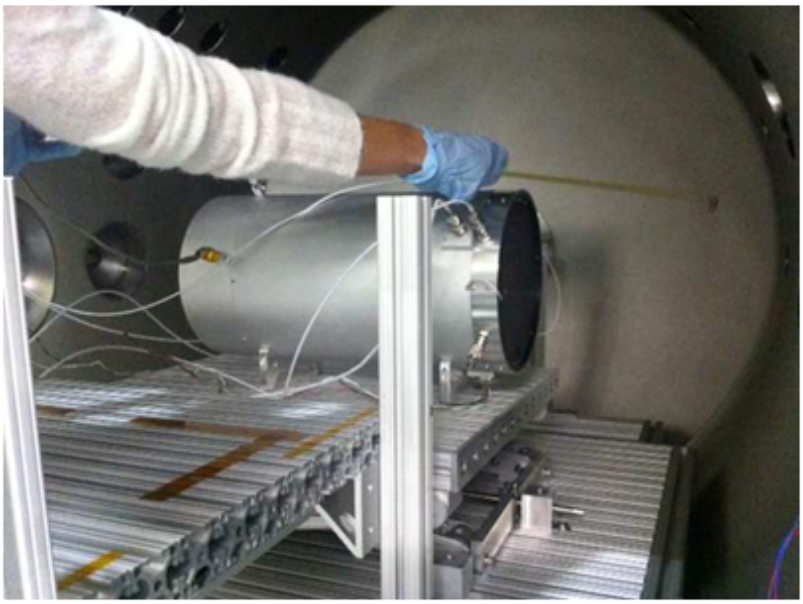

Figure 4.12 Picture of the NDA being mounted and aligned with the dust beam on the linear-moving table in the target chamber.

Figure 4.13(A) shows a typical TOF signal recorded, which is similar to those measured by related instruments [*Sternovsky et al.,* 2007]. The mass spectrum was analyzed using a previously developed interactive software package that can identify mass lines, calculate mass resolution, etc. The Fe and Ag peaks and their isotopes are the dominant mass lines in the spectrum and originate from the projectile and target materials, respectively. The abundance of ions in the spectrum is characterized by the area under the corresponding mass line. Various cluster ions (e.g., Fe_2, AgFe, Ag_2) are also commonly present. A number of mass lines in the spectrum originate from the small contamination present on the surface or within the bulk materials. The surface contamination by organic molecules is the expected source of H, C, and O ions, for example. The ions of alkali metals (Na, K) are often strongly pronounced or even the dominant contamination peaks due to their low ionization potentials. Contaminated mass spectra are more of a problem for lab measurements, which are performed in imperfect vacuum and

shortly after installment. In attempts at minimizing the effects of contaminations collected in space, periodic heating of the surface target can be employed, as was done on the CDA instrument, which was also carefully cleaned prior to launch using ion-sputtering methods.

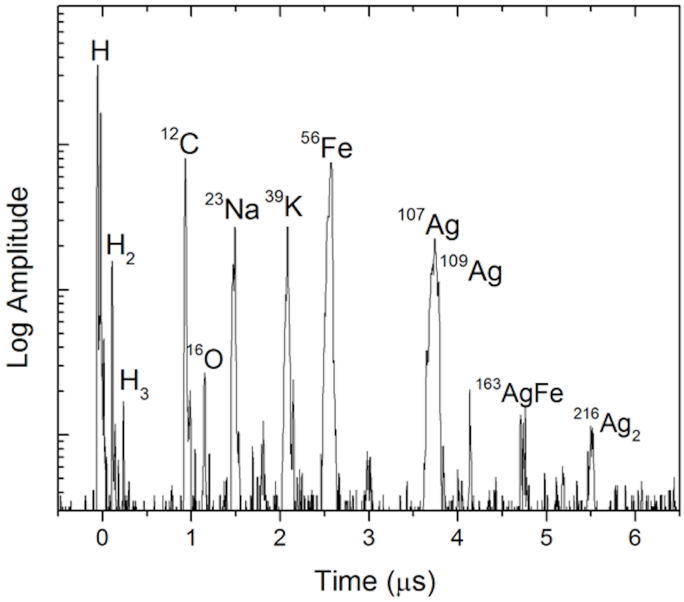

(A)

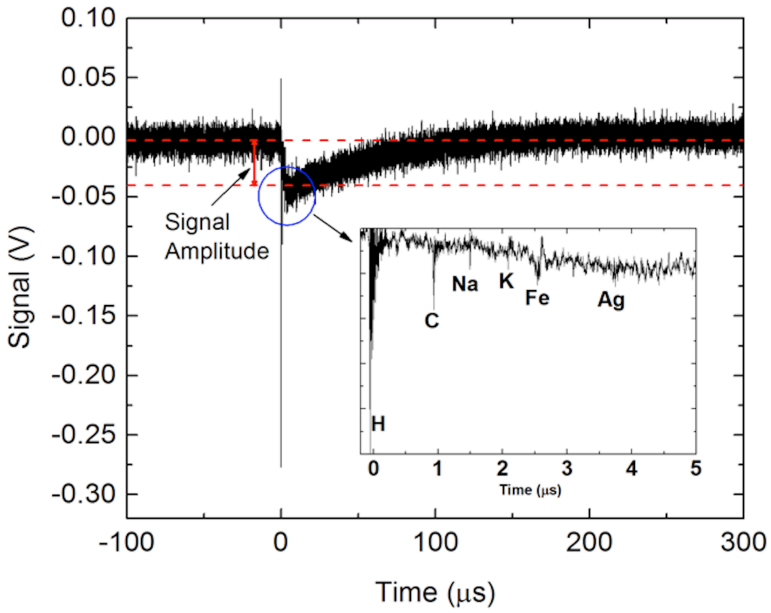

(B)

Figure 4.13 (A) A typical mass spectrum measured by the NDA instrument from a r = 120 nm iron dust particle impacting NDA's silver target at 20.8 km s^{-1}. Note the wide dynamic range in the vertical direction. (B) The ion grid signal obtained from the same dust particle impact. The signal amplitude corresponds to the total charge of the ions collected by the grid. The peak voltage amplitude of ~0.04 V is converted to a total collected charge of 2.4×10^{-14} C. The insert shows the fine structure of the signal, where the main mass peaks also show up due to the image charge that develops when the ions travel through the grid (from *O'Brien et al.*, 2014).

Figure 4.13(B) shows a typical ion grid signal, which is a measurement of the charge induced on the grid by ions on their way to the MCP detector. The ion grid will collect ~ 42% of the incoming ions. The amplitude of the signal rises on a time-scale dependent on the impact speed, and the peak amplitude of the signal corresponds to the total charge of ions that are collected on the grid. The voltage signal can thus be converted to a charge signal from the sensitivity of the CSA: 5×10^{12} V/C. The ion grid signal provides an estimate of the number of ions generated by the impact, particularly those that will reach the detector. The dominant mass peaks are revealed in the fine structure of the signal (Fig. 4.13(B) insert) as a result of the image charge that is produced by the ions that pass through the grids. Due to the angular spread of the ions during their time-of-flight, a measurement of the charge yield directly at the target provides a much better estimate of the total number of impact-generated ions than the measurement from the ion grid. Such a measurement will be incorporated in this instrument, but small impact charge yields become difficult to measure due to the increased noise levels attributed to the applied high voltage.

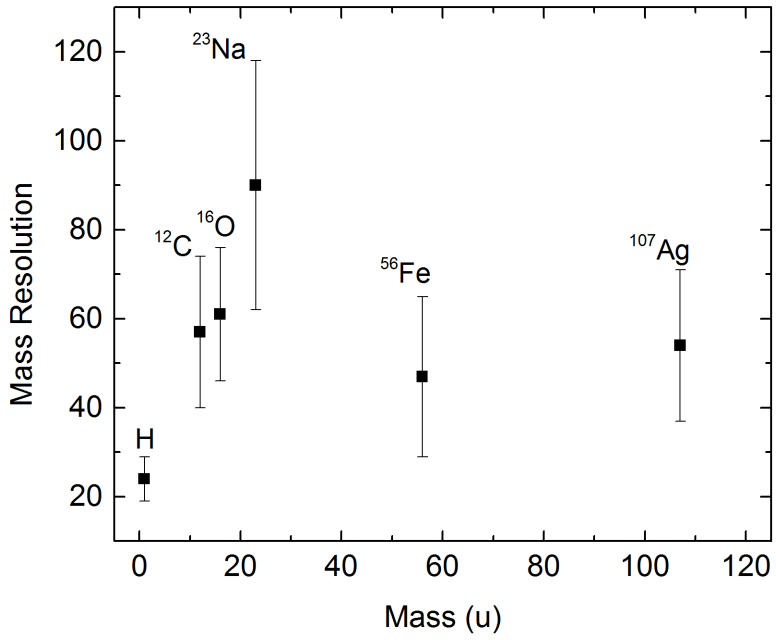

Figure 4.14 The mass resolution (FWHM) of the common mass lines when a +3 kV bias voltage is applied to the target. Note the difference in mass resolution for contaminant peaks (H, C, O, Na) versus the bulk material (Fe, Ag) (from *O'Brien et al.*, 2014).

Figure 4.14 shows the mass resolution of the common mass lines for the nominal conditions of +3 kV target bias voltage at the reference impact position. The set of spectra was taken for particles ranging in velocity from 8 to 60 km s^{-1}. Approximately 50 dust impact-generated spectra were analyzed for a given set of test parameters. The mass resolution in this analysis is defined using the full width at half maximum (FWHM). For the case of partially overlapping mass lines, the respective widths at half maximum are approximated. The data show that the typical resolution of the mass lines from the bulk material (Fe and Ag) are $m/\Delta m$ = 40−60. The contamination peaks (e.g. H, C, O, Na) exhibit significantly higher mass resolution possibly due to the different nature of the ionization process resulting in different

initial conditions, e.g. ion energy distribution. The mass resolution of these peaks apparently decreases with decreasing mass. This is due to the limited bandwidth of the analog electronics that artificially widens the mass lines for low masses, which have narrow peak widths as a result of shorter flight time/lower energy spread.

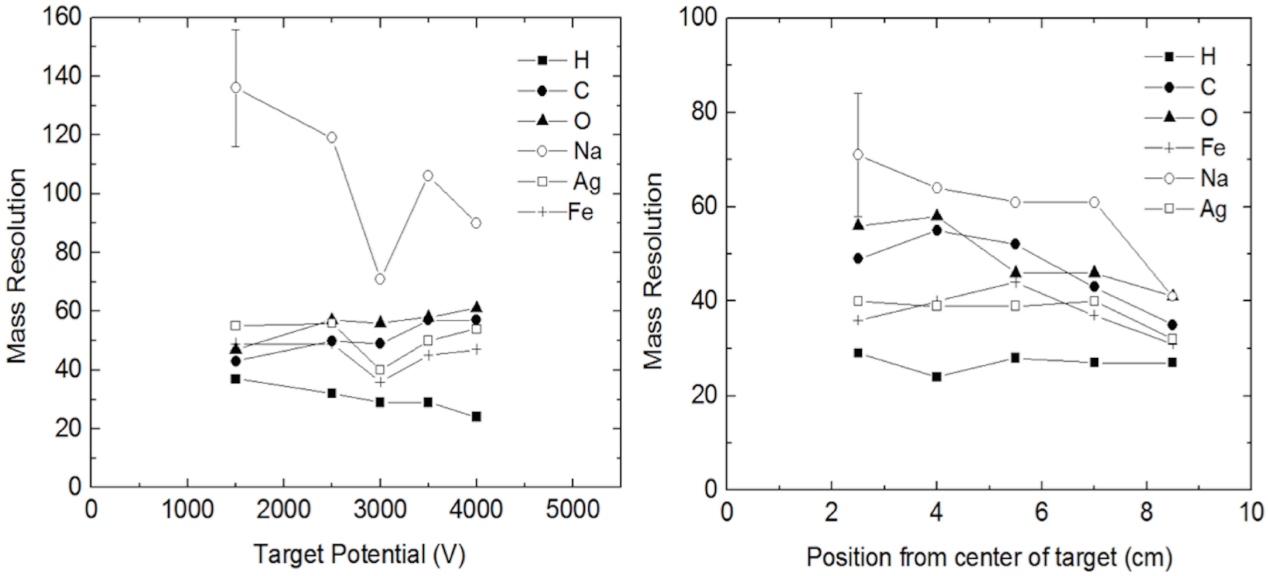

Figure 4.15 (Left) The mass resolution as a function of target potential for impact speeds of 8 km s^{-1} to 60 km s^{-1}. (Right) The mass resolution as a function of impact position on the target. A representative statistical error bar is shown in both plots (from *O'Brien et al.*, 2014).

Fig. 4.15 (left) shows the mass resolution for a selected number of mass lines as a function of the target bias potential. The impact location is kept constant at 2.5 cm from the center of the target and the projectile velocity range was set to 8 km s^{-1} and above. The figure shows that there is little variation in mass resolution with increasing target potential. The pronounced dip in the mass resolution for Na at +3 kV target potential is unexplained and likely

a statistical deviation. These results differ from the theoretical analysis of *Kempf et al.* [2012] where it is reported that an increase in the target potential will result in an increase in mass resolution. *Kempf et al*. [2012], however, ignores the angular distribution of the initial ion energy and the finite size of the detector. A possible explanation for the disparity is that with increasing target potential, ions from a wider angular distribution range are impacting the detector. This results in a wider spread of the arrival time of ions of the same mass that limits the attainable mass resolution. This property of the instrument, however, was not investigated further. Similar measurement sets are made by varying the dust impact positions on the target. The results (Fig. 4.15(right)) show that regardless of where the dust impacts the target, there will be little variation in the mass resolution, especially for the bulk materials (Fe, Ag).

4.9.2 Solar Wind Rejection Tests

Because NDA must point close to the Sun's direction, it is potentially sensitive to solar wind (SW) ions and electrons. These inputs may reduce its sensitivity to dust observations. Solar wind particles entering the instrument may be scattered or even guided into the detector, thus contributing to the background level, reducing the sensitivity of NDA. The duration of a TOF mass spectrum is on the order of 10^{-5} s (see Fig. 4.13(A)) and for a mass spectrum to be meaningful, it needs to consist of about ~10^3 ions reaching the detector. For the solar wind induced noise to be negligible, the number of solar wind particles that reach the detector in the TOF period needs to be much smaller, e.g. < 30, which corresponds to a tolerable rate at the detector of < $3\text{x}10^6$ s^{-1}. The typical flux of solar wind ions is 10^9 cm^{-2} s^{-1} and the total number of ions over the ~300 cm^2 aperture area is then 3×10^{11} ions per second. It is thus important to reject the majority of the solar wind ion flux. The SW electron flux is even higher; however, they are rejected by the high negative potential of the detector.

The NDA instrument employs three consecutive stages of rejection. First, the instrument is to be oriented such that no direct solar illumination reaches the impact target, which also eliminates almost completely direct access of SW to the target. Second, the NDA has an electron and ion rejection grid system at its aperture, which only lets neutral and high-energy particles pass into the interior. However, a small fraction of ions will be neutralized when making contact with the grids' edges and will enter the instrument and potentially scatter into the sensor. Third, not all of the particles that hit the target are reflected or produce positive ions that are guided to the detector. In this section, the tests related to the latter two points are discussed.

The grid system over the aperture of NDA is designed to reject most of the SW particles (both electrons and ions) from entering NDA. The -200 V applied on the second grid (Fig. 4.1) is sufficient to reject most of the SW electron population, which has a typical temperature of about 10 eV. The +4 kV bias applied to the third grid will reject all protons and most of the He^{2+} ions for typical solar wind conditions (assuming a typical SW velocity of 410 km s^{-1}, the kinetic energy of He^{2+} ions is about 1.75 keV). A small fraction of the SW is composed of heavier ions such as C, N, and O, but they are still rejected for typical SW speeds.

There are two known effects limiting the system's rejection of solar wind particles that need to be considered and discussed. The solar wind contains a ~10^{-5} fraction of neutral particles that will not be affected by applied electric potentials [*Gruntman,* 1997]. Also, some fraction of the solar wind ions will impact the grids and other surfaces of the NDA aperture and recoil as neutralized particles. These processes were also considered and analyzed for the design of the low energy neutral detector developed for the IBEX (Interstellar Boundary Explorer) mission [*Fusilier et al.,* 2009].

The NDA instrument was tested at the University of New Hampshire's Space Sciences

Facility to validate the effectiveness of the solar wind ion rejection grid and the potential influence of secondary effects, including those due to neutral particles. Figure 4.16 shows the schematics of the experimental setup. A 1 keV ion beam used for the testing was mounted behind a 2 cm diameter aperture. The source was mounted on a moving stage and a reference MCP detector was used for characterizing the beam. Measurements with the neutral portion of the beam were also performed by applying a +3 kV potential on the aperture, thus removing the positive ions from the beam. The detectors were operated in a pulse counting mode, i.e. with high gain and the output signal connected to a counter set up for single ion impact recognition and the number of ion detections over a set time were recorded. The ion beam was mounted over the location of the accelerator grid electrode with the slit opening (see Fig. 4.16).

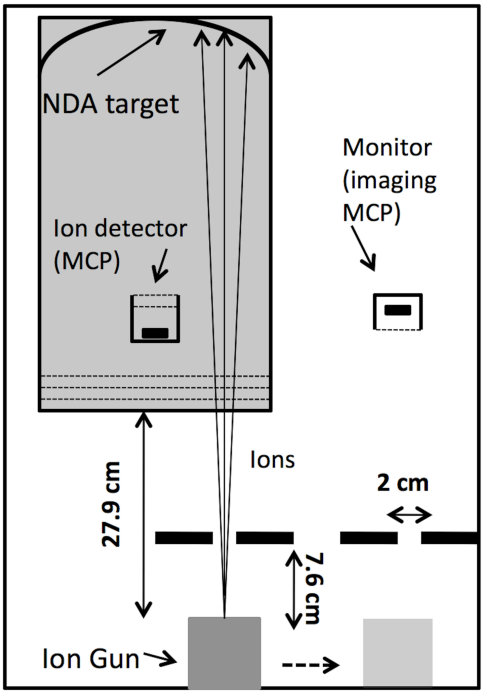

Figure 4.16 The schematic picture of the solar wind simulator test setup. The flux from the ion gun was periodically recorded using the monitor MCP to verify an unchanging ion flux (from *O'Brien et al.*, 2014).

Several key measurements were performed. The first was to test the effectiveness of the grid system rejecting particles. The beam was pointed at the NDA instrument and the number of ion impacts was measured as a function of the bias voltage on the ion rejection grid. At bias potentials higher than the beam energy, the number of ions that reach the detector drops by more than three orders of magnitude to the level of background noise (see Fig. 4.17). This result confirmed that the grid system as designed (10 mm separation between adjacent grids, ~3 mm opening cell sizes) is adequate for rejecting solar wind-like charged particles. The target potential was set to +3 kV for these measurements.

The second set of measurements aimed at providing a higher probability for ions to scatter from the grids and enter the interior as neutrals. This was achieved by installing another identical grid on top of the outermost grid. The results were then compared with that of the standard grid configuration. For both sets of measurements, the ion beam flux was measured to be ~ 10^5 s^{-1} and the fraction of neutrals in the beam is 10^{-3}, which is sufficiently larger than the solar wind neutral fraction (10^{-5}). Following the installation of the second grid, a noticeable increase in the fraction of incoming ions that scatter from the grids (and enter the instrument as neutrals) was not detected because this fraction still does not exceed the neutral fraction of the ion beam. Therefore, the neutral fraction of the beam is used as an upper limit for the fraction of ions that scatter into the instrument. The total fraction of ion beam particles (neutrals and grid-produced neutrals) entering the instrument interior was then estimated to be 2×10^{-3}. Of these particles, the fraction that reaches the ion sensor is ~10^{-3}, as deduced from the measurements.

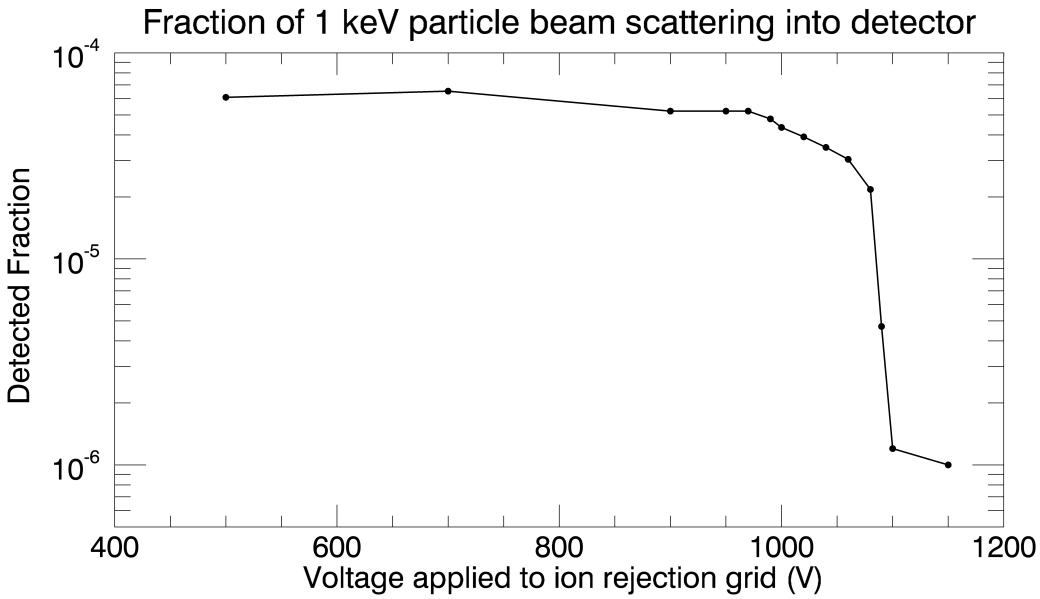

Figure 4.17 Measurements from testing with the solar wind rejection grids show that the fraction of detected particles drops significantly when the ion rejection grid is biased positively. A grid with > 1 kV potential applied is sufficient to reject incident positive ions with 1 keV energy. The plot shows that the remaining fraction that scatters into the detector (mostly neutrals and ions neutralized by grid impacts) is below the required 10^{-5} detected fraction for sensitive nano-dust detection.

The results from the measurements discussed above are scaled to the actual solar wind flux at 1 AU and reveal that, for a solar wind flux of 3×10^{11} s^{-1} incident on the NDA aperture, only $6x10^{5}$ particles per second will pass through the grids and scatter into the detector, which is smaller than the 3×10^{6} s^{-1} (10^{-5} detected fraction) requirement defined above. It must be noted that these results overestimate the number of solar wind particles that will reach the detector. The test setup enabled all particles that made it past the grids to directly scatter from the target into the detector. However, the instrument will be offset from the solar direction and at an angle relative to the solar wind flow. Many particles entering the instrument will directly impact the walls, making them less likely to reach the detector. In addition, the fraction of neutral particles in the solar wind is smaller than that of the ion beam used in the simulations. Therefore, the

number of particles entering the instrument and thus reaching the detector is further reduced from the results we report here. It is concluded from this analysis that by employing the rejection grids in the instrument, the typical solar wind flux at 1 AU will not interfere with NDA measurements. The 4 kV ion suppression grid will reject most of the SW ions in normal conditions, however, may be less effective against high energy particles that are present during CME events, for example. During such events, it is expected that the instrument will measure dust events with reduced-sensitivity. Also, the high-energy tail of the SW electron distribution can exceed 200 eV and also will not be stopped by the -200 V rejection grid [*Lazar et al.,* 2012]. However, the background noise associated with this distribution is estimated to be low in comparison with solar UV photons and is not expected to interfere significantly with the sensitivity of dust detection.

4.10. How NDA will Address the Science Questions

4.10.1. Confirm the Existence of Nano-dust

Firstly, NDA must confirm that the registered dust impacts are indeed nano-dust (or β-meteoroids). Typically, a calibrated impact charge measurement would allow for reasonable mass and velocity estimates. However, only a small portion of the expected particles lies within the calibration range (see Fig. 4.8). Furthermore, the impact charge tends to flatten out for a portion of the dust range of interest and thus wouldn't be a useful determination of dust mass and velocity. For NDA, the best method of estimating nano-dust mass and speed is by relating the dust flux directionality to the numerical trajectory analysis. Figure 3.8 shows that the smallest dust particles arrive nearly in the ecliptic plane, while the larger nano-dust distribution is spread over a larger range of latitudes. On a spinning spacecraft, NDA can scan at higher latitudes

(above and below the ecliptic plane). Larger particles will be detected when NDA is pointed above or below the ecliptic plane. Nano-dust dynamical calculations using the appropriate solar wind conditions will allow for interpretation of the nano-dust flux variability (in time and space) and relate to dust properties. In addition, Cassini's measurement of nanometer-sized dust particles will also be useful in interpreting impact charge measurements and TOF spectra. CDA observed very short rise times (~2 μs) in the impact charge signal [*Kempf et al.,* 2005b]. It is also worth mentioning that the Jovian and Saturnian stream particles' sizes and speeds were estimated through a combination of the measured fluxes and dynamics calculations, and similar methodology could be applied here [*Graps et al.,* 2000; *Hsu et al.,* 2011].

4.10.2. Investigate Nano-Dust Dynamics Through Interaction with the Solar Wind

The dust dynamics modeling described in Chapter 3 shows that the nano-dust flux variability in space and time are shaped by their complex interaction with the solar wind. The size distribution and flux is expected to vary as the NDA scans over zenith angles, as a result of the Lorentz force effects. Also, the variable distribution around the Sun of nano-dust reaching the Near Earth Orbit region as a result of the configuration of the IMF that they are interacting with translates to a temporal variation in the flux observed by NDA. Thus, the observed fluxes, paired with knowledge of the spacecraft position and NDA pointing and FOV, can be traced back to the dynamical interaction of nano-dust with the solar wind. Flux variations due to nano-dust interaction with solar transient events like ICMEs, as discussed in Sec. 3.7, can be significant and measurable as well. Theoretical modeling of the nano-dust interaction with the solar wind, for the appropriate solar wind conditions, will be crucial in interpreting the flux variability. The nano-dust could potentially be traced back to their place of origin, yielding information about the distribution of nano-dust near the Sun.

4.10.3. Determine the Source of Nano-Dust

One of the goals of the NDA nano-dust composition measurements is to constrain the sources of nano-dust and determine the relative contribution of cometary and asteroid material. NDA has the resolution necessary to identify the elemental constituents of nano-dust. Similar to the method performed by CDA's identification of stream particles, recorded mass spectra with similar characteristics will be grouped into respective types. For example, the 'CHON' type of comet-born dust particles may be identified by with a large abundance of H, C, O, and N, and the 'rock' type will be show Si, Fe, and Mg. Identification of silicate minerals, such as Olivine (containing Mg, Fe, Si, and O) can be representative of asteroid-originating dust particles. Supporting calibration measurements with coated olivine particles belonging to the nano-dust size/velocity portion that lies within the accelerator's capability (see Fig. 4.8) will aid in identifying the mineral in the TOF spectrum.

4.11. Summary of NDA Instrument Development

A fraction of the ejected nano-dust and β-meteoroids ejected from the inner Solar System will reach Earth's orbit, where they can be detected and analyzed. The NDA linear TOF mass spectrometer has been developed to measure the nano-dust fluxes and their chemical composition. The instrument development effort is driven by the design/operation requirements and constraints that allow NDA to successfully address the key science questions, like the determination of nano-dust sources and the details of their interaction with the solar wind. A laboratory version of NDA has been built and tested at the dust accelerator facility operated at the University of Colorado. The results show that NDA has the adequate performance and resolution power for the expected mass spectra. The nano-dust particles arrive from near the

Sun's direction, posing strict requirements on the instrument design and operation. Experimental investigations show that the instrument performance will not be compromised when exposed to typical solar wind particles. The design optimization under solar UV illumination is also addressed and will be discussed in Chapter 5.

Chapter 5: Optimization of the NDA for Operation Under Solar UV Illumination

5.1. Overview

This Chapter presents the optimization of NDA for close Sun-pointing and is based on the work described in *O'Brien et al.* [2015]. The expected arrival directions of the nano-dust and β-meteoroids (Fig. 3.8) determined by the numerical modeling described in Chapter 3 reveal that the dust particles will be arriving from directions close to the Sun (e.g., the smallest nano-dust arrive in ecliptic plane, ~20° from the solar radial direction). Thus, NDA will need to point close to the Sun to measure the expected fluxes. Furthermore, the entire distribution covers a range of zenith angles. Therefore, the instrument field-of-view (FOV) must accommodate these measurement requirements.

The challenge in detecting and analyzing the nano-dust particles is in the pointing requirement of NDA that is close to the Sun's direction. Some fraction of the solar UV photons entering through the aperture will inevitably scatter into the ion detector. The generated background noise then reduces the signal-to-noise ratio (SNR) of the recorded TOF spectra and

also limits the lifetime of the ion detector. The straightforward way to reduce the level of UV background is to limit the field-of-view (FOV) of the instrument and avoid pointing at or near the Sun's direction. This approach, however, is in conflict with the desire of a large FOV instrument capable of detecting the nano-dust particles from all directions simultaneously, including that of the Sun's. This chapter describes the analysis performed to characterize the instrument's performance under UV irradiation and presents the optimum compromise for sensitive detection of nano-dust particles by the NDA instrument in terms of FOV and pointing requirements. The expected UV noise background is analyzed in detail and a combination of low-reflectivity optical coatings and baffles are used to reduce it to acceptable levels. The analysis is performed using the ray-tracing program *Zemax* for Lyman-α radiation, which has the most significant effect on NDA. The analysis shows that only an instrument with a relatively narrow FOV provides a feasible solution. This means that the continuous monitoring of nano-dust particles arriving from all expected directions requires operation from a scanning platform or spinning spacecraft. With the Sun in the FOV, the instrument is still capable of measurements but with reduced sensitivity and for a limited duration.

The sections below are organized as follows. The requirements for acceptable UV background are derived in Section 5.2. Section 5.3 discusses the general properties of UV reflection from surfaces and the contribution to noise from Lyman- α. Section 5.4 describes the design of the optical light trap system using baffles. Section 5.5 describes the performance analysis. Sections 5.6 and 5.7 present the results from the analysis and requirements on all optical surfaces that are necessary to reduce the UV effect to the required level and the conclusions, respectively.

5.2. Operation Requirements

Sensitive detection and mass analysis of the dust particles of interest requires that the TOF spectrum ion signal be clearly detectable on top of the noise background due to solar UV photons scattering into the detector. Solar UV photons will generate background noise by scattering into the ion detector where they have sufficient energy (≥ ~5 eV) to liberate electrons from the detector surface with some efficiency of detection. UV photons entering the instrument will also generate secondary electrons from other surfaces in the instrument (e.g. walls, target) but the ion detector is biased at a high negative potential (between 2 and 4 kV) and will repel photoelectrons, which have much lower energy, thus the main contribution to noise will come from photons scattering directly into the ion detector. A simple estimate of the maximum UV photon flux can be made as follows. At the high impact velocities expected from nano-dust particles (> 60 km s^{-1}) atomic ions dominate the mass spectrum. The highest significant mass line in the TOF spectrum then will be from the Rhodium target material. The FWHM width of this Rh mass line is about 35 ns long, based on the resolution power and the instrument geometry as discussed in Chapter 4 [*O'Brien et al.,* 2014]. A reasonable goal in the compositional analysis with the NDA instrument is to clearly resolve mass lines that are composed of ≥ 1% of the total charge generated ~10^{-14} C, or 10^5 generated ions (from Fig. 4.8). For a SNR ≥ 10, this means that the flux of detected UV photons should be smaller than one detected photon in the 35 ns duration, considering worst-case scenario. In other words, the flux of detected UV photons needs to be limited to 3×10^7 s^{-1}.

There is another limitation on the UV background level, which is the lifetime of the ion detector. The ion detectors considered for NDA start to degrade after a total of 1 C cm^{-2} charge is driven through [*Hamamatsu Photonics K.K.*, 2006]. The effective area of the ion detector is ~2.5

cm^2. Assuming the detector is operating with a gain of 10^4 electrons per incident ion and a multi-year mission with continuous operation yields a limit of $< 10^7$ s^{-1} detected photons, i.e. slightly more restricting than the condition for resolving TOF ion spectra. Considering the uncertainties discussed throughout this chapter, and design goal maintaining ample margin, the optical performance of the NDA instrument described below is designed to achieve a $< 10^5$ s^{-1} rate of detected photons for sensitive nano-dust analysis measurements.

The solar UV photons entering the instrument will scatter from the internal surfaces and some fraction will reach the ion detector, where they are detected with some probability. Reflectivity and properties of photon scattering depend on the wavelength λ, the angle of incidence (AoI), and the properties of the scattering surfaces. The quantum efficiency of detection (QED) is the probability that a photon is detected that is also a function of λ. For bare MCP detectors, for example, the QED reaches close to 10% for $\lambda < 10$ nm and decreases with increasing wavelength [*Martin and Bowyer,* 1982]. For the complete analysis of the UV background noise, a part of the solar spectrum with $\lambda < 250$ nm (approx. 5 eV photon energy) would need to be considered. However, the reflectivity and scattering properties of the surfaces of interest are poorly known in the UV range and simplifying assumptions are needed. Figure 5.1 shows the cumulative contribution from the solar UV radiation weighted by the QED of the detector for a case where the detector is directly exposed to the Sun. This is calculated as:

$$\int_0^{\lambda_{max}} S(\lambda) QED(\lambda) d\lambda \tag{5.1}$$

where $S(\lambda)$ is the solar irradiance spectrum for solar maximum conditions (assuming the worst case) [*Chamberlin et al.,* 2008]. The figure shows that the intense Lyman-α ($\lambda = 121.6$ nm) line

accounts for about half of the total contribution, the other half comes from shorter wavelengths, and longer wavelengths are relatively unimportant. The ray-tracing analysis of the NDA instrument presented below is thus performed with a simplifying assumption that all of the solar UV radiation (photons with $\lambda < 250$ nm) occurs at Lyman-α wavelengths at a flux of with 3×10^{10} cm^{-2} s^{-1} flux (note: this is an 'effective flux', as it already includes the QED of the detector). This assumption is conservative as photons with shorter wavelengths generally have a lower probability of reflecting from a surface and are less likely to reach the detector. It should also be noted that the QED used here is that reported for an MCP detector, but is similar for the Hamamatsu electron multiplier [*Hamamatsu Photonics, K.K.,* 2015]. The aperture of NDA instrument is approximately 300 cm^2 and thus the total influx is ~ 10^{13} s^{-1} . As derived above, the requirement is to reduce the number of detected UV photons to a rate ≤ 10^5 s^{-1}. This means that, for nano-dust measurements, NDA instrument needs to be designed such that, on average, less than one out of 10^8 photons entering the instrument scatters into the detector.

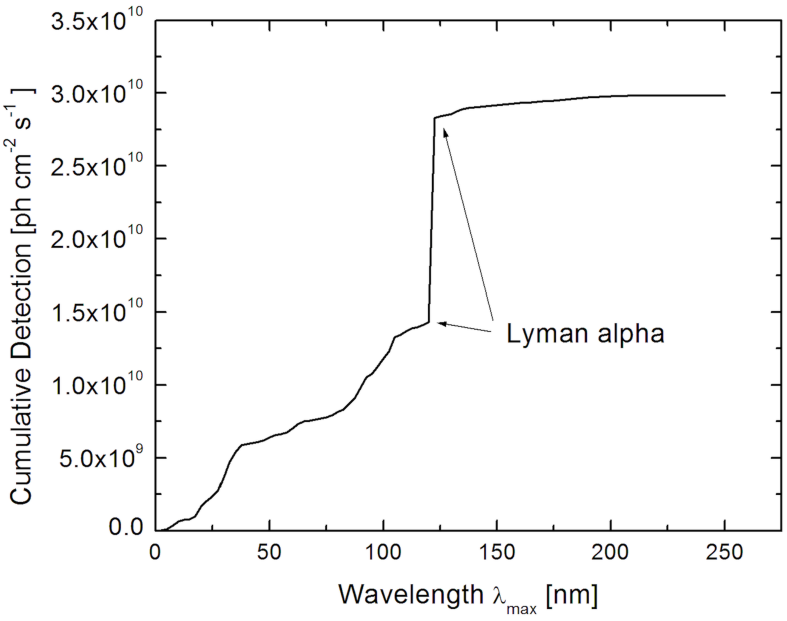

Figure 5.1 The cumulative contribution from solar UV radiation at 1 AU, where the wavelength-dependent QED is factored in. The Lyman-alpha emission line contributes to nearly half of the detected radiation and shorter wavelength radiation is mainly responsible for the other half (from *O'Brien et al.*, 2015).

5.3. NDA Surfaces

Three types of surfaces are assumed to interact with the incoming UV within the instrument: (1) the Rh target, for which the reflectivity is R = 0.09 for Lyman-α radiation at normal incidence [*Samson and Ederer,* 1999], (2) bare metallic surfaces without optical treatment or polishing (e.g., grids), with reflectivity (total fraction of incident power reflected by surface) assumed to be R = 0.1 for Lyman-α at normal incidence, and (3) the optical baffle system coated for very low reflectivity. The scattering properties of surfaces are determined by the ration of the Root Mean Square (RMS) roughness of the surface σ and the wavelength of incident light λ. Highly polished surfaces ($\sigma << \lambda$) reflect dominantly in the specular with a small

fraction scattering into a cone around the specular direction. For moderately rough surfaces ($\sigma \approx \lambda$), the component that is diffusely scattered about the specular direction becomes more important. Rough surfaces ($\sigma \geq \lambda$) generally exhibit a Lambertian scattering profile for all angles of incidence (AoI), in which the scattered intensity exhibits a $cos(\theta_S)$ angular distribution. The integral scattering properties of very rough surfaces deviate from Lambertian, especially at large AoI. The ratio of integrated scattered radiation to the specular reflected radiation is known as the total integrated scatter (TIS):

$$TIS \approx R\left(\frac{4\pi\sigma^2}{\lambda}\right)^2 \tag{5.2}$$

where R is the total reflectivity of the material that is also a function of λ and AoI. Low-reflectivity surfaces have rough morphologies consisting of micro-cavities, where photons undergo multiple scattering that increases the probability of absorption (see Fig. 5.2). Only a very limited number of surface treatments are characterized in the UV. An additional requirement for NDA is to use conductive or at least dissipative surface coatings to eliminate the buildup of surface charges that would alter the trajectories of the ions within the instrument. *Zurbuchen et al.* [1995] reported the scattering properties for incident radiation at the Lyman-alpha wavelength for a variety of rough surface treatments, including CuO, Ni black and Cu_2S. The integral reflection coefficients of these treatments are 0.005, 0.03 and 0.02, respectively, measured at normal incidence. The scattering properties of a surface are described by the Bidirectional Reflectance Distribution Function (BRDF), which can be expressed in the following form:

$$BRDF(\theta_I,\theta_S,\Phi_I,) = \frac{P_S(\theta_I,\theta_S,\Phi,)}{P_I \Omega \cos\theta_S} \tag{5.3}$$

where P_I is the incident power, P_S is the scattered power, Ω is the solid angle through which the incident power scatters, (θ_I ,Φ_I) and (θ_S, Φ_S) describe the direction vectors of the incident and scattered light in spherical coordinates and ~θ is measured from the surface normal (see Fig. 5.3). It must also be noted that BRDF is dependent on the wavelength λ, but is assumed for a single λ here. Equation 5.3 is used to approximate the BRDF using measurements of incident and scattered power. Ω, thus, describes the solid angle subtended by the detector. Isotropic Lambertian scattering surfaces are characterized by a BRDF profile that is constant across all θ_S. This is because both the scattered light measured and the projected area of the illuminated spot vary as a $cos(\theta_S)$.

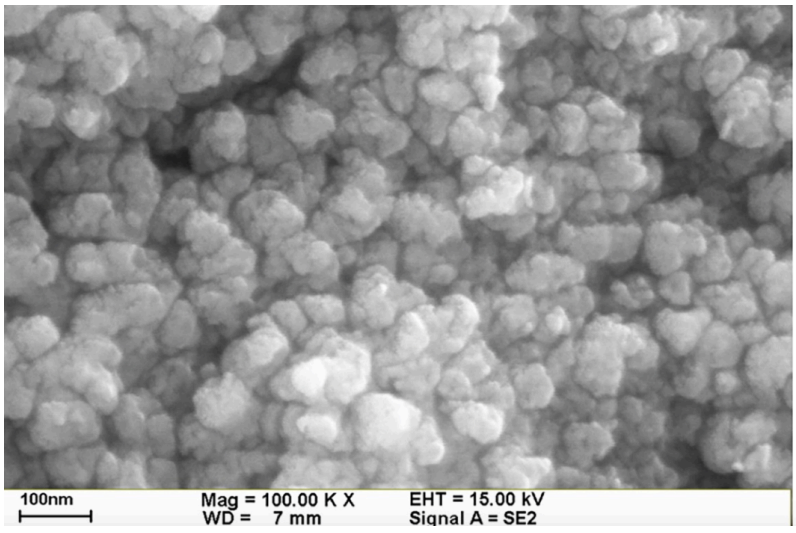

Figure 5.2 A scanning electron microscope image showing the surface morphology of oxidized copper shows spongy structures that can easily trap UV radiation (figure from *Lee et al.*, 2016).

For the coatings listed above, *Zurbuchen et al.* (1995) reported that the BRDF profiles exhibit Lambertian characteristics (constant BRDF) for small incident angles, but for large incident angles (> 60°), the reflectance properties depart from Lambertian and exhibit dominance in the specular direction, as well as enhanced backscatter into the direction of incidence, $\theta_S = \theta_I$, (see top plot of Fig. 5.4). For the analysis of the NDA instrument, CuO is the surface treatment of choice because it exhibits very low reflectivity in the UV and the BRDF data is available for Lyman-α radiation. While CuO is very weakly conductive, it has been used for UV rejection in electrostatic analyzers and its presence typically does not compromise the analyzer's performance when applied as a thin layer (E. Möbius, personal communication, 2013). Experimental verification will still be necessary.

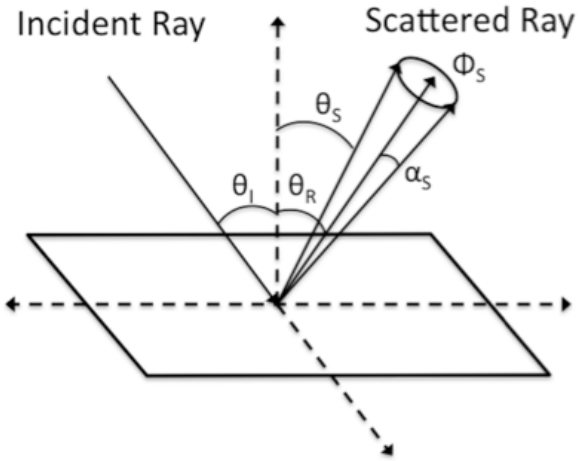

Figure 5.3 Scattering geometry from a planar surface. θ_R is the specular reflection angle and is defined in the same plane as the incident angle θ_I. The cone surrounding the specular direction represents the scattered radiation distribution where θ_S is the scattering angle defined relative to the surface normal. Here α_S is the scattering angle defined relative to the specular direction and ϕ_S defines the azimuth about the specular direction where ϕ_S = 0°(180°) corresponds to a scattering angle α_S in the plane of incidence to the right (left) of the specular direction.

Zurbuchen et al. [1995] measured the BRDF in the plane of incidence for a set of incident angles and reported the distribution of the scattered light intensity with a resolution of 1.5° These data are imported into the *Zemax* model as a user-defined scattering profile to implement the scattering properties of CuO into the ray trace analysis. The BRDF data are input for the measured incidence angles ranging from $\theta_I = 0°$ to 88° and scattering angles between $\theta_S =$ -90° and +90°, with a 2° resolution, within the plane of incidence through interpolation of the experimental values. Both the BRDF data and integral reflection coefficient is defined in the scattering profile for each angle of incidence. In the *Zemax* scatter profile, the scatter angles are defined relative to the specular direction as α_S, as depicted in Fig. 5.3, which describes the scattering geometry from a planar surface. The BRDF data is reported for scattering angles θ_S measured with respect to normal incidence. Thus, the data is input to the model using the relation $\alpha_S = \theta_S - \theta_R$ for $\phi_S = 0°$ and $\alpha_S = \theta_R - \theta_S$ for $\phi_S = 180°$ (see Fig. 5.3 for definitions).

The BRDF scatter data is measured only in the plane of incidence ($\phi_S = 0^\circ, 180^\circ$), but the complete range of scattering angles α_S are defined for ϕ_S between 0° and 180° under the assumption that the scattering is azimuthally symmetric about the specular direction. For small angles of incidence, where scattering is essentially Lambertian, this is a valid approximation. For larger angles of incidence ($> 60^\circ$), the BRDF is not quite symmetric about the specular angle. In this case, the BRDF measured at $\phi_S = 0^\circ$ is assumed for $0^\circ < \phi_S < 90^\circ$, and the BRDF measured at $\phi_S = 180^\circ$ for $90^\circ < \phi_S < 180^\circ$. The lack of measured data outside of the incident plane introduces uncertainty to the model and is taken into consideration when interpreting the analysis results.

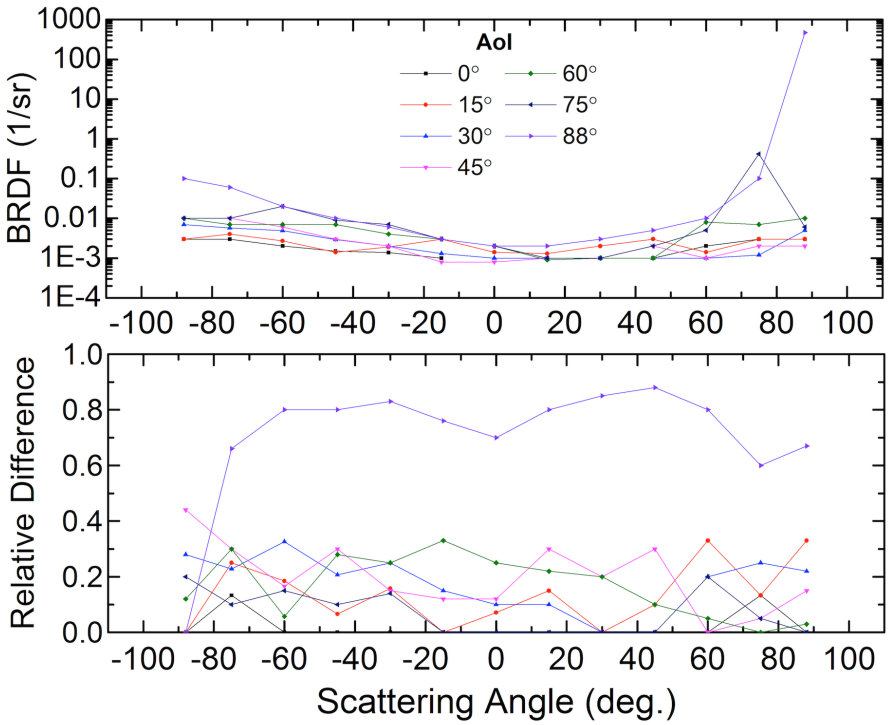

Figure 5.4 (Top) The measured BRDF data from *Zurbuchen et al.* (1995) plotted as a function of scattering angle θ_S in the plane of incidence at various AoI. The BRDF profile is relatively flat for small AoI but has a strong enhancement in the specular direction for AoI = 75° and 88°. (Bottom) The difference between the experimental BRDF values and those recovered from *Zemax*, relative to the experimental BRDF values using the user-defined scattering model: [$BRDF_{model}$-$BRDF_{measured}$]/$BRDF_{measured}$ (from *O'Brien et al.*, 2015).

A simple *Zemax* model set-up was created to verify that the user-defined scattering profile implemented in the optical analysis reproduces the experimental BRDF data. A scattering surface is illuminated at AoI (θ_I) ranging from -88° to 88° in 15° increments. Detectors are also positioned with 15° increments within the plane of incidence. The detector size and distance from the target are selected to achieve an angular resolution of 2° through the relationship $sin(2°) = r_{det}/d$ where r_{det} is the radius of the detector and d is the distance from the center of the scattering surface to the detector. This provides a reasonable representation of the experimental

setup, in which a 1.5° resolution was reported. The ratio of the detected scattered power to the total incident power $P_S(\theta_I,\theta_S) / P_I$ is calculated numerically yielding back the BRDF function via Eq. (5.3). Figure 5.4 shows that the recovered BRDF from the numerical model is close to the experimental data, confirming the validity of the user-defined scattering model used in *Zemax*. For most angles of incidence the relative difference is < 40% and this value will be used as the estimated error of the scattering model used. The relative difference is somewhat larger for AoI = 88°, which might be from the imperfect scattering model, or from measurement error.

5.4. Optical Baffle System

The preliminary analysis of the instrument found that it is necessary to reduce the number of photons scattering off the inner surfaces of NDA instrument and thus the inner walls are lined with a set of optical baffles. Both the baffles and the underlying instrument wall are coated with ultra-black CuO for efficient light trapping. The baffles are spaced 1 cm apart and have a 22 cm outer diameter and a 20 cm inner diameter, so they do not obstruct the sensitive target area. (depicted in Fig. 5.5). The baffles are described and optimized in terms of their conical geometry, i.e. the angle at which they are exposed to the incoming radiation. Fig. 5.5 shows the baffle geometry at two example cone angles: 90° and 20°. The performance as a function of the cone angle is discussed in detail in Section 5.5.

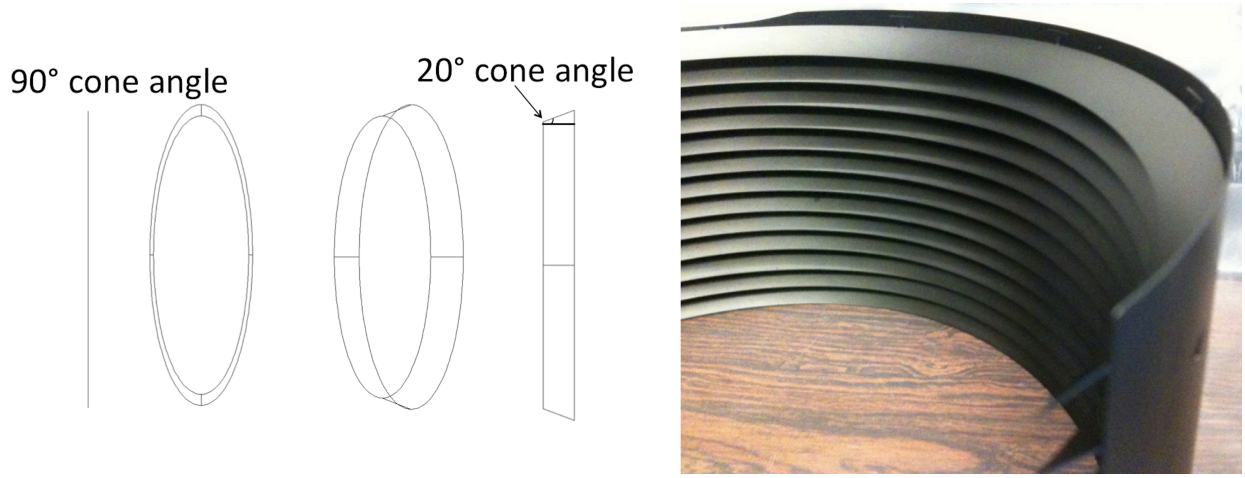

Figure 5.5 Optical baffle geometry. Left: The optical baffle with a 90° cone angle is a flat ring with 20 cm inner diameter and 22 cm outer diameter, followed by an optical baffle with a 20° cone angle. The cone angle is defined relative to the axis of cylindrical symmetry. Right: sample optical baffles manufactured and coated with Anoplate ™ AnoBlack (Ni)Te coating for incorporation into the NDA prototype (note: the optimal CuO coating material was outside of the scope of this project, but is intended for use in the baffle system to be incorporated in a flight instrument).

5.5. Optical Analysis of NDA

5.5.1. Overview

The geometry of the instrument surfaces and surface material optical properties plays a critical role in reducing photon scatter into the detector. NDA was designed for an effective target area of 100 cm^2, mass resolution of $m/\Delta m > 40$ to resolve the most common elements, and limited FOV that enables the detection of nano-dust while mitigating the effect of UV photons [*O'Brien et al.,* 2014]. The NDA instrument design is further optimized in terms of geometry and surface scattering properties using the commercially available ray-tracing software *Zemax*. In *Zemax*, a radiation source is specified with a 'total incident energy' and a number of rays. The energy is divided equally between the rays, which are released into the instrument, free to interact with the surfaces. Based on the specified surface scattering properties, the rays will be

reduced in energy each time they interact with a surface in the instrument. Each ray will take a unique path of scattering throughout the instrument, and its final energy is recorded once it reaches the detector. The fraction of 'incident energy' recorded by the detector is synonymous with the fraction of incident photons that reach the detector. In the model, it was specified that individual rays are traced until they either reach the detector or are reduced in energy to 10^{-10} relative to the initial value, after which their contribution to the detector signal is considered negligible, as it is much less than the limit of detected photons ~ 10^{-8} of the incident photons. The cumulative energy at the detector, and thus, the total number of photons reaching the detector, is reported and compared with the requirements (Sec. 5.2). The paths of rays reaching the detector are analyzed in order to evaluate and improve NDA's performance. The numerical simulations are performed for Sun pointing angles from $\theta = 0°$ to 60° (i.e., Sun angle relative to the cylindrical axis of the instrument).

5.5.2. Instrument Geometry Optimization

The instrument geometry is optimized to reduce the UV background by adjusting the length of the instrument, which in turn sets the FOV. The size of the target and the placement of the ion detector remain the same. In addition, optical surfaces can be introduced to reduce the number of photons reaching the detector. These, in turn, may obstruct the target and reduce its effective area.

The major observation geometry and functionality constraints are driven by the need of photons to undergo multiple scattering before reaching the detector in order to meet the optical performance requirements defined in Sec. 5.2. If the target is even partially illuminated with direct sunlight, as in the case of small source angles (smaller than about 20°, see Fig. 5.6), the fraction of photons scattering from there directly into the detector is too large, regardless of the

selected target material or scattering model applied. For sensitive nano-dust measurements, this limits possible Sun pointing to > 20° in order to avoid the direct illumination of the target surface. With the target directly illuminated, the instrument sensitivity is reduced. Similarly, it is imperative to prevent the direct scattering into the detector from illuminated baffles. This latter effect warrants introducing an extension of the detector housing, as shown in Fig. 5.6. This extension is conical in shape, with a geometry that does not restrict ions generated at the target from reaching the detector. The extension is also coated with CuO. The length of the instrument and size of the cone are optimized such that the instrument maintains a reasonable effective target area, while extending the range of possible sun pointing angles.

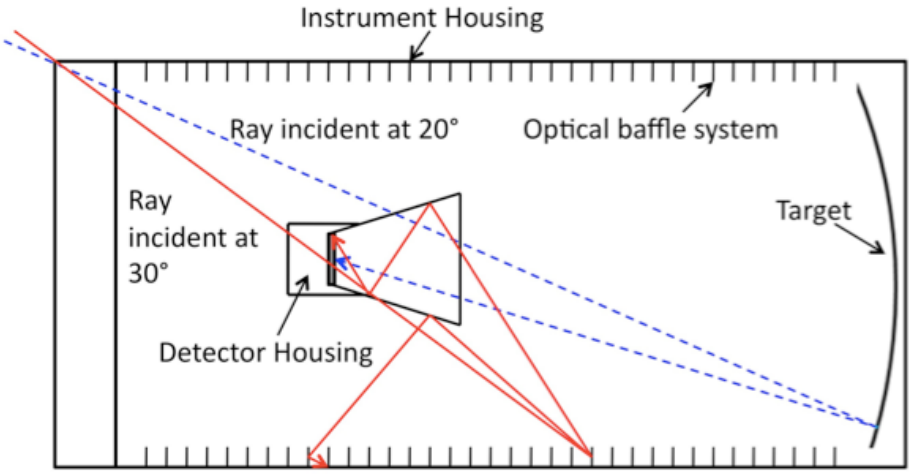

Figure 5.6 Simplified NDA model used in *Zemax*. A ray entering at 20° with respect to the cylindrical axis may scatter directly into the detector from the target. Rays entering at 30°, on the other hand, can scatter directly from the baffles toward the detector. A conical extension to the detector housing is used to prevent photons from reaching the detector from a single scattering event within the instrument (from *O'Brien et al.*, 2015).

5.5.3 Effect of the Aperture Grids

The four solar wind rejection grids at the instrument's aperture can potentially scatter UV photons onto the target and then eventually into the detector. Preliminary mechanical analysis shows that grids etched from 125 μm thick molybdenum sheets of high open area (~92%) with hexagonal pattern are sufficiently strong to withstand space launch conditions and are assumed for the analysis below. The hexagonal openings are 3 mm wide and the grids are spaced at 10 mm from one another.

Light scattering from the entrance system may terminate at the detector, so a separate analysis was performed to determine what fraction of the incident photons scattering from the entrance grids reaches the detector. Scattering properties of the entrance grids are treated as described in Sec. 5.3. Due to their fine details, the high-fidelity modeling of the grids is difficult. The simple analysis discussed below proves, however, that the light scattered off the grids has a negligible contribution to the UV noise background. Since the grid thickness is much larger than the wavelength of Lyman-α radiation, direct scattering from the exposed edges dominates over other effects (e.g., diffraction). Photons impacting on the front (outward facing side) of the grids either reflect back to space, or are absorbed, and multiple scattering between grids is neglected. Solar UV photons can scatter into the instrument only from the inner sides of the hexagonal openings. Based on the number and dimensions of the grids and the etch pattern, the effective exposed scattering area is ~ $sin(\theta)\times(10\ cm^2)$, where θ is the Sun pointing angle and ~10 cm^2 is the sum of the exposed scattering surface from the individual hexagonal openings. This scattering area is distributed roughly uniformly across the aperture of the instrument and in *Zemax* it is modeled using line array sources spaced 3 mm apart. The intensity of the sources is adjusted to include the reflectivity of the material and have Lambertian distribution into 2π

steradians based on the argument that the scattering distribution is approximately Lambertian (see Sec. 5.3). For a representative θ = 30° Sun pointing angle, the grids contribute to the background signal only with a fraction of the incident flux ~10^{-15} for the case with CuO coated grids and ~10^{-14} for uncoated surfaces. Both of these values are much lower than the required 10^{-8} and thus the effect of the grids can be neglected.

5.6. Analysis Results: Performance-Driven Instrument Geometry

The NDA design is analyzed in *Zemax* and the number of UV photons scattered into the detector is reduced below the requirement. Here it is reported that NDA can make sensitive nano-dust analysis measurements as long as it is pointed away from the solar direction by at least a minimum Sun pointing angle θ_{min}. The instrument design requirements and their effect on the FOV and effective target area are also reported. Figure 5.7 depicts the pointing geometry of the instrument with respect to the Sun and the expected direction of the nano-dust flux at 1 AU where an orbiting spacecraft could detect nano-dust.

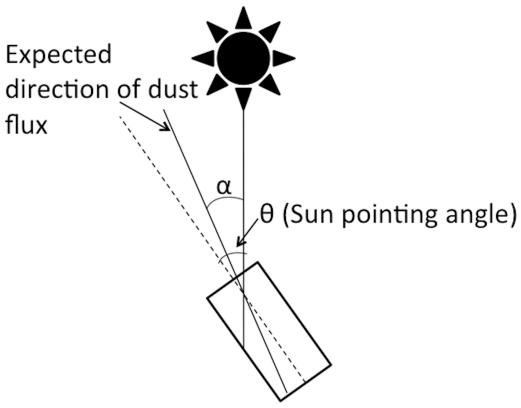

Figure 5.7 NDA pointing geometry. *θ* represents the pointing angle of the instrument with respect to the Sun's radial direction. *α* represents the angle that the direction of the expected dust flux at 1 AU makes with the solar radial direction (from *O'Brien et al.*, 2015).

First, the effect of the baffle geometry is investigated (Sec. 5.4). Effects due to variations in the baffle length and the spacing between baffles were studied and show that these variations do not have a significant effect of the number of photons scattering into the detector. The baffle cone angle does have a rather significant effect, however. Figure 5.8 shows the results of a ray trace analysis where only the cone angle is changed. The geometry analyzed is a 48 cm long instrument with a FOV of 22.6°. The conical extension of the detector housing is 9 cm in length and opening diameter of 7.9 cm (shown in Fig. 5.9). The results indicate that the background signal decreases with increasing cone angle, although all three cases ≥ 50° provide excellent and similar performances. Baffles with a 90° cone angle (see Fig. 5.4) will be considered further as this option has the benefit of being the least complicated to manufacture.

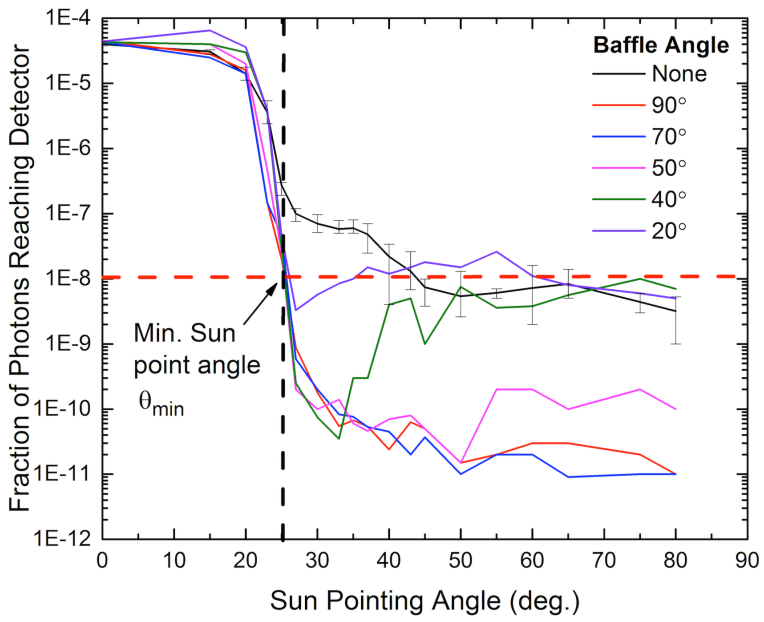

Figure 5.8 The fraction of photons scattering into the detector as a function of Sun pointing angle for a range of baffle cone angles. The red dashed line on the horizontal axis identifies the requirement of photons scattering into the detector below which sensitive dust measurements can be made. The black dashed line on the vertical axis labels the minimum Sun pointing angle. The error bars are indicative to all data shown and describe the standard deviation for the ray tracing analyses (from *O'Brien et al.*, 2015).

The UV noise background of the instrument depends on the Sun pointing angle θ, the size of the conical detector housing extension and the length L of the instrument, which in turn sets the FOV through relation FOV = $tan^{-1}(D/L)$, where D = 20 cm is the diameter of both the aperture and impact target. In order to have the results directly comparable, the simulations were performed as follows: First, the minimum Sun pointing angle θ_{min} is selected to be 20°, 25°, 30°, or 35°. θ_{min} is defined as the closest pointing of NDA to the Sun while keeping the UV background noise below the required level, which is depicted in Fig. 5.8 where θ_{min} = 25°. Then the instrument's FOV is selected noting that it is limited to FOV ≤ θ_{min} in order to avoid the

direct exposure of the target surface. The last step is the iterative adjustment of the length and outer diameter of the conical detector housing to a point where the instrument satisfies the θ_{min} selected in the first step. Each combination of the selected θ_{min} and FOV values thus results in a viable instrument geometry option.

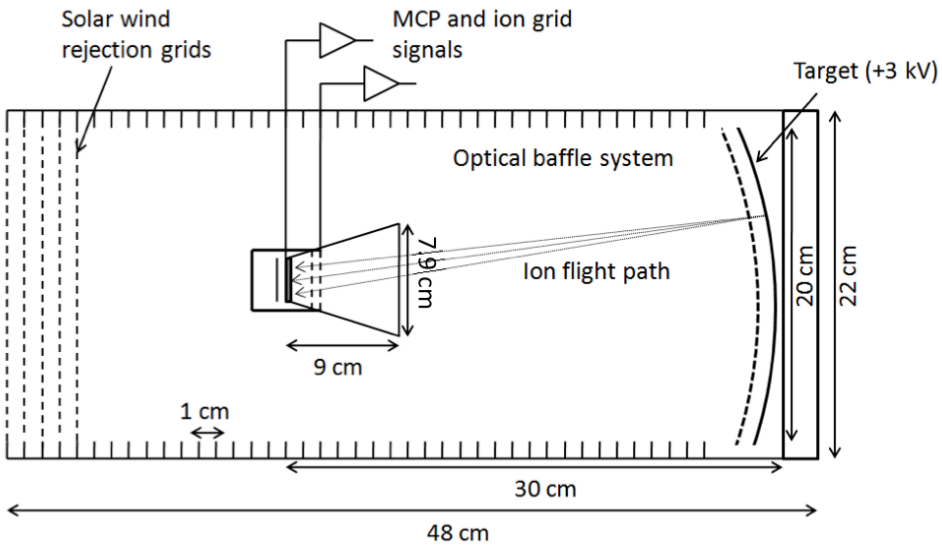

Figure 5.9 Schematic drawing of the NDA instrument, optimized for exposure to UV radiation. The optical baffles here are shown in their optimized geometry (from *O'Brien et al.*, 2015.)

The next step is evaluating the instrument geometry options in terms of effective target area, considering the expected direction from where the nano-dust particles arrive (see Fig. 3.8). Fig. 5.10 shows the effective target area of NDA instrument for Sun pointing angle of θ_{min} and two different cases of dust arrival angles, $\alpha = 20°$ and 25°. For the case of small particles arriving with $\alpha = 20°$, it is clear that the largest effective target area is reached also for $\theta_{min} = 20°$ (direct

pointing into the dust flux), however, at an expense of very limited FOV. This is because as the instrument's length is reduced and FOV improved, the detector housing extension must be increased in size to allow for the θ_{min} pointing. Limited FOV would require more elaborate scanning of the instrument, when searching for nano-dust particles in flight, and also limiting the number of detections. On the other hand, by making the FOV large, the effective target area diminishes quickly for the observation of $\alpha = 20°$ particles, as the instrument cannot be pointed close to the direction they arrive from. A compromise is reached by selecting instrument geometries with FOV between 22.5° and 25° and a conical detector housing extension that allows for observations with θ_{min} = 25–30°. The evaluation for case $\alpha = 25°$ yields similar conclusions. A possible instrument design option is one which achieves $\theta_{min} = 25°$, a FOV of 22.6°, and effective target area 166 cm^2 (245 cm^2) for a predicted dust arrival at $\alpha = 20°$ (25°). The instrument design includes optical baffles with a 90° cone angle, an instrument length of 48 cm, and a conical detector extension with length 9 cm and outer diameter of 7.9 cm. The inner walls of the instrument housing, optical baffles, and conical detector extension are all coated with CuO. This design is illustrated in Fig. 5.9 and its ray trace analysis results are shown in Fig. 5.8 by the red plotted line.

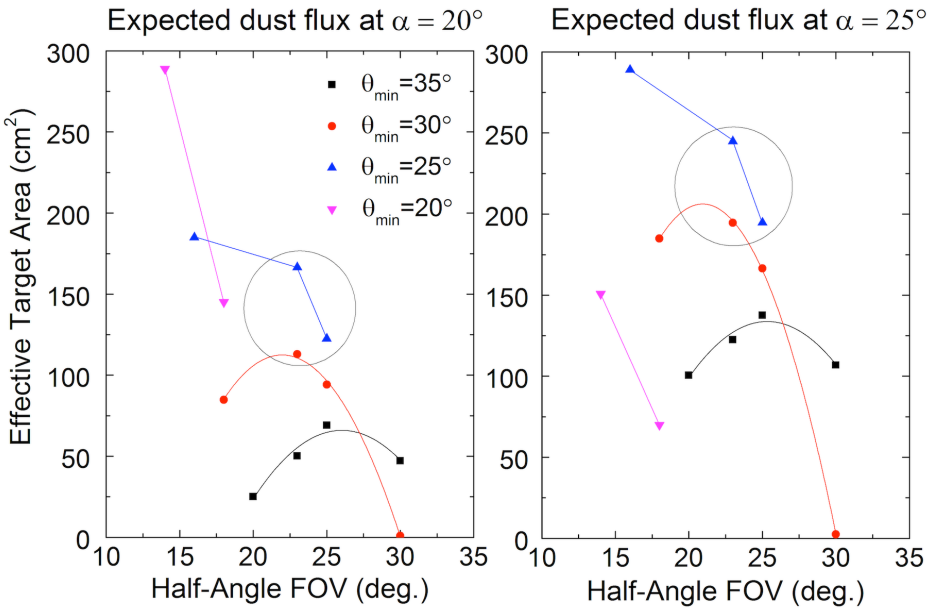

Figure 5.10 Effective target area plotted against instrument FOV for instrument designs optimized for a particular θ_{min}. Each plotted point represents a unique instrument design. The optimum instrument designs, shown circled, represent a reasonable compromise between the effective target area and the FOV (from *O'Brien et al.*, 2015).

The comparison of instrument geometries presented above and the selection of a viable option is based on the current understanding of nano-dust dynamics and the modeling results described in Sec. 3.5.3. Nevertheless, it is clear that close pointing to the Sun is a possible, if not the most likely arrival direction and thus mapping out this region is important. The analysis and optimization presented here is a big step towards defining the NDA instrument to make important observations related to nano-dust. The analysis shows that the instrument is capable of making sensitive nano-dust measurements while pointed ≥ 20° from the Sun, but at the expense

of the instrument FOV and effective target area. To detect the full distribution of nano-dust, a relatively narrow FOV is unavoidable. Thus, the use of a spinning spacecraft or scanning platform is likely necessary.

The analysis presented here is based on a requirement to detect the ion composition of the nano-dust impact generated plasma with 1% sensitivity even for the smallest (r_g = 1 nm) particles considered. The ray-tracing modeling shows that such sensitive measurements are possible as long as the direct illumination of the target is avoided. This would mean that the particles arriving directly from the solar direction would elude detection. The analysis in Sec. 5.2 presents that the detection of 10^{-16} C impact charge requires a factor of 10^{-8} reduction in the number of photons reaching the detector with a factor of margin built in. Figure 5.8 indicates that with NDA pointed directly at the Sun, $< 3\times10^{-5}$ of the incident photons would be detected. This would mean that dust impacts that generate an impact charge larger than about 10^{-14} C are still clearly detectable above the background noise, albeit with reduced sensitivity for mass measurements. Most nano-dust particles, however, would still be above this detection limit. A periodic pointing of the NDA instrument at the Sun would thus be possible to look for dust particles arriving from that direction. The duration of such observations would need to be limited because of detector lifetime issues, and/or compensated for by operation at lower detector gain.

5.7 Conclusions

NDA is analyzed for performance under solar UV illumination and it is concluded that sensitive detection of dust and composition analysis is possible with an optimized instrument design (i.e. inclusion of optical baffles and instrument geometry adjustments), proper optical treatment of surfaces using ultra-black coatings such as CuO, and avoiding direct Sun-pointing.

Table 1 shows a summary of the results from the optimization methods. This is a big step forward in the definition of the operation requirements for NDA that would enable the discovery of important science related to nano-dust origin and the chemical differentiation of matter in the inner heliosphere, as well as nano-dust dynamics and interaction with the expanding solar wind. The results of the analysis imply that sensitive dust measurements can be made at Sun pointing angles $\geq 20°$, but at the expense of the FOV and effective area of the target. The relatively narrow FOV that is required cannot provide full mapping of the nano-dust distribution, thus scanning the instrument is unavoidable and would require either a spinning spacecraft or a scanning platform. Scanning over the full distribution would entail direct Sun pointing, at which detection of nano-dust is possible but with a reduced sensitivity that will require further investigation.

Analysis Parameters	**Fraction of incident Photons Scattered into Detector**
• Direct illumination of target	$\sim 5\times10^{-5}$
• No direct illumination of target • CuO coated instrument walls • CuO coated conical detector housing	$\sim 10^{-7}$-10^{-8} (varies with Sun pointing angle)
• No direct illumination of target • CuO coated instrument walls • CuO coated conical detector housing • CuO coated baffles (optimized geometry)	$\sim 10^{-10}$-10^{-11} (varies with Sun pointing angle)

Table 5.1 The fraction of photons scattered into the detector as a function of the analysis parameters. The performance requirement is a maximum photon fraction of 10^{-8} reaching the detector. The results related to direct target illumination hold regardless of optimized instrument geometry, added baffles, or coating.

Chapter 6. Conclusions

This thesis poses some important questions regarding the interplanetary dust population in the inner Solar System. What are the sources, sinks, as well as collisional and evolutionary/transport processes of dust within 1 AU? What is the size and spatial distribution of the inner Solar System dust complex and its variability? Submicron (β-meteoroids) and nanometer-sized dust particles are generated close to the Sun where the dust density is high and are transported away from the Sun through radiation pressure and solar wind electromagnetic forces. A fraction of these particles cross Earth's orbit where they can be observed. Detection and compositional analysis of nano-dust and β-meteoroids that are ejected to Earth's orbit reveal information about the origin, distribution, and transport processes of dust originating near the Sun. Furthermore, nano-dust interact strongly with the solar wind and the spatial and temporal variability in their measured fluxes can report on the nature of dust-solar wind coupling, another outstanding question.

This thesis has described the development of the Nano Dust Analyzer (NDA) to explore the near-Sun dust complex at 1 AU. The linear time-of-flight mass spectrometer has been designed to detect nano-dust and β-meteoroids transported from the inner Solar System to Earth's orbit and measure their elemental composition. Numerical modeling of the dust dynamics is performed and described in this work to provide some insight into the way the solar wind and interplanetary magnetic field shapes nano-dust trajectories and their spatial and temporal distribution at 1 AU. An additional preliminary investigation of nano-dust interaction with interplanetary coronal mass ejections shows that the unique interaction can result in the delivery of nano-dust to near Earth's orbit in high concentration.

The NDA concept and design is driven by the performance requirements and is discussed in detail. The numerical model calculations of the nano-dust and β-meteoroid velocity distribution and arrival directions reveals that NDA must point close to the Sun's direction (~20–25°) and scan over a range of zenith angles to measure the full distribution. This close Sun-pointing requirement presents a challenge for NDA, which will need to be able to make sensitive dust measurements while exposed to solar UV radiation and solar wind particles. A detailed optical analysis and optimization of NDA's design and performance under exposure to solar radiation is presented and ultimately has shown that NDA can make the required measurements while pointed at 25° from the solar radial direction with some small compromises to the FOV and sensitive target area. A laboratory prototype of the instrument was built and tested using the dust accelerator at the University of Colorado, verifying that NDA can make sensitive dust measurements and achieves the required mass resolution. NDA's sufficient rejection of solar wind particles incident to the instrument was also experimentally verified with the prototype.

The overall conclusion is that the NDA design achieves the sensitivity, dynamic range, and capability of detecting the full expected range of nano-dust and β-meteoroids and measuring their composition based on the expected elemental constituents of IDPs. With these capabilities, NDA can confirm the existence of nano-dust, potentially determine their sources, origin, and size distribution, and investigate their interaction with the solar wind.

This thesis concludes with a short discussion on the exciting possibilities for NDA. The NDA instrument is ideally suited for a mission that combines studies of the inner Solar System dust complex with the exploration of dust-solar wind interactions. Nano-dust contributes to the mass, momentum and energy balance of the solar wind. The nature of nano-dust–solar wind interaction is an open question that motivates the simultaneous measurements of nano-dust, the

interplanetary magnetic field, as well as solar wind particle and pickup ion measurements to identify the role of nano-dust in the solar wind dynamics and structure through mass loading and inner source pickup ion generation. Thus, a near-Earth orbit mission with a suite of instruments, including NDA, presents an exciting opportunity to explore the dust complex in the inner Solar System and discover the significance of dust-solar wind interaction.

Bibliography

Auer, S. (2001). Instrumentation Interplanetary Dust ed. E. Grün, BAS Gustafson, S.F. Dermott and H. Fechtig.

Austin, D. E., Ahrens, T. J., & Beauchamp, J. L. (2002). Dustbuster: a compact impact ionization time-of-flight mass spectrometer for in situ analysis of cosmic dust. *Review of Scientific Instruments*, *73*(1), 185-189.

Baguhl, M., Grün, E., Linkert, G., Linkert, D., & Siddique, N. (1993). Identification of "small" dust impacts in the Ulysses dust detector data. *Planetary and Space Science*, *41*(11-12), 1085-1098.

Barge, P., Pellat, R., & Millet, J. (1982). Diffusion of Keplerian motions by a stochastic force. II-Lorentz scattering of interplanetary dusts. *Astronomy and Astrophysics*, *115*, 8-19.

Berg, O. E., & Grün, E. (1973). Evidence of hyperbolic cosmic dust particles.

Brownlee, D. E. (1996). The elemental composition of interplanetary dust. In *IAU Colloq. 150: Physics, Chemistry, and Dynamics of Interplanetary Dust* (Vol. 104, p. 261).

Brownlee, D., Tsou, P., Aléon, J., Alexander, C. M. D., Araki, T., Bajt, S., ... & Borg, J. (2006). Comet 81P/Wild 2 under a microscope. *science*, *314*(5806), 1711-1716.

Burlaga, L. F. (1988). Magnetic clouds and force-free fields with constant alpha. *Journal of Geophysical Research: Space Physics*, *93*(A7), 7217-7224.

Burlaga, L. F. (1991). Magnetic clouds. In *Physics of the Inner Heliosphere II* (pp. 1-22). Springer Berlin Heidelberg.

Ceplecha, Z., Borovička, J., Elford, W. G., ReVelle, D. O., Hawkes, R. L., Porubčan, V., & Šimek, M. (1998). Meteor phenomena and bodies. *Space Science Reviews*, *84*(34), 327-471.

Collette, A., Grün, E., Malaspina, D., & Sternovsky, Z. (2014). Micrometeoroid impact charge yield for common spacecraft materials. *Journal of Geophysical Research: Space Physics*, *119*(8), 6019-6026.

Czechowski, A., & Mann, I. (2010). Formation and acceleration of nano dust in the inner heliosphere. *The Astrophysical Journal*, *714*(1), 89.

Dahl, D. A. (2000). SIMION for the personal computer in reflection. *International Journal of Mass Spectrometry*, *200*(1), 3-25.

Dietzel, H., Neukum, G., & Rauser, P. (1972). Micrometeoroid simulation studies on metal targets. *Journal of Geophysical Research*, *77*(8), 1375-1395.

Dohnanyi, J.S. (1969). Collisional model of asteroids and their debris. *J. Geophys. Res.* 74, 2531-2554

Drapatz, S., & Michel, K. W. (1974). Theory of shock-wave ionization upon high-velocity impact of micrometeorites. *Zeitschrift für Naturforschung A*, *29*(6), 870- 879.

Fujiwara, A., Kamimoto, G., & Tsukamoto, A. (1977). Destruction of basaltic bodies by high-velocity impact. *Icarus*, *31*(2), 277-288.

Fuselier, S. A., Bochsler, P., Chornay, D., Clark, G., Crew, G. B., Dunn, G., ... & Googins, J. (2009). The IBEX-Lo Sensor. *Space science reviews*, *146*(1-4), 117-147.

Geiss, J., Gloeckler, G., Fisk, L. A., & Steiger, R. V. (1995). C+ pickup ions in the heliosphere and their origin. *Journal of Geophysical Research: Space Physics*, *100*(A12), 23373-23377.

Gloeckler, G., Fisk, L. A., Geiss, J., Schwadron, N. A., & Zurbuchen, T. H. (2000). Elemental composition of the inner source pickup ions. *Journal of Geophysical Research: Space Physics*, *105*(A4), 7459-7463.

Graps, A. L., Grün, E., Svedhem, H., Krüger, H., Horányi, M., Heck, A., & Lammers, S. (2000). Io as a source of the Jovian dust streams. *Nature*, *405*(6782), 48-50.

Grün, E., Pailer, N., Fechtig, H., & Kissel, J. (1980). Orbital and physical characteristics of micrometeoroids in the inner solar system as observed by Helios 1. *Planetary and Space Science*, *28*(3), 333-349.

Grün, E., Zook, H. A., Fechtig, H., & Giese, R. H. (1985). Collisional balance of the meteoritic complex. *Icarus*, *62*(2), 244-272.

Grün, E., Zook, H. A., Baguhl, M., Balogh, A., Bame, S. J., Fechtig, H., ... & Lindblad, B. A. (1993). Discovery of Jovian dust streams and interstellar grains by the Ulysses spacecraft.

Grün, E., Gustafson, B., Mann, I., Baguhl, M., Morfill, G. E., Staubach, P., & Zook, H.A. (1994). Interstellar dust in the heliosphere. *Astronomy and Astrophysics*, *286*.

Gruntman, M. (1997). Energetic neutral atom imaging of space plasmas. *Review of Scientific Instruments*, *68*(10), 3617-3656.

Gustafson, B. A. (1994). Physics of zodiacal dust. *Annual Review of Earth and Planetary Sciences*, *22*(1), 553-595.

Hamamatsu Photonics K.K., Electron Tube Division (2006). Electron multipliers.

Hamamatsu Photonics K.K., Electron Tube Division (2015). Electron multipliers.

Hamilton, D. P., Grun, E., & Baguhl, M. (1996). Electromagnetic escape of dust from the Solar System. In *IAU Colloq. 150: Physics, Chemistry, and Dynamics of Interplanetary Dust* (Vol. 104, p. 31).

Hilchenbach, M., Kissel, J., Langevin, Y., Briois, C., Von Hoerner, H., Koch, A., ... & Cottin, H. (2016). Comet 67P/Churyumov–Gerasimenko: close-up on dust particle fragments. *The Astrophysical Journal Letters*, *816*(2), L32.

Hillier, J. K., Sestak, S., Green, S. F., Postberg, F., Srama, R., & Trieloff, M. (2009). The production of platinum-coated silicate nanoparticle aggregates for use in hypervelocity impact experiments. *Planetary and Space Science*, *57*(14), 2081-2086.

Hoeksema, J. T. (1995). The large-scale structure of the heliospheric current sheet during the Ulysses epoch. *Space Science Reviews*, *72*(1), 137-148.

Horányi, M. (2000). Dust streams from Jupiter and Saturn. *Physics of Plasmas*, *7*(10), 3847-3850.

Horányi, M., Sternovsky, Z., Lankton, M., Dumont, C., Gagnard, S., Gathright, D., ... & Lamprecht, B. (2015). The lunar dust experiment (ldex) onboard the lunar atmosphere and dust environment explorer (ladee) mission. In *The Lunar Atmosphere and Dust Environment Explorer Mission (LADEE)* (pp. 93-113). Springer International Publishing.

Hornung, K., Drapatz, S. (1979). Residual ionization after impact of large dust particles. In: European Space Agency Special Publication ESA SP-155, 23-37.

Hsu, H. W., Postberg, F., Kempf, S., Trieloff, M., Burton, M., Roy, M., ... & Srama, R. (2011). Stream particles as the probe of the dust-plasma-magnetosphere interaction at Saturn. *Journal of Geophysical Research: Space Physics*, *116*(A9).

Jessberger, E. K., Stephan, T., Rost, D., Arndt, P., Maetz, M., Stadermann, F. J., ... & Kurat, G. (2001). Properties of interplanetary dust: Information from collected samples. In *Interplanetary Dust* (pp. 253-294). Springer Berlin Heidelberg.

Jia, Y. D., Ma, Y. J., Russell, C. T., Lai, H. R., Toth, G., & Gombosi, T. I. (2012). Perpendicular flow deviation in a magnetized counter-streaming plasma. *Icarus*, *218*(2), 895-905.

Jones, A. P., Tielens, A. G. G. M., & Hollenbach, D. J. (1996). Grain shattering in shocks: The interstellar grain size distribution. *The Astrophysical Journal*, *469*, 740.

Juhász, A., & Horányi, M. (2013). Dynamics and distribution of nano-dust particles in the inner solar system. *Geophysical Research Letters*, *40*(11), 2500-2504.

Kempf, S., Srama, R., Postberg, F., Burton, M., Green, S. F., Helfert, S., ... & Roy, M. (2005b). Composition of saturnian stream particles. *Science*, *307*(5713), 1274-1276.

Kempf, S., Srama, R., Horányi, M., Burton, M., Helfert, S., Moragas-Klostermeyer, G., ... & Grün, E. (2005a). High-velocity streams of dust originating from Saturn. *Nature*, *433*(7023), 289-291.

Kempf, S., Srama, R., Grün, E., Mocker, A., Postberg, F., Hillier, J. K., ... & Thissen, R. (2012). Linear high resolution dust mass spectrometer for a mission to the Galilean satellites. *Planetary and Space Science*, *65*(1), 10-20.

Kimura, H., Okamoto, H., & Mukai, T. (2002). Radiation pressure and the Poynting–Robertson effect for fluffy dust particles. *Icarus*, *157*(2), 349-361.

Kissel, J., Glasmachers, A., Grün, E., Henkel, H., Höfner, H., Haerendel, G., ... & Möhlmann, D. (2003). Cometary and interstellar dust analyzer for comet Wild 2. *Journal of Geophysical Research: Planets*, *108*(E10).

Knabe, W., & Krueger, F. R. (1982). Ion formation from alkali iodide solids by swift dust particle impact. *Zeitschrift für Naturforschung A*, *37*(12), 1335-1340.

Krittinatham, W., & Ruffolo, D. (2009). Drift orbits of energetic particles in an interplanetary magnetic flux rope. *The Astrophysical Journal*, *704*(1), 831.

Kurat, G., Koeberl, C., Presper, T., Brandstätter, F., & Maurette, M. (1994). Petrology and geochemistry of Antarctic micrometeorites. *Geochimica et Cosmochimica Acta*, *58*(18), 3879-3904.

Lamy, P. L. (1974). Interaction of interplanetary dust grains with the solar radiation field. *Astronomy and Astrophysics*, *35*, 197-207.

Landgraf, M., Augustsson, K., Grün, E., & Gustafson, B. Å. S. (1999). Deflection of the local interstellar dust flow by solar radiation pressure. *Science*, *286*(5448), 2319-2322.

Lazar, M., Schlickeiser, R., & Poedts, S. (2012). *Suprathermal particle populations in the solar wind and corona*. INTECH Open Access Publisher.

Le Chat, G., Issautier, K., Zaslavsky, A., Pantellini, F., Meyer-Vernet, N., Belheouane, S., & Maksimovic, M. (2015). Effect of the interplanetary medium on nanodust observations by the Solar Terrestrial Relations Observatory. *Solar Physics*, *290*(3), 933-942.

Lee, S. K., Hsu, H. C., & Tuan, W. H. (2016). Oxidation Behavior of Copper at a Temperature below 300° C and the Methodology for Passivation. *Materials Research*, (AHEAD), 0-0.

Leinert, C., Richter, I., Pitz, E., & Planck, B. (1981). The zodiacal light from 1.0 to 0.3 AU as observed by the Helios space probes. *Astronomy and Astrophysics*, *103*, 177-188.

Leinert, C., & Grün, E. (1990). Interplanetary dust. In *Physics of the Inner Heliosphere I* (pp. 207-275). Springer Berlin Heidelberg.

Leitner, M., Farrugia, C. J., Möstl, C., Ogilvie, K. W., Galvin, A. B., Schwenn, R., & Biernat, H. K. (2007). Consequences of the force-free model of magnetic clouds for their heliospheric evolution. *J. Geophys. Res.: Space Physics*, *112*(A6).

Lepping, R. P., J. A. Jones, and L. F. Burlaga (1990), Magnetic field structure of interplanetary magnetic clouds at 1 AU, J. *Geophys. Res*., 95(A8), 11957–11965.

Liou, J. C., Zook, H. A., & Dermott, S. F. (1996). The contribution of Kuiper belt dust grains to the inner solar system. In *IAU Colloq. 150: Physics, Chemistry, and Dynamics of Interplanetary Dust* (Vol. 104, p. 163).

Lundquist, S. (1950). Magneto-hydrostatic fields. *Arkiv for fysik*, *2*(4), 361-365.

Mann, I., Grün, E., & Wilck, M. (1996). The contribution of asteroid dust to the interplanetary dust cloud: The impact of ULYSSES results on the understanding of dust production in the asteroid belt and of the formation of the IRAS dust bands. *Icarus*, *120*(2), 399-407.

Mann, I., Krivov, A., & Kimura, H. (2000). Dust cloud near the Sun. *Icarus*, *146*(2), 568-582.

Mann, I., & Murad, E. (2005). On the existence of silicon nanodust near the sun. *The Astrophysical Journal Letters*, *624*(2), L125.

Mann, I., Köhler, M., Kimura, H., Cechowski, A., & Minato, T. (2006). Dust in the solar system and in extra-solar planetary systems. *The Astronomy and Astrophysics Review*, *13*(3), 159-228.

Mann, I., Meyer-Vernet, N., & Czechowski, A. (Eds.). (2012). Nanodust in the Solar System: Discoveries and Interpretations (Vol. 385). Springer Science & Business Media.

Martin, C., & Bowyer, S. (1982). Quantum efficiency of opaque CsI photocathodes with channel electron multiplier arrays in the extreme and far ultraviolet. *Applied optics*, *21*(23), 4206.

Maurette, M., Olinger, C., Michel-Levy, M. C., Kurat, G., Pourchet, M., Brandstätter, F., & Bourot-Denise, M. (1991). A collection of diverse micrometeorites recovered from 100 tonnes of Antarctic blue ice. *Nature*, *351*(6321), 44-47.

Meyer-Vernet, N., Maksimovic, M., Czechowski, A., Mann, I., Zouganelis, I., Goetz, K., ... & Bale, S. D. (2009). Dust detection by the wave instrument on STEREO: nanoparticles picked up by the solar wind?. *Solar Physics*, *256*(1), 463-474.

Miller, G., & Turner, L. (1981). Force free equilibria in toroidal geometry. *The Physics of Fluids*, *24*(2), 363-365.

Misconi, N. Y. (1993). The spin of cosmic dust: Rotational bursting of circumsolar dust in the F corona. *Journal of Geophysical Research: Space Physics*, *98*(A11), 18951-18961.

Mocker, A., Bugiel, S., Auer, S., Baust, G., Colette, A., Drake, K., ... & Hillier, J. (2011). A 2 MV Van de Graaff accelerator as a tool for planetary and impact physics research. *Review of Scientific Instruments*, *82*(9), 095111.

Mocker, A., Hornung, K., Grün, E., Kempf, S., Collette, A., Drake, K., ... & Srama, R. (2013). On the application of a linear time-of-flight mass spectrometer for the investigation of hypervelocity impacts of micron and sub-micron sized dust particles. *Planetary and Space Science*, *89*, 47-57.

Morfill, G. E., & Grün, E. (1979). The motion of charged dust particles in interplanetary space—I. The zodiacal dust cloud. *Planetary and Space Science*, *27*(10), 1269-1282.

Mukai, T., & Mukai, S. (1973). Temperature and motion of the grains in interplanetary space. *Publications of the Astronomical Society of Japan*, *25*, 481.

Mukai, T., Yamamoto, T., Hasegawa, H., Fujiwara, A., & Koike, C. (1974). On the circumsolar grain materials. *Publications of the Astronomical Society of Japan*, *26*, 445-458.

Mukai, T. (1981). On the charge distribution of interplanetary grains. *Astronomy and Astrophysics*, *99*, 1-6.

Mukai, T., & Schwehm, G. (1981). Interaction of grains with the solar energetic particles. *Astronomy and Astrophysics*, *95*, 373-382.

Nakamura, T., Noguchi, T., Tanaka, M., Zolensky, M. E., Kimura, M., Tsuchiyama, A., ... & Yada, T. (2011). Itokawa dust particles: a direct link between S-type asteroids and ordinary chondrites. *Science*, *333*(6046), 1113-1116.

Naumann, R. J., Jex, D. W., & Johnson, C. L. (1969). *Calibration of Pegasus and Explorer 23 detector panels NASA Rep*. TR R-321.

Nesvorný, D., Jenniskens, P., Levison, H. F., Bottke, W. F., Vokrouhlický, D., & Gounelle, M. (2010). Cometary origin of the zodiacal cloud and carbonaceous micrometeorites. Implications for hot debris disks. *The Astrophysical Journal*, *713*(2), 816.

Northrop, T. G. (1961). The guiding center approximation to charged particle motion. *Annals of Physics*, *15*(1), 79-101.

Northrop, T. G. (1963). Adiabatic charged-particle motion. *Reviews of Geophysics*, *1*(3), 283-304.

O'Brien, L., Auer, S., Gemer, A., Grün, E., Horanyi, M., Juhasz, A., ... & Srama, R. (2014). Development of the nano-dust analyzer (NDA) for detection and compositional analysis of nanometer-size dust particles originating in the inner heliosphere. *Review of Scientific Instruments*, *85*(3), 035113.

O'Brien, L., Grün, E., Sternovsky, Z. (2015). Optimization of the Nano-Dust Analyzer (NDA) for operation under solar UV illumination. *Planetary and Space Science*, *119*, 173-180.

O'Brien, L., Juhasz, A., Sternovsky, Z., Knipp, D. (2017). Effect of interplanetary coronal mass ejections on the dynamics of nano-dust born in the inner heliosphere (manuscript in preparation).

Owens, M. J., Merkin, V. G., & Riley, P. (2006). A kinematically distorted flux rope model for magnetic clouds. *Journal of Geophysical Research: Space Physics*, *111*(A3).

Pei, C., Bieber, J. W., Burger, R. A., & Clem, J. (2011). Three-dimensional wavy heliospheric current sheet drifts. *The Astrophysical Journal*, *744*(2), 170.

Poppe, A. R. (2016). An improved model for interplanetary dust fluxes in the outer Solar System. *Icarus*, *264*, 369-386.

Postberg, F., Kempf, S., Srama, R., Green, S. F., Hillier, J. K., McBride, N., & Grün, E. (2006). Composition of jovian dust stream particles. *Icarus*, *183*(1), 122-134.

Rachev, M., Srama, R., Srowig, A., & Grün, E. (2004). Large area mass analyzer. *Nuclear Instruments and Methods in Physics Research Section A: Accelerators, Spectrometers, Detectors and Associated Equipment*, *535*(1), 162-164.

Ragot, B. R., & Kahler, S. W. (2003). Interactions of dust grains with coronal mass ejections and solar cycle variations of the F-coronal brightness. *The Astrophysical Journal*, *594*(2), 1049.

Ratcliff, P. R., Burchell, M. J., Cole, M. J., Murphy, T. W., & Alladfadi, F. (1997). Experimental measurements of hypervelocity impact plasma yield and energetics. *International journal of impact engineering*, *20*(6-10), 663-674.

Rietmeijer, F. J. (2000). Interrelationships among meteoric metals, meteors, interplanetary dust, micrometeorites, and meteorites. *Meteoritics & Planetary Science*, *35*(5), 1025-1041.

Riley, P., & Crooker, N. U. (2004). Kinematic treatment of coronal mass ejection evolution in the solar wind. *The Astrophysical Journal*, *600*(2), 1035.

Romashets, E. P., & Vandas, M. (2003). Force-free field inside a toroidal magnetic cloud. *Geophysical research letters*, *30*(20).

Russell, H. N. (1929). On meteoric matter near the stars. *The Astrophysical Journal*, *69*, 49.

Russell, C. T., Jian, L. K., & Luhmann, J. G. (2009). An unusual current sheet in an ICME: Possible association with C/2006 P1 (McNaught). *Geophysical Research Letters*, *36*(7).

Russell, C. T., Weimer, D. R., Omidi, N., Jian, L. K., Luhmann, J. G., & Strangeway, R.J. (2010). Interplanetary field enhancements travel at the solar wind speed. *Geophysical Research Letters*, *37*(7).

Schatten, K. H., Wilcox, J. M., & Ness, N. F. (1969). A model of interplanetary and coronal magnetic fields. *Solar Physics*, *6*(3), 442-455.

Sekanina, Z., Hanner, M. S., Jessberger, E. K., & Fomenkova, M. N. (2001). Cometary dust. In *Interplanetary Dust* (pp. 95-161). Springer Berlin Heidelberg.

Shu, A., Collette, A., Drake, K., Grün, E., Horányi, M., Kempf, S., ... & Sternovsky, Z. (2012). 3 MV hypervelocity dust accelerator at the Colorado Center for Lunar Dust and Atmospheric Studies. *Review of Scientific Instruments*, *83*(7), 075108.

Srama, R., Ahrens, T. J., Altobelli, N., Auer, S., Bradley, J. G., Burton, M., ... & Grande, M. (2004). The Cassini cosmic dust analyzer. In *The Cassini-Huygens Mission* (pp. 465-518). Springer Netherlands.

Sterken, V. J., Altobelli, N., Kempf, S., Schwehm, G., Srama, R., & Grün, E. (2012). The flow of interstellar dust into the solar system. *Astronomy & Astrophysics*, *538*, A102.

Sternovsky, Z., Amyx, K., Bano, G., Landgraf, M., Horanyi, M., Knappmiller, S., ... & Auer, S. (2007). Large area mass analyzer instrument for the chemical analysis of interstellar dust particles. *Review of scientific instruments*, *78*(1), 014501.

Tielens, A. G. G. M., Seab, C. G., Hollenbach, D. J., & McKee, C. F. (1987). Shock processing of interstellar dust-Diamonds in the sky. *The Astrophysical Journal*, *319*, L109-L113.

Tielens, A. G. G. M., McKee, C. F., Seab, C. G., & Hollenbach, D. J. (1994). The physics of grain-grain collisions and gas-grain sputtering in interstellar shocks. *The Astrophysical Journal*, *431*, 321-340.

Vandas, M., Romashets, E., & Geranios, A. (2015). Modeling of magnetic cloud expansion. *Astronomy & Astrophysics*, *583*, A78.

Wagner, M., & Wimmer-Schweingruber, R. F. (2009). Interaction of interplanetary dust particles with magnetic clouds-Effects on the orbital evolution. *Astronomy & Astrophysics*, *507*(3), L41-L43.

Wang, C., Du, D., & Richardson, J. (2005). Characteristics of the interplanetary coronal mass ejections in the heliosphere between 0.3 and 5.4 AU. *Journal of Geophysical Research: Space Physics*, *110*(A10).

Wang, Y., Zhou, Z., Shen, C., Liu, R., & Wang, S. (2015). Investigating plasma motion of magnetic clouds at 1 AU through a velocity-modified cylindrical force-free flux rope model. *Journal of Geophysical Research: Space Physics*, *120*(3), 1543-1565.

Zook, H. A. (1975). Hyperbolic cosmic dust: its origin and its astrophysical significance. *Planetary and Space Science*, *23*(10), 1391-1397.

Zook, H. A., & Berg, O. E. (1975). A source for hyperbolic cosmic dust particles. *Planetary and Space Science*, *23*(1), 183-203.

Zurbuchen, T. H., Bochsler, P. A., & Scholze, F. (1995). Reflection of ultraviolet light at 121.6 nm from rough surfaces. *Optical Engineering*, *34*(5), 1303-1315.